Multi-Parametric Photoacoustic Microscopy of Cerebral Hemodynamics and Metabolism

---

A Dissertation

Presented to

the faculty of the School of Engineering and Applied Science

University of Virginia

---

in partial fulfillment
of the requirements for the degree

Doctor of Philosophy

by

Rui Cao

August 2018

APPROVAL SHEET

This Dissertation
is submitted in partial fulfillment of the requirements
for the degree of
Doctor of Philosophy

Author Signature: Rui Cao

This Dissertation has been read and approved by the examining committee:

Advisor: Song Hu

Committee Member: John Hossack

Committee Member: Craig Meyer

Committee Member: Zhiyi Zuo

Committee Member: Shayn Peirce-Cottler

Committee Member:

Accepted for the School of Engineering and Applied Science:

Craig H. Benson, School of Engineering and Applied Science

August 2018

ABSTRACT

There is no organ in the body as dependent as the brain on a continuous blood supply. Unsurprisingly, disruptions in cerebral hemodynamics and oxygen metabolism underlie a wide spectrum of brain disorders, including ischemic stroke, traumatic brain injury, epilepsy and Alzheimer's disease. Capitalizing on the optical absorption of hemoglobin, the primary oxygen carrier in the circulation, photoacoustic microscopy (PAM) is uniquely capable of imaging all hemodynamic and oxygen-metabolic parameters with high spatiotemporal resolution in vivo in a label-free manner.

The first part of my dissertation, Chapter II, Chapter III, and Chapter IV, focuses on the design, instrumentation, and validation of the multi-parametric PAM, which are capable of simultaneously *in vivo* imaging the total concentration of hemoglobin, oxygen saturation, and blood flow speed in the mouse brain. Combining these parameters, two key oxygen metabolism parameters, oxygen extraction fraction and metabolic rate of oxygen, can be quantified. After the validation of the multi-parametric PAM, the head-restraint apparatus has been designed to extend the capability of our system to image the awake mouse brain, avoiding the bias introduced by the anesthesia. Furthermore, complicated algorithms have been designed for data analysis, image processing and vessel segmentation, allowing the comprehensive characterization of the cerebral vasculature in the awake mouse brain. Beyond the parameters mentioned above, comprehensive cerebrovascular characterization also includes vessel density, tortuosity, shear stress, resistance, blood brain barrier permeability, and cerebrovascular reactivity. This PAM-based imaging and analysis platform enables comprehensive and quantitative characterization of obesity-induced structural, functional and oxygen-metabolic

changes in the cerebral microvasculature, in particular the increased response to vasodilatory stimulation.

The second part of my dissertation, Chapter V, and Chapter VI, demonstrated the feasibility of using our multi-parametric PAM for the studies of brain diseases in both mice and rats. The influence of blast traumatic brain injury (TBI) on cerebrovascular reactivity was investigated using PAM. The results showed the impaired cerebrovascular reactivity due to the blast TBI, although there was no observable vasculature damage. This study is the first to comprehensively characterize the cerebrovascular responses to bTBI. The striking impairment of the cerebrovascular reactivity by moderate bTBI, as revealed by our study, may lead to increased vulnerability of the brain to metabolic insults such as hypoxia/ischemia and secondary injuries. Furthermore, the feasibility of using PAM to image the cerebral hemodynamics in acute ischemic stroke has also been demonstrated in awake mouse brain, which showed clear changes in response to the ischemia. This provides the opportunity for further ischemic stroke studies without the interruption of the neuroprotective anesthetic. In the end, the neuroprotective effect of Sphingosine-1-phosphate was investigated, which showed altered cerebral oxygenation under hypoxia. The decreased cerebral metabolic rate of oxygen under hypoxia was found in the animal with elevated S1P, which may explain the reduced infarct volume in the pre-treatment animals.

ACKNOWLEDGEMENTS

First of all, I would like to acknowledge particularly acknowledge Dr. Song Hu for providing valuable opportunities, guidance, and assistance in both my research and career. Without his constructive advice and discussion, I would not have accomplished this work.

I would also like to thank Dr. Zhiyi Zuo for the general help, great insight, and critical advices for the animal experiment design. Additionally, Dr. John Hossack, Dr. Craig H. Meyer, and Dr. Shayn Peirce-Cottler, who served on my dissertation committee, are acknowledged for their time and suggestions in shaping my dissertation.

Next, I would like to acknowledge Dr. Bo Ning, Dr. Matthew Kennedy, Mr. Dr. Chenchu Zhang, Mr. Naidi Sun, and Dr. Adam Dixon for their great contributions to this dissertation in system design and development, animal preparation, and valuable discussion. I would particularly acknowledge Dr. Jun Li for his sustained support, especially for the animal surgery and procedures. In addition, I would like to thank all the lab members, past and present.

Last, but not least, I thank my family for their endless support; especially my wife, Xi Lei. This dissertation will not be possible without her support and love.

Table of Contents

Acronyms

ACZ: acetazolamide

BBB: Blood-brain barrier

bTBI: Blast traumatic brain injury

CBF: Cerebral blood flow

C_{Hb}: Hemoglobin concentration

$CMRO_2$: Cerebral metabolic rate of oxygen

CSVD: Cerebral small vessel disease

CT: Computed tomography

CVR: Cerebrovascular reactivity

DOT: diffuse optical tomography

fMRI: Functional magnetic resonance imaging

fPAM: Functional photoacoustic microscopy

MCA: Middle cerebral artery

MCAO: Middle cerebral artery occlusion

MPM: multiphoton microscopy

MRI: Magnetic resonance imaging

MRO_2: Metabolic rate of oxygen

LSI: laser speckle imaging

OCT: optical coherence tomography

OEF: Oxygen extraction fraction

OISI: optical intrinsic signal imaging

PAI: photoacoustic imaging

PAM: Photoacoustic microscopy

PET: Positron emission tomography

S1P: Sphingosine-1-phosphate

sO_2: Oxygen saturation

TBI: Traumatic brain injury

tMCAO: Transient middle cerebral artery occlusion

Chapter I: Introduction

1.1 Background and Motivation

Our understanding of the brain, one of the most complicated and least understood organs, has been revolutionized in the past decades with the help of rapid advances in neuroimaging[1]. The concept of neurovascular coupling and the use of cerebral hemodynamics as a surrogate of neural activity is drawing enormous attention, enabled by innovations in multiphoton microscopy (MPM)[2,3], optical coherence tomography (OCT)[4,5], laser speckle imaging (LSI)[6], optical intrinsic signal imaging (OISI)[7], diffuse optical tomography (DOT)[8,9], and functional magnetic resonance imaging (fMRI)[10,11]. Although fundamental improvements have been made, a major challenge is still unsolved, which is the gap between mechanistic studies in animals and clinical practice in humans. The applications of advanced functional and molecular neuroimaging techniques, such as fMRI and positron emission tomography (PET), provide excellent tissue penetration which is enough for the entire human brain imaging. However, due to limited spatial resolution, it is complicated to translate the clinical study from the human to the mouse, a species with abundant brain disease models and genetic manipulations available[12]. For instance, in the mouse model of focal brain ischemia which has important implications for microinfarction-induced human dementia, the infarct spans only about 500 μm[13]. Thus, studying these models usually requires much finer resolution than that of current PET and fMRI.

Providing high-resolution views of the brain at the cellular level, the optical microscopy techniques (such as OCT, MPM, OISI, and LSI) enables the study of various mouse models[14]. The superior resolution and rich endogenous and

fluorescence contrasts make these optical microscopy very popular in the biological society. However, the limited penetration depth (1-2 mm), caused by the strong scattering of biological tissues, prevents these optical microscopy techniques from whole brain studies. For instance, the invasive cranial window is usually required for MPM to image the underlying mouse cortex since light scattering in the skull is too strong which will affect the imaging quality[15]. However, it has been reported that the open-skull procedure can easily affect the brain environment and leads to readout bias[16].

Moreover, existing preclinical neuroimaging techniques lack the capability of quantifying cerebral oxygen metabolism at the microscopic level. Consuming about 20% of oxygen despite its relatively small size (~2% body weight), the brain is vulnerable to the disturbance of oxygen metabolism, which is relevant to a broad range of neurological disorders[17]. Thus, high-resolution imaging of the cerebral metabolic rate of oxygen ($CMRO_2$) in mice is in great need for various studies of the brain function and pathology. Capitalizing on the elegant integration of optics and ultrasound, photoacoustic imaging (PAI) provides a revolutionary solution[18]. Capable of extracting the blood oxygenation and flow encoded in the optical absorption spectrum and dynamics of red blood cells (RBCs), PAI provides the opportunity to the microscopy level $CMRO_2$ in mice.

1.2 PAM Principles and Advantages

Capable of directly probing biomolecules through their unique spectra, optical imaging plays an indispensable role in biomedicine. However, pure optical imaging technologies fall into two spatially distinct categories, high-resolution (down to tens of nanometers) optical microscopy at shallow depth (less than 1 millimeter) and deep-penetrating (up to 7 centimeters) optical tomography with macroscopic

resolution (~1/3 of the imaging depth), leaving a huge gap in between[18]. Ultrasound imaging, in contrast, provides seamless spatial scalability by varying the acoustic frequency, but it remains a challenge to directly detect chemical contrasts underlying the tissue function and metabolism[19].

Combining optical contrast and ultrasonic scalability, photoacoustic imaging (PAI) is among the most rapidly growing biomedical imaging modalities in recent years[18,20]. In PAI, short-pulsed or intensity-modulated laser light is absorbed by endogenous or exogenous chromophores in biological tissues, which induces transient heating. The subtle temperature rise (at the level of milliKelvin) leads to thermoelastic expansion of the tissue and subsequent emission of ultrasonic waves, which can be captured by an acoustic detector(s) to map the distribution of the optical absorber *in vivo* [Fig. 1]. The conversion of optical excitation to acoustic emission brings two unique advantages: specific imaging contrast of optical absorption and excellent depth-to-resolution ratio across the optical and acoustic dimensions. The absorption contrast complements that of fluorescence imaging, the most widely used optical modality for molecular imaging *in vivo*. It enables label-free PAI of multiple endogenous biomolecules, in particular hemoglobin and lipid, which are intrinsically weakly fluorescent and difficult to tag with exogenous contrast agents. Moreover, PAI detects emitted acoustic waves rather than fluorescent light. The much weaker scattering effect of the biological tissue on ultrasound than light allows effective acoustic focusing in the optical diffusive regime and leads to a depth-to-resolution ratio of ~200 in PAI, far exceeding that in diffuse optical tomography[18].

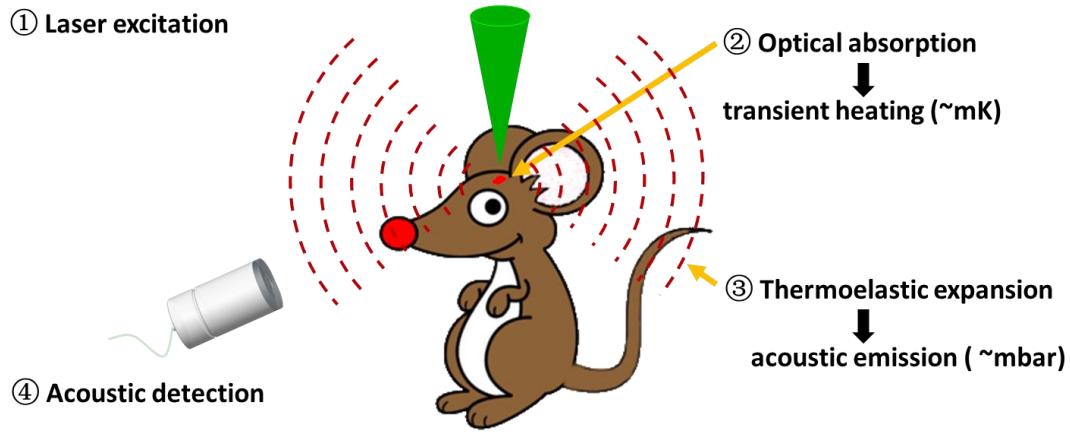

Fig. 1. Principle of photoacoustic imaging. mK: milliKelvin.

Providing the specific imaging contrast of optical absorption and excellent spatial scalability across the optical and ultrasonic dimensions, photoacoustic imaging has been rapidly emerging and expanding in the past two decades. This enabling technology that hold the potential to transform in vivo functional and molecular imaging at multiple length scales. Specifically, multi-parametric photoacoustic microscopy enables simultaneous high-resolution mapping of hemoglobin concentration, oxygen saturation and blood flow — opening up the possibility of quantifying the $CMRO_2$ at the microscopic level.

1.3 Functional Photoacoustic Imaging of the Brain Metabolism

Based on physiologically specific optical absorption contrasts, functional PAM (fPAM) enables imaging of functional parameters (i.e. oxygen saturation of hemoglobin and blood flow speed), in addition to the structure or the distribution of the contrast. In recent years, intensive research efforts have been made to unleash the full potential of fPAM[18,20]. Here, considering the scope of the dissertation, I will focus on the review of transformative advances in functional and molecular PAM of rodent brain.

As an important organ that performs many complicated tasks such as perception, motor control and learning, the mammal brain consumes a large portion of their energy intake considering its weight. For most mammals including human, the major energy source for the brain is the oxygen-dependent metabolism of glucose[21]. In major brain diseases, interrupted metabolic rate of glucose and/or oxygen is usually observed[22]. Thus, appropriate imaging tools for brain oxygen/glucose metabolism will not only improve understanding of the underlying brain dysfunction pathology but also enable the monitoring and design of targeted therapies.

Benefitting from the endogenous hemoglobin contrast, a key component for oxygen metabolism and transportation, PAM has been demonstrated for cerebral oxygen metabolism imaging[23]. Combining the measured brain arterial and venous sO_2 in individual vessels, the brain oxygen supply and local oxygen extraction can be directly calculated[24], which is key for understanding the progression and therapy of several severe brain dysfunctions such as brain hypoxia and ischemic stroke. Meanwhile, the normal cerebral blood flow (CBF) is also key for brain functions, which can also be measured through PAM using several different mechanisms such as the correlation analysis[25] or Doppler Effect[26]. Combining the arterial and venous sO_2 with CBF, the local $CMRO_2$ can be quantified, which can be used to evaluate the health state and activity level of the neurons[27].

Beyond the cerebral metabolism of oxygen, the measurement of blood glucose uptake is also indispensable for the understanding of brain metabolism. However, suffering from the strong background absorption of water in the near-infrared range and low photoacoustic signal from glucose, the blood glucose level is difficult to directly measure without exogenous contrast[28]. Luckily, the glucose uptake and local metabolism can be reflected via its analogs. Recently, the glucose update was imaged via photoacoustic imaging, with the help of one newly developed glucose

analog 2-deoxy-2-[N-(7-nitrobenz-2-oxa-1,3-diazol-4-yl)amino]-D-glucopyranose (2-NBDG)[29]. The 2-NBDG can be transported into cells and phosphatized but not further metabolized, which can be used to indicate the glucose uptake. With a peak absorption at 480 nm and strong photoacoustic signal, the photoacoustic imaging of 2-NBDG was demonstrated, which shows acute glucose uptake rate elevation in response to electrical stimulations to the mouse paw[30].

1.4 Dissertation Overview

In Chapter II, the development and principle of multi-parametric PAM was reviewed. Capitalizing on the optical absorption of hemoglobin, PAM is uniquely capable of anatomical and functional characterization of the intact microcirculation in vivo. However, PAM of the metabolic rate of oxygen (MRO_2) at the microscopic level remains an unmet challenge, mainly due to the inability to simultaneously quantify microvascular diameter, oxygen saturation (sO_2) of hemoglobin, and blood flow at the same spatial scale. To fill this technical gap, we have developed a multi-parametric PAM platform. By analyzing both the sO_2-encoded spectral dependence and the flow-induced temporal decorrelation of photoacoustic signals generated by the raster-scanned mouse ear vasculature, we demonstrated—for the first time—simultaneous wide-field PAM of all three parameters down to the capillary level in vivo. Furthermore, our newly developed multi-parametric PAM enables simultaneous quantification of the hemoglobin concentration (C_{Hb}), sO_2, and CBF at the microscopic level and through the intact mouse skull. Moreover, bi-directional raster scan allows determining the direction of blood flow in individual vessels. Capable of imaging all three hemodynamic parameters at the same spatiotemporal scale, our PAM fills a critical gap in preclinical neuroimaging and lays the foundation for high-resolution mapping of $CMRO_2$—a quantitative index of cerebral

oxygen metabolism. This technical innovation is expected to shed new light on the mechanism and treatment of a broad spectrum of neurological disorders, including Alzheimer's disease and ischemic stroke.

Chapter III focuses on the development of head-restraint multi-parametric PAM, which can be applied to image the awake mouse brain. A long-standing challenge in optical neuroimaging has been the assessment of hemodynamics and oxygen metabolism in the awake rodent brain at the microscopic level. Here, we demonstrated first-of-a-kind head-restrained PAM, which enables simultaneous imaging of the cerebrovascular anatomy, total concentration and oxygen saturation of hemoglobin, and blood flow in awake mice. Combining these hemodynamic measurements allows us to derive two key metabolic parameters—oxygen extraction fraction (OEF) and the $CMRO_2$. This enabling technology offers the first opportunity to comprehensively and quantitatively characterize the hemodynamic and oxygen-metabolic responses of the mouse brain to isoflurane, a general anesthetic widely used in preclinical research and clinical practice. Side-by-side comparison of the awake and anesthetized brains reveals that isoflurane induces diameter-dependent arterial dilation, elevated blood flow, and reduced OEF in a dose-dependent manner. As a result of the combined effects, $CMRO_2$ is significantly reduced in the anesthetized brain under both normoxia and hypoxia, which suggests a mechanism for anesthetic neuroprotection. The head-restrained functional and metabolic PAM opens a new avenue for basic and translational research on neurovascular coupling without the strong influence of anesthesia and on the neuroprotective effects of various interventions, including but not limited to volatile anesthetics, against cerebral hypoxia and ischemia.

Chapter IV focuses on the implementation of comprehensive characterization of cerebral vasculature using our head-restraint multi-parametric PAM. Metabolic

disorders-induced microvascular alternations have been linked to a variety of cerebrovascular and neurodegenerative diseases. However, the underlying mechanisms remain incompletely understood, partially due to the limited accessibility of these small vessels in the live brain. Currently, high-resolution intravital imaging of the cerebral microvasculature in the small-animal brain is predominantly carried out by two-photon microscopy. Even with the aid of angiographic agents, it remains an unmet challenge to comprehensively elucidate pathological changes in cerebral microvessels. CD-1 mice with obesity induced by high-fat diet and confirmed with blood examination were used to study the metabolic disorder-induced changes in the cerebral microvasculature. Multi-parametric PAM was used to image vascular anatomy, blood perfusion, oxygenation and flow in the awake brain. With the aid of vessel segmentation, these structural and functional parameters were extracted at the single-microvessel level, from which vascular density, tortuosity, shear stress, resistance and associated tissue oxygen extraction fraction and metabolism were also quantified. Moreover, relying on an in vivo Evans blue assay, permeability of the blood-brain barrier (BBB) was dynamically evaluated via time-lapse measurements of dye diffusion. Also, multifaceted cerebrovascular reactivity (CVR) to acetazolamide-based stimulation was assessed. Together, the comprehensive characterization revealed increased microvascular density, reduced arterial blood flow, impaired BBB integrity, and increased CVR in obese mice. Interestingly, the counterintuitive observation on the CVR echoed the elevated activation of the endothelial nitric oxide synthase. This PAM-based imaging and analysis platform enables comprehensive and quantitative characterization of obesity-induced structural, functional and oxygen-metabolic changes in the cerebral microvasculature, in particular the increased response to vasodilatory stimulation. This technology is widely applicable to the studies of small

vessel disease in the brain and holds the potential to be transformed for microvascular studies in other vital organs (e.g., the heart and kidney).

Chapter V shows the application of our multi-parametric PAM for the study of cerebrovascular dysfunctions after blast traumatic brain injury. Blast traumatic brain injury (bTBI) is a leading contributor to combat-related injuries and death. Although substantial attention has been drawn to bTBI-induced neuronal dysfunction, co-existing dysfunction in the cerebral vasculature, especially microvessels, remains under-studied and poorly understood. Here, we studied the bTBI-induced cerebrovascular dysfunction in a rat model of bTBI (blast pressure: 187.8±18.3 kPa). Using multi-parametric photoacoustic microscopy, we quantified the changes in cerebral hemodynamics and metabolism—including blood perfusion, oxygenation, flow, oxygen extraction fraction, and the metabolic rate of oxygen—in a label-free manner 4 hours post the injury. Moreover, we assessed the influence of bTBI on the cerebrovascular reactivity to vasodilatory stimulation. With vessel segmentation, we dissected the multifaceted responses at the single-vessel level, revealing the dependence of the responses on the vessel type (i.e., artery vs. vein) and diameter. We found that the moderate bTBI did not induce pronounced changes in the microvascular diameter, blood perfusion, oxygenation, flow, oxygen extraction and metabolism in the brain, except a slight yet statistically significant sO2 increase in small veins (<45 μm) and flow increase in big veins (⩾45 μm). By contrast, the moderate bTBI almost completely abolished the cerebrovascular reactivity, including arterial dilation, flow upregulation, and venous sO_2 increase. This study is the first to comprehensively characterize the cerebrovascular responses to bTBI. The striking impairment of the cerebrovascular reactivity by moderate bTBI, as revealed by our study, may lead to increased vulnerability of the brain to metabolic insults such as hypoxia/ischemia and secondary injuries.

Chapter VI demonstrated the capability of studying the ischemic stroke and the anesthetic neuroprotection using our multi-parametric PAM. Stroke affects 800,000 people in the United States every year, and ischemic stroke accounts for 87% of all stroke incidences[31]. The risk for ischemic stroke is even higher in obese people. As the one of the major cause of death in United States, in the past decades, it has been widely reported that anesthetics have effects on neuronal and vascular function, which raises the possibility that anesthesia could affect the outcome of a neuroprotection study. In order to address this problem, the potential therapies and neuroprotection mechanism need to be studied in a model of stroke that can be induced without anesthesia. We firstly demonstrated the feasibility of our head-restraint PAM to imaging the ischemic stroke induced cerebral hemodynamic and metabolic changes under awake condition using the widely accepted transient middle cerebral artery occlusion (tMCAO) model. To further avoid the use of anesthetic during the ischemic stroke procedure, the photothrombotic stroke model using Rose Bengal dye was also explored, which can induce the vascular occlusion through illuminating the green light without anesthesia. The widely used general anesthetic, isoflurane, was used as the neuroprotective agent to check the anesthetic-induced hemodynamic changes and corresponding neuroprotection. Furthermore, the neuroprotective sphingosine-1-phosphate (S1P) was observed to induce oxygen metabolism changes in awake mouse, which may help better understand its neuroprotection mechanism from the metabolism prospective.

Finally, in Chapter VII, the summary of my dissertation work and discussion of future improvement are presented.

Chapter II. Multi-parametric PAM

2.1 Principle of multi-parametric PAM

2.1.1 Oxygen Saturation (sO_2)

Due to the difference in absorption spectrum, the concentrations of oxy-hemoglobin [HbO_2] and de-oxy hemoglobin [HbR] can be distinguished by using two wavelengths and corresponding spectroscopic analysis[32]. Since the [HbO_2] and [HbR] are the dominant absorbing compounds in visible range, the blood absorption coefficients at wavelength λ_1 and wavelength λ_2 can be calculated as following:

$$\mu_a(\lambda_1) = \varepsilon_{HbR}(\lambda_1)[\mathrm{HbR}] + \varepsilon_{HbO_2}(\lambda_1)[\mathrm{HbO_2}] \quad \text{(eq. 2.1)}$$

$$\mu_a(\lambda_2) = \varepsilon_{HbR}(\lambda_2)[\mathrm{HbR}] + \varepsilon_{HbO_2}(\lambda_2)[\mathrm{HbO_2}] \quad \text{(eq. 2.2)}$$

where ε_{HbR} and ε_{HbO_2} are the wavelength-dependent molar extinction coefficients of HbR and HbO_2, which are known constants. Meanwhile, the blood absorption coefficients μ_a is proportional to the photoacoustic signal, which can be used to derive the relative concentration of [HbO_2] and [HbR]. Therefore, the absolute oxygen saturation (sO_2) can thus be deducted through the following equation:

$$sO_2 = \frac{[HbO_2]}{[HbR]+[HbO_2]}. \quad \text{(eq. 2.3)}$$

Because the laser availability and the strong absorption of hemoglobin, the lasers at the wavelengths of 532 nm and 558 nm are widely used in the PAM measurement of sO_2.

To validate PAM measurement of sO_2, the comparison of PAM measurement and established blood gas analyzer were done. To assess the accuracy of PAM across a wide variety of physiological and pathophysiological states, we introduced three different conditions by alternating the oxygen concentration in the inhalation gas. Normoxia was first attained with room air, followed by moderate hypoxia (14% O_2, 86% N_2), again normoxia, and finally severe hypoxia (7% O_2, 93% N_2). Measurements were taken 5 minutes after each change to allow for equilibration. As expected, our results (Fig. 2.1) showed a good agreement (R^2=0.97 and p=0.0001) between the in vivo PAM measurements and the readouts of blood-gas analyzer across a wide range of sO_2 values (40–100%).

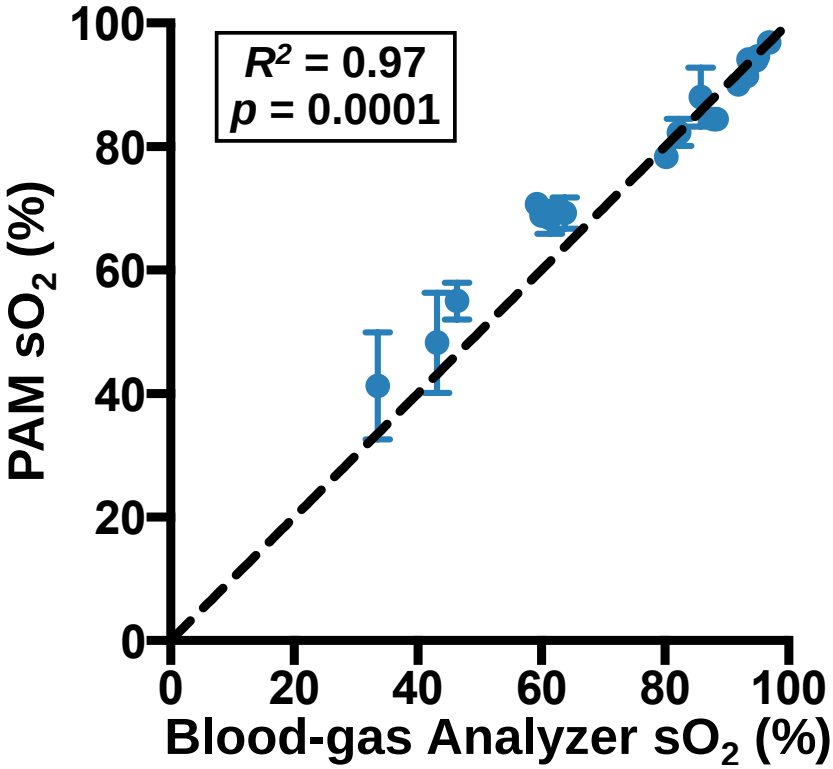

Fig. 2.1 Comparison of the arterial sO_2 measured by *in vivo* transcranial PAM and blood-gas analyzer in mice (N=4) under systemic normoxia (21% O_2), moderate hypoxia (14% O_2), and severe hypoxia (7% O_2). PAM measurements are presented in mean ± standard deviation.

2.1.2 Concentration of Total Hemoglobin (C_{Hb})

The absolute value of C_{Hb} can be quantified by statistical analysis of PAM signals [33]. At 532 nm, a near-isosbestic point of hemoglobin, PAM is insensitive to sO_2. Fluctuation in the amplitude of the PAM signal acquired at this wavelength encodes both the Brownian motion and the flow of red blood cells (RBCs). Since the Brownian motion of RBCs follows the Poisson distribution, the average RBC count within the detection volume (N_{RBC}) can be estimated as:

$$E(N_{RBC}) = \frac{E(Amp)}{Var(Amp) - Var(Noise)}, \quad (1)$$

where $E()$ and $Var()$ are the mean and variance operation, respectively. Amp and $Noise$ denote the amplitude of the photoacoustic signal and the noise of the PAM system, respectively. With this, the average RBC count can be quantified through the statistical analysis of 100 successive A-lines. Given that fact that each RBC contains ~15 pg of hemoglobin [34], C_{Hb} can thus be estimated as:

$$C_{Hb} = \frac{15 \times E(N_{RBC})}{Vol}, \quad (2)$$

where Vol represents the detection volume of the PAM system. If the lateral resolution is assumed at 2.7 μm, the detection volume should be 263 μm [33,34]. Before *in vivo* experiments, the accuracy of this method has been examined with samples of 10 different C_{Hb} values evenly distributed over the range of 15–150 g/L (fresh defibrinated bovine blood, Quad Five). The PAM-measured C_{Hb} values have shown good agreement with the preset concentrations (linearity: R^2=0.96) above 30 g/L. It becomes inaccurate when the blood is further diluted to below 30 g/L, which is likely due to the insufficient SNR of PAM under the severe and non-physiological hemodilution.

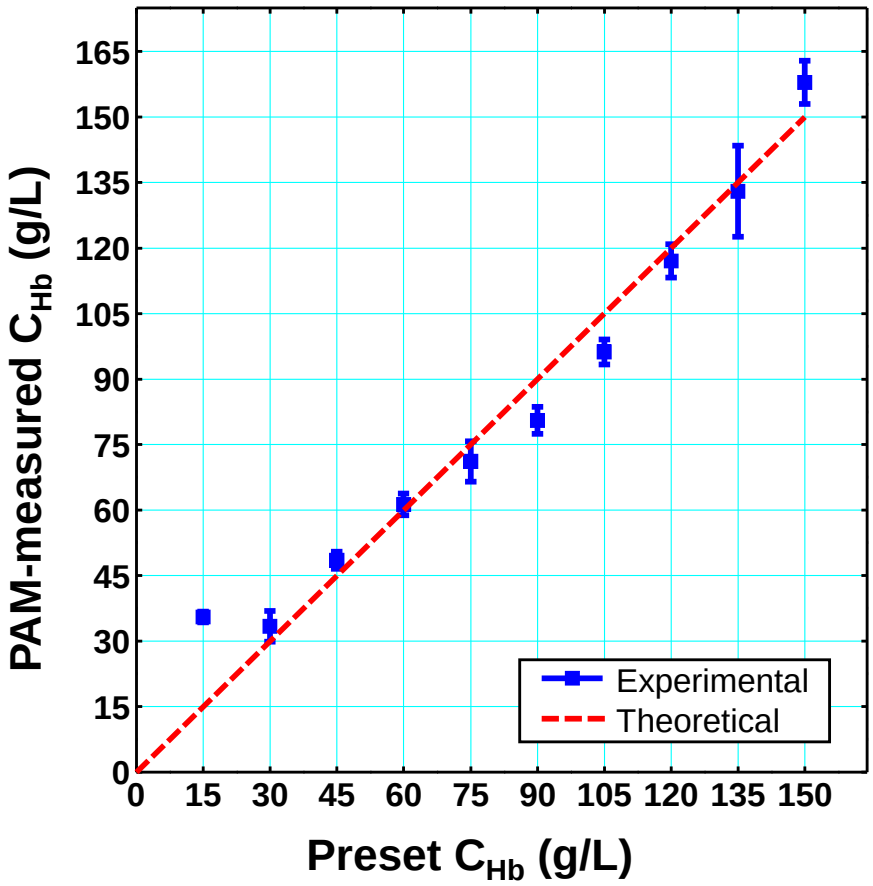

Fig. 2.2 Validation of PAM-based CHb measurements in vitro using diluted blood sample with preset CHb. PAM measurements are in mean ± SD.

2.1.3 Blood Flow

Correlation analysis of the same 100 A-lines used for the C_{Hb} measurement allows simultaneous quantification of the blood flow speed. The flow-induced A-line decorrelation follows a second-order exponential (i.e., Gaussian) decay, and the decay constant is linearly proportional to the flow speed [35,36]. Thus, the blood flow speed can be measured by fitting the experimental data to the decay model. Given the 100-μs interval between adjacent A-lines in our current PAM system, the correlation window is 10 ms. With a B-scan speed of 1 mm/s, the movement of the PAM scan head over this time window is only 10 μm, comparable to the average diameter of capillaries.

Furthermore, we validated our decorrelation-based wide-field flow measurement approach in a vessel-mimicking phantom (Fig. 2.3A). Specifically, a syringe pump (Pump System Inc., NE-300) was used to drive defibrinated bovine blood (Quad Five, 910) through a plastic tube (United States Plastic Corporation, 56514; inner diameter: ~250 μm). A randomly chosen cross section of the tube was imaged under three different preset flow rates, and the corresponding decay constants λ_f were extracted (Fig. 2.3B). The experimentally measured cross-sectional profile of λ_f agreed with the theoretical parabolic distribution of blood flow across the lumen, and the larger value of λ_f corresponded to the higher preset speed. We then calibrated the relationship between the decay constant λ_f and flow speed, which was set to 25 different values within the range of 0.03–40 mm/s (Fig. 2.3C). To evaluate the precision of our measurement, the flow speed across the tube was measured 40 times. As expected, the decay constant λ_f showed a good linear relationship (R^2=0.88) with the preset flow speed, which, however, did not hold beyond the range of 0.18–21 mm/s.

The lower detection limit is due to the 10-ms correlation window, which is not wide enough to record slow decays due to extremely low flow speeds. This limit could be extended by reducing the B-scan speed; however, this would increase the imaging time. The upper detection limit is due to the A-line rate (i.e., the laser repetition rate) being limited to 10 kHz, which is not adequate for accurate quantification of rapid decays due to high flow speeds. This limit could be extended by operating at a higher laser repetition rate and data acquisition speed; however, the bottleneck in our current data acquisition system does not allow that. Nevertheless, the current detection range provides good coverage of physiological flow rates in the rodent microcirculation[37].

Finally, we tested the feasibility of 2D flow mapping in a blood-perfused tube with a non-uniform diameter. According to the conservation of mass, the volumetric flow rate should remain constant throughout the tube, while the flow speed should vary with the cross-sectional diameter. The volumetric flow was set to 0.22 μL/s, and a segment of the tube was bi-directionally scanned (Fig. 2.3D). The scan parameters were the same as in the calibration experiment. As expected (Fig. 2.3E), the peak flow speed along the central axis of the tube (green curve) gradually increased with the decreasing tube diameter to maintain the volumetric flow at a near-constant value of 0.22±0.01 μL/s (blue curve). The perfect match between the preset and experimentally measured volumetric flow underscores the accuracy of our technique for quantitative flow mapping.

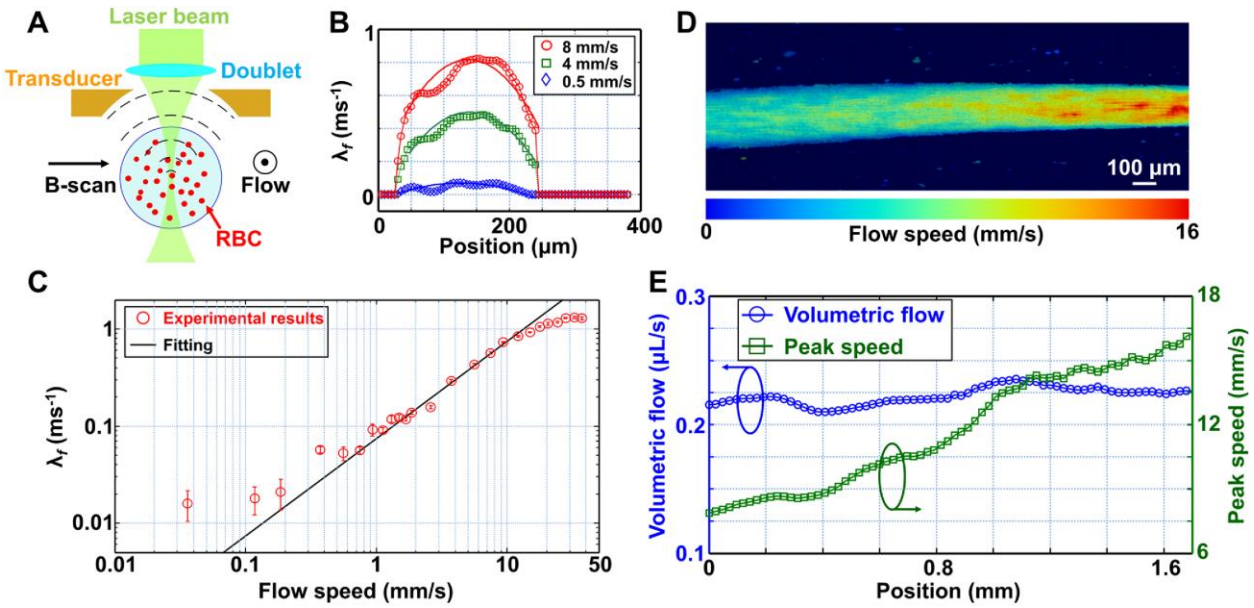

Fig. 2.3 Phantom validation of flow measurement. (a) Experimental configuration. (b) Parabolic profiles of the decay constant (λ_f) across the tube measured under different preset blood flow speeds. (c) Linear relationship between λ_f and the preset flow speed. The linear regression (dark line) is forced to go through the origin.

Circles and error bars are mean values and standard deviations, respectively. (d) Two-dimensional map of the blood flow in the tube. (e) Changes in the volumetric flow rate and peak cross-sectional flow speed along with the decreasing tube diameter. Reprinted from the reference (25).

2.1.4 Vessel Segmentation Analysis

To enable quantitative analysis of vessel diameters and extract the hemodynamics values within certain vessels, proper vessel segmentation algorithms are necessary [25]. The semi-automatic vessel segmentation algorithm and related data extraction are consisted of the following steps:

(1) Manually identify and select the boundary of all interested vessels in Matlab.

(2) Refine boundaries using the theory of Otsu threshold in the maximum amplitude projection (MAP) image.

(3) Remove over-lapping vessels and label the selected vessels with proper identification number.

(4) Obtain the skeletons (or "central line") of segmented vessels and calculate the length of the skeleton for each vessel.

(5) Calculate the total area for each individual segmented vessel and divided by the length of its skeleton, which gives us the vessel diameter.

(6) Extract the sO_2, blood flow speed, and C_{Hb} within vessels for further analysis using the segmentation information and classify the vessels with arteries and veins based on sO_2 value.

2.1.5 Oxygen Metabolism

With the aid of vessel segmentation, the blood flow in individual vessels can be extracted. Therefore, the vascular blood flow speed and diameter can be combined to derive CBF in the volumetric unit as:

$$CBF = \frac{\pi DV^2}{8}, \quad \text{(eq. 2.4)}$$

in which *D* is the vessel diameter and *V* is the blood flow speed along the central axis of the vessel. Thus, the volumetric blood flow in each individual vessel can be quantified. The total volumetric blood flow can thus be measured by adding up all the major feeding arteries or draining veins within the region of interest.

With the segmented vessels, the average sO_2 values of the feeding arteries (s_aO_2) and draining veins (s_vO_2) within the ROI can be extracted to quantify OEF within this region as:

$$OEF = \frac{s_aO_2 - s_vO_2}{s_aO_2}. \quad \text{(eq. 2.5)}$$

Now, all the necessary parameters for quantification of metabolic rate of oxygen (MRO_2) are obtained. Thus, MRO_2 can be derived as:

$$MRO_2 = \xi \times C_{Hb} \times s_aO_2 \times OEF \times \frac{BF_{total}}{W}, \quad \text{(eq. 2.6)}$$

where ξ is the oxygen binding capacity of hemoglobin (1.36 mL oxygen per gram hemoglobin), BF_{total} is the total volumetric blood flow through the region, and W is the tissue weight estimated by assuming an average cortical thickness of 1.2 mm and a tissue density of 1.05 g/ml [38,39]. One thing to be noticed is that the total volumetric flow rates in the feeding arteries and draining veins need to be approximately equal to validate the use of above $CMRO_2$ calculation. Meeting this

important condition in the cerebral cortex typically requires a relatively large field of view.

2.2 Multi-parametric PAM System

2.2.1 System Schematic

For the multi-parametric PAM (Fig. 2.4A), two nanosecond-pulsed lasers (Edgewave, BX40-2-G and BX40-2-GR; wavelengths: 532 and 559 nm; repetition rate: 30 kHz) are used for dual-wavelength photoacoustic excitation. The two laser outputs with orthogonal polarizations are combined using a broadband polarizing plate beam splitter (Edmund optics, 48–545), attenuated by a neutral-density filter (Thorlabs, NDC-50C-2M), and reduced to the same diameter by an iris (Thorlabs, SM1D12D) for fiber-optic coupling. To enhance the coupling efficiency, the combined laser beam is focused by a condenser lens (Thorlabs, LA1608) and reshaped again by a 50-μm-diameter pinhole (Thorlabs, P50C) positioned near the lens focus. The spatially filtered beam is then coupled into a single-mode optical fiber (Thorlabs, P1-460B-FC-2) through a microscope objective (Newport, M-10X). To compensate for the fluctuation in laser intensity, ~5% of the laser energy is tapped off by a beam sampler (Thorlabs, BSF10-A) before the objective and monitored by a high-speed photodiode (Thorlabs, FDS100).

As shown in the blow-up of the PAM scan head (Fig. 2.4B), the fiber output with a mode-field diameter of ~3 μm is mapped into the object to be imaged by two identical doublets (Thorlabs, AC127-025-A; one for collimation and the other for focusing). A 2D galvanometer scanner (Cambridge, 6215HSM40B) is inserted between the doublets for the automatic confocal alignment of the optical and acoustic foci prior to imaging experiments. To match the surface dimension of the

galvo mirrors, the diameter of the beam after the collimating doublet is reduced to 5 mm by an iris (Thorlabs, SM05D5). A ring-shaped LiNbO3 ultrasonic transducer (inner diameter: 2.2 mm; outer diameter: 4.0 mm; focal length: 6 mm; center frequency: 35 MHz; 6-dB bandwidth: 70%) was fabricated by the NIH Resource Center for Medical Ultrasonic Transducer Technology at the University of Southern California for convenient confocal alignment of the optical and acoustic foci in reflection mode. Directly passing the focused laser beam through the central hole of the transducer avoids the optical aberration and acoustic loss induced by otherwise needed optical-acoustic beam combiners in our first- and second-generation PAM systems [40,41]. For acoustic coupling, the transducer must be immersed in water. A correction lens (Thorlabs, LA1207-A) is inserted into the optical path to compensate for the optical aberration at the air-water interface.

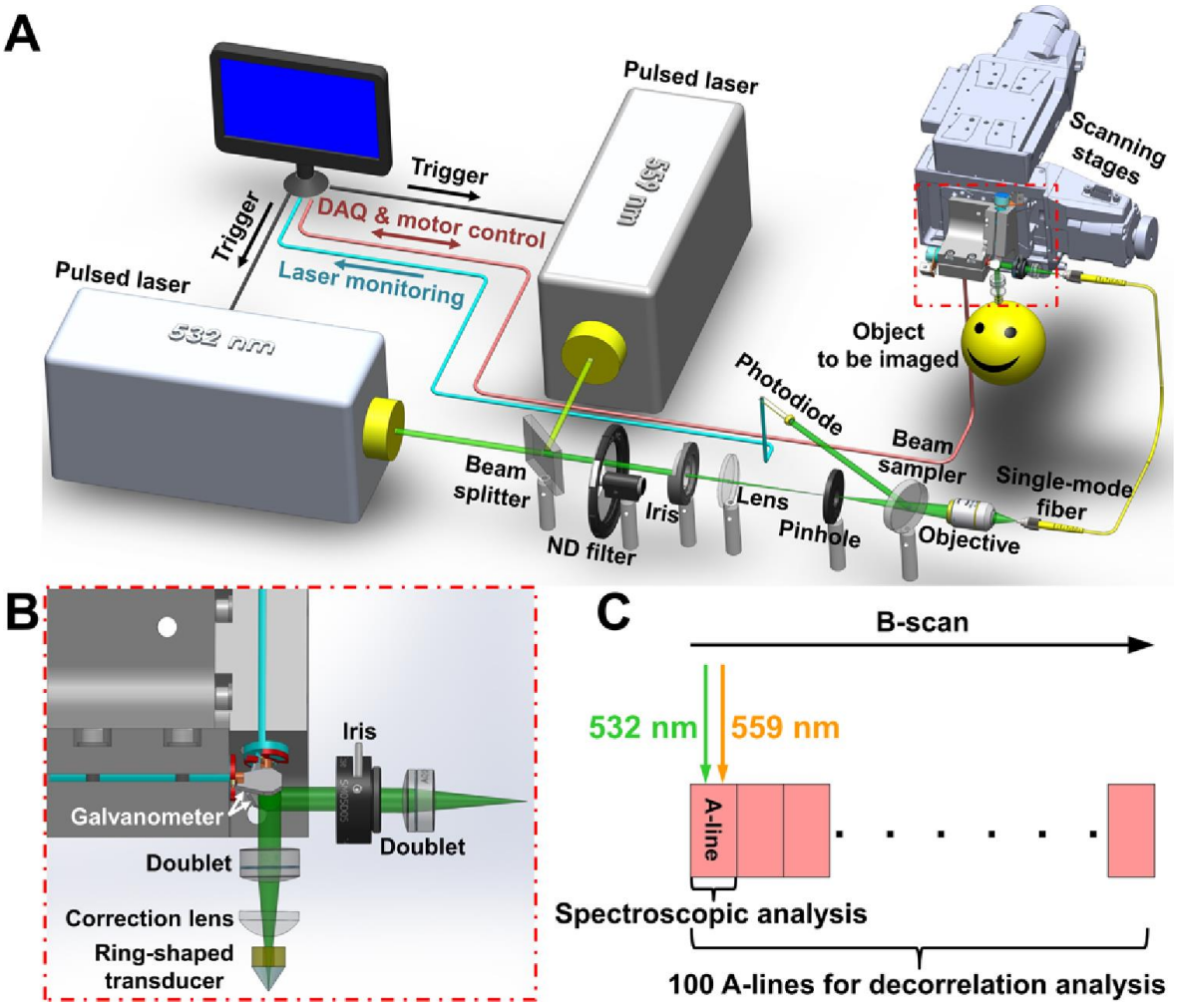

Fig. 2.4 Multi-parametric PAM platform. (a) System schematic (DAQ=data acquisition; ND=neutral density). (b) Blow-up of the scan head boxed in 1(a). (c) Scanning mechanism for simultaneous acquisition of vascular anatomy, oxygen saturation, and blood flow. Reprinted from the reference (25).

The scan head is mounted on a two-axis motorized linear stage (PI miCos GmbH, PLS-85) for raster scanning. A speed of 1 mm/s is set for the cross-sectional scan (B-scan), during which the two lasers are alternately triggered at a 50-μs interval to produce dual-wavelength A-line pairs (Fig. 2.4C). Spectroscopic analysis of these pairs leads to pixel-wise quantification of normalized C_{Hb} and absolute sO_2. In the same B-scan, each A-line is respectively correlated with 100 successive A-lines

acquired at the same wavelength to extract the flow-induced temporal decorrelation of the photoacoustic signal. Given the 100-μs interval between adjacent A-lines of the same wavelength, the time window for computing decorrelation is 10 ms. Within this window, the scan head travels only 10 μm along the B-scan direction, which is comparable to the average diameter of capillary—the smallest vessel in vivo. Thus, our platform is able to measure the blood flow in any single vessel, regardless of its orientation in respect to the scanning direction.

2.2.2 System Performance

The optically defined lateral resolution of PAM was characterized using a resolution target (R1DS1P, Thorlabs). As shown in Fig. 2.5a, our platform clearly resolved the 6th element of Group 7. By fitting the experimentally measured modulation transfer function (MTF) to the theoretical MTF of a "perfect" optical system, we estimated the cutoff spatial frequency to be 365.4 line pair/mm, corresponding to a lateral resolution of 2.7 μm. Although slightly worse than the diffraction-limited resolution (2.0 μm), it is sufficient to resolve single capillaries. The acoustically defined axial resolution of PAM was estimated by imaging a 7-μm carbon fiber (S-CF706-T700, CST), whose diameter is much smaller than the acoustic wavelength and thus serves as an "ideal" line target. The full-width at half-maximum (FWHM) value of the temporal envelope of the A-line photoacoustic signal was measured to be 31 ns (Fig. 2b), corresponding to an axial resolution of 46.4 μm (theoretically 38.0 μm).

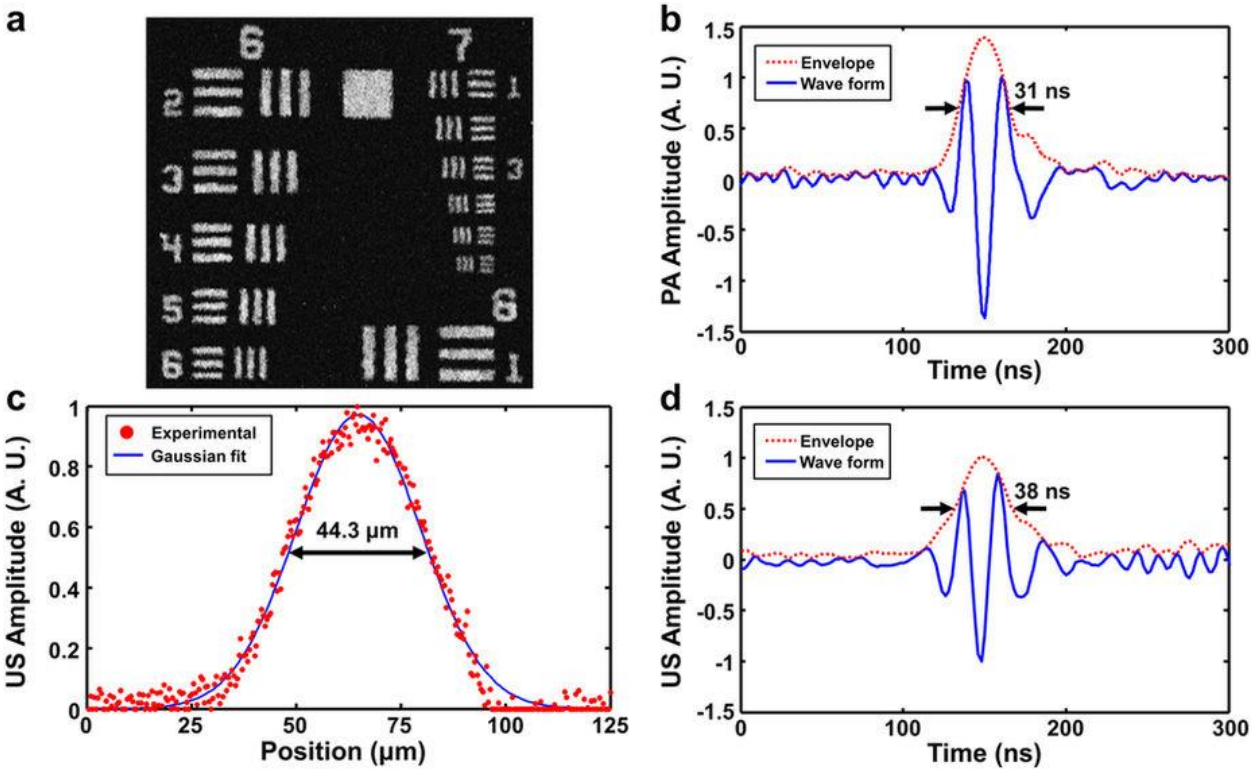

Fig. 2.5 (a) Lateral resolution of PAM quantified using a resolution target. (b) Axial resolution of PAM quantified by the FWHM value of the A-line photoacoustic envelope of a 7-μm carbon fiber. (c) Lateral resolution of SAM quantified by the FWHM value of the Gaussian-fitted cross-sectional profile of the same carbon fiber. (d) Axial resolution of SAM quantified by the FWHM value of the A-line ultrasonic envelope of the carbon fiber. Reprinted from the reference (33).

2.2.3 Multi-parametric PAM of Mouse Ear

Capitalizing on the near-optical-diffraction-limited lateral resolution and elegant sensitivity to hemoglobin, our multi-parametric PAM platform successfully demonstrated simultaneous mapping of vessel diameter, sO_2, and blood flow down to the capillary level [Figs. 2.6a–c]. Individual red blood cells (RBCs) flowing through a capillary were clearly resolved [insets in Figs. 2.6a–c], showing an RBC diameter of 6.7±2.6 μm, sO_2 of 0.48±0.07, and speed of 0.37±0.13 mm/s. Moreover,

the three major arteries could be clearly distinguished from their paired veins based on the marked difference in diameter, sO2, and flow speed. Using vessel segmentation technique, we were able to trace the dynamic changes in diameter, sO_2, and flow speed along with bifurcations in the arterial and venous trees all the way down to pre-capillary arterioles and post-capillary venules [Figs. 2.6d–f]. Combining the average diameter and flow speed of each vessel segment between two adjacent bifurcations, we further computed the volumetric blood flow of each segment in absolute values. The inflow and outflow rates at each of the 15 bifurcations showed good agreement with each other [Fig. 2.6g], which implies that our quantitative anatomical and flow measurements are accurate.

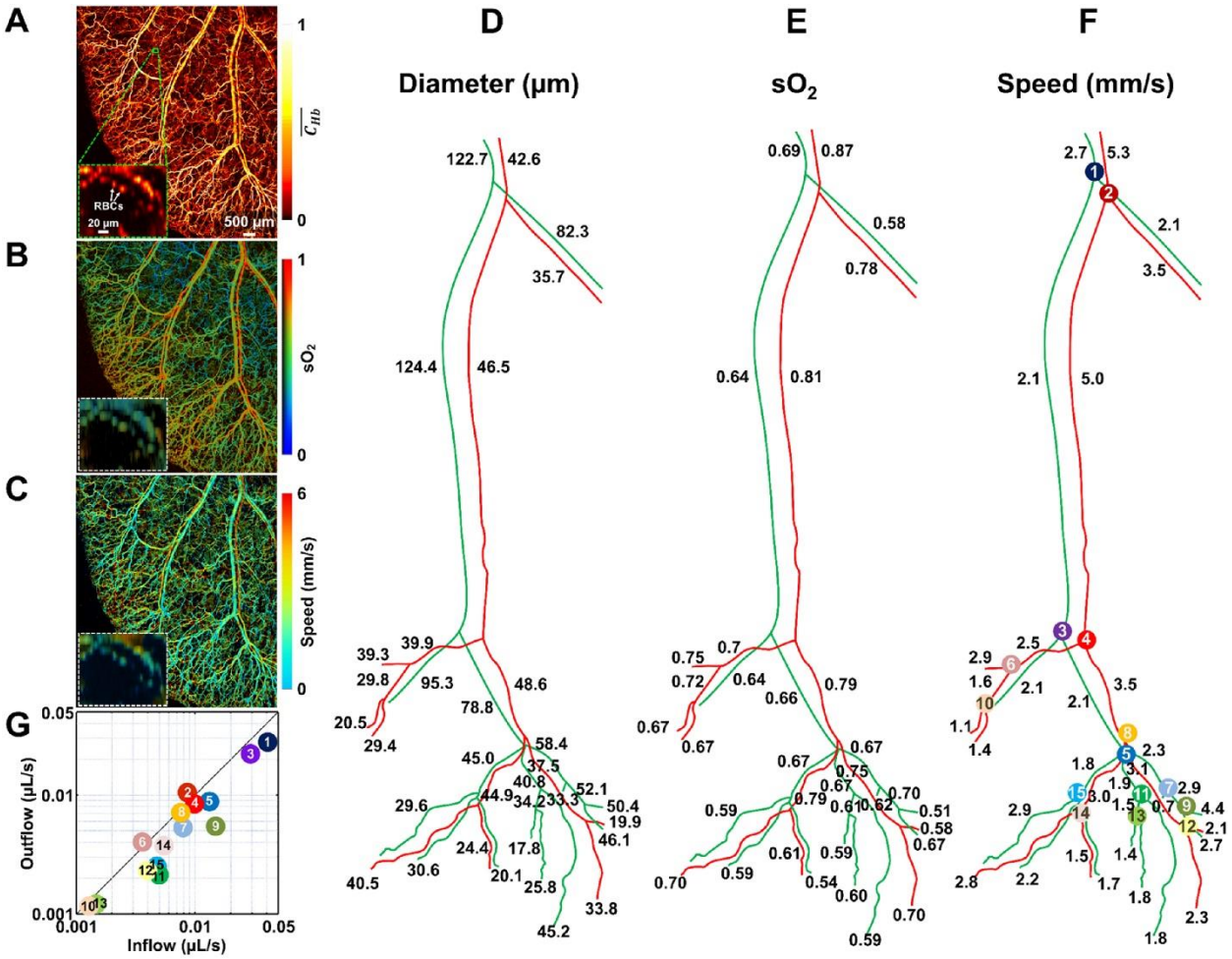

Fig. 2.6 Simultaneous PAM of (a) vascular anatomy (delineated by the distribution of normalized C_{Hb}), (b) oxygen saturation of hemoglobin (sO_2), and (c) blood flow speed in a nude mouse ear in vivo. Vessel segmentation reveals dynamic changes in (d) vessel diameter, (e) sO_2, and (f) flow speed, along with bifurcations in the paired arterial and venous trees. (g) Conservation of the volumetric inflow and outflow rates at each bifurcation. Reprinted from the reference (25).

2.2.4 Ultrasound-aided Multi-parametric PAM of Mouse Brain

This section was modified and reprinted with permission from "Ultrasound-aided multi-parametric photoacoustic microscopy of the mouse brain." Scientific reports 5 (2015): 18775. Bo Ning, Naidi Sun, and I designed and built the photoacoustic microscopy system. Bo Ning performed the animal experiments and data analysis.

With the ultrasonically extracted contour map of the mouse skull, our PAM can dynamically focus on the underlying cortical vasculature when scanning across the uneven brain surface to maintain high spatial resolution and sensitivity. To maintain high resolution and sensitivity for accurate quantification of C_{Hb}, sO_2, and CBF in the uneven mouse brain, we have expanded the contour PAM technique that was recently developed to address the out-of-focus issue in imaging the tumor-bearing mouse ear. Following the surface contour of the tumor outlined by its densely packed vasculature in a pre-scanned photoacoustic image, the contour PAM can dynamically adjust the focal plane to accommodate the uneven tumor surface. Although encouraging, this technique is not directly applicable to the mouse brain, because skull vessels could be easily misidentified as cortical vessels and adversely influence the detection of the cortical contour. To address this challenge, we have integrated scanning acoustic microscopy (SAM) in our platform. Compared with the previous implementation[42], our ultrasound-aided contour PAM relies on direct

pulse-echo imaging of the skull-cortex interface rather than inaccurate interpolation based on discretely distributed brain vessels. Moreover, the much larger depth of focus of SAM allows more reliable detection of the surface contour of the dome-shaped mouse cortex, which spans several hundred microns along the depth direction.

We have designed a novel scanning scheme to simultaneously acquire the hemodynamic and anatomical information of the mouse brain. Specifically, the B-scan speed is set to 1 mm/s, during which the two lasers are alternately triggered at a 50-μs interval to produce dual-wavelength photoacoustic A-line pairs with a spatial interval of 0.1 μm. Statistical, spectral, and correlation analysis of 100 successive A-line pairs allows simultaneous quantification of C_{Hb}, sO_2, and CBF at the same spatial scale (10 μm). With 200 pairs of dual-color laser pulses, an ultrasonic pulse (energy: 1 μJ) is fired for pulse-echo imaging. The corresponding step size of SAM is 20 μm, which is about half of its lateral resolution.

We tested the performance of our ultrasound-aided contour scan using a plastic ball coated with black ink (diameter: 20 mm). First, as shown in Fig. 2.7a, the surface contour of the ball was extract by a rapid SAM scan. Then, a pair of PAM images with (Fig. 2.7b) and without (Fig. 2.7c) ultrasound-aided contour scan were acquired for comparison. Visibly, the sphere-shaped ball surface shown in the conventional PAM image became flat in the contour image, due to the dynamically adjusted focal plane. Moreover, the top surface and lower periphery of the ball—which were out of focus and thus dim and fuzzy in the conventional PAM image—became bright and clear in the contour image, indicating the improvement in both sensitivity and spatial resolution.

Following the phantom study, we further tested the system performance *in vivo*. Similarly, a $6 \times 8\,mm^2$ region of the mouse brain was imaged by SAM to map the skull contour (Fig. 2.7d). Then, the same region of interest was imaged by our dual-contrast platform with and without the contour guidance. Since PAM and SAM shared the same acoustic detection, the concurrently acquired photoacoustic and ultrasonic images were automatically co-registered and readily fusible. As shown in Fig. 2.7e, the entire mouse skull (imaged by SAM) and underlying cortical vasculature (image by PAM) are visually flat, due to the contour-guided dynamic focusing. Better maintaining the spatial resolution and sensitivity, the contour scan clearly resolved the microvasculature near the junction of parietal and temporal cortices, which were out of the focal plane of conventional PAM (Fig. 2.7f).

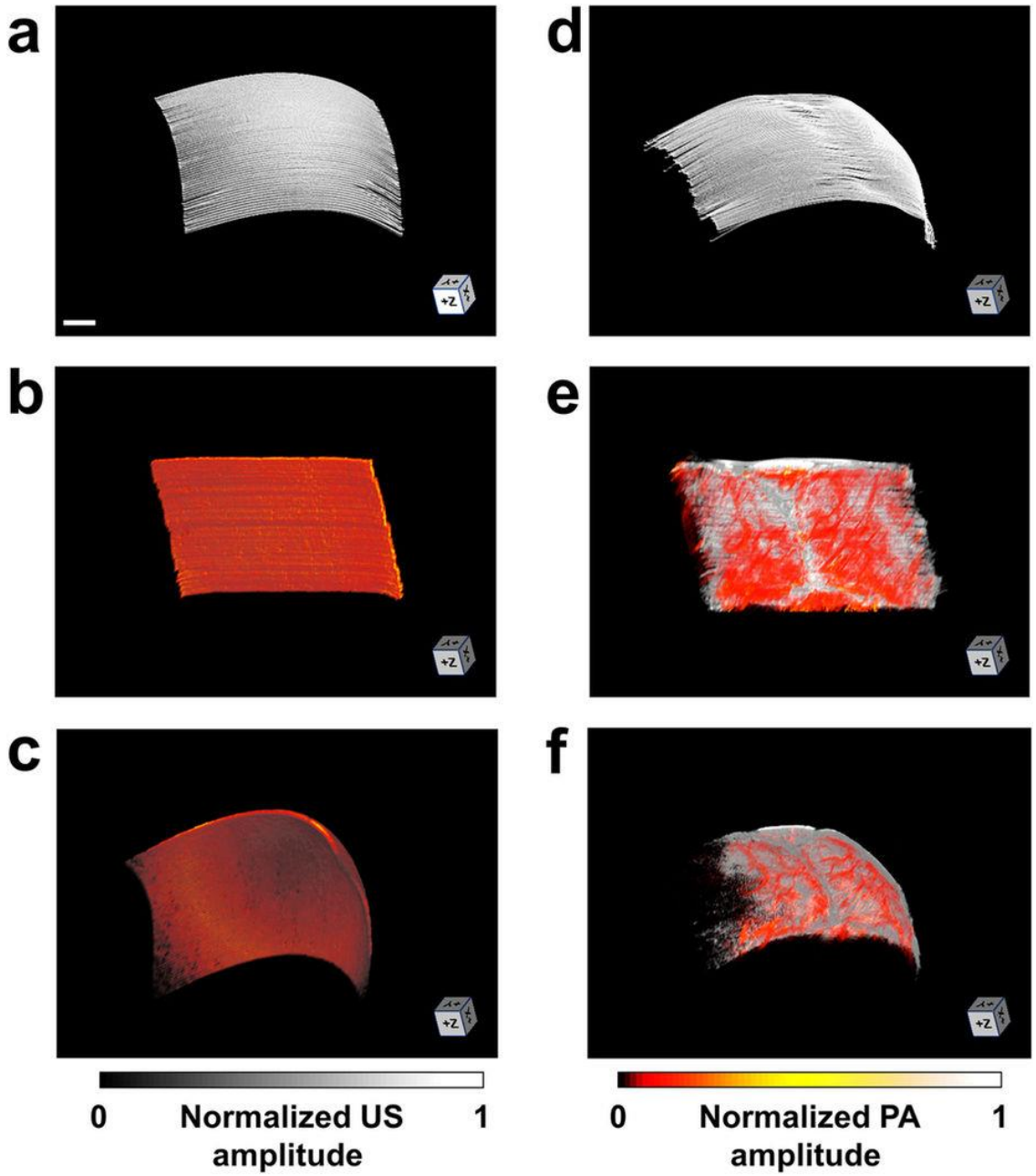

Fig. 2.7 (a) Screenshot of the 3D surface contour of the plastic ball extracted by SAM. (b,c) Screenshots of the 3D rendering of the surface of the ball imaged by PAM with and without the contour scan, respectively. (d) Screenshot of the 3D surface contour of the mouse skull extracted by SAM. (e,f) Screenshots of the 3D rendering of the mouse brain simultaneously imaged by SAM (gray) and PAM (hot)

with and without the contour scan, respectively. Scale bar: 1 mm. Reprinted from the reference (33).

To derive the total CBF from its transverse component measured by the correlation analysis, we have developed a three-step procedure. First, the vascular skeleton is extracted from the two-dimensional maximum amplitude-projected PAM image using a built-in function of MATLAB (bwmorph) and transformed into 3D by the incorporation of corresponding depth information. Then, the vessel axis is estimated by the local slope of the vascular skeleton on a pixel basis. Finally, by computing the angle (α) formed by the vessel axis and the transverse plane (Fig. 2.8), we can derive the total CBF as:

$$CBF_{total} = \frac{CBF_{trans}}{\cos(\alpha)}, \qquad \text{(eq. 2.6)}$$

in which CBF_{trans} is the transverse component of the total flow speed.

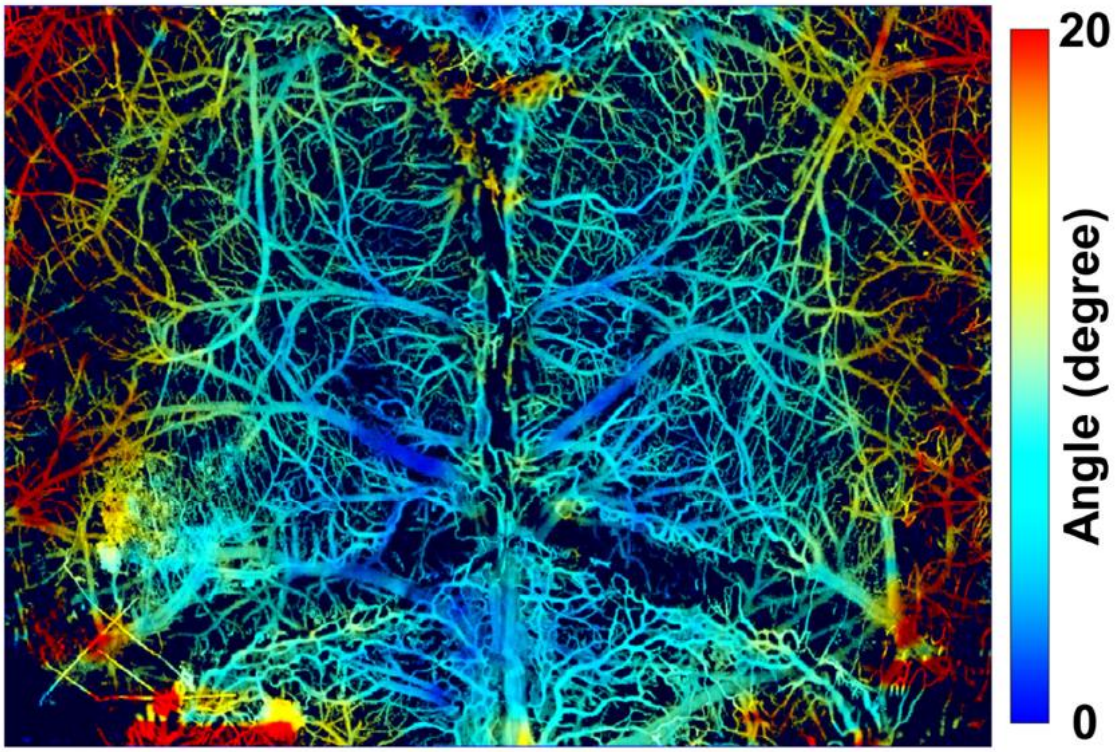

Fig. 2.8 Orientation of the brain vasculature determined by the ultrasound-aided contour PAM. The angle (α) is formed by the vessel axis and the transverse plane. The image was smoothed using the moving average window. Reprinted from the reference (33).

Then, we demonstrated—for the first time—simultaneous transcranial mapping of C_{Hb}, sO_2, and CBF over the entire mouse cortex. The vascular networks in the skull and underlying cortex were clearly separated (Fig. 2.9a). Note that the depth range (up to 400 μm) does not reflect the maximum penetration of PAM, because the maximum rather than the deepest signal is projected along each A-line. As shown in Fig. 2.9b, the average C_{Hb} was measured to be 113.7 ± 34.7 g/L. Interestingly, the average C_{Hb} value in the skull (136.1 ± 28.7 g/L) was slightly higher than that in the cortex (100.1 ± 20.8 g/L). By analyzing the 100 dual-wavelength A-line pairs acquired at 532 and 559 nm, we computed the proportions of HbO_2 and HbR in C_{Hb}, from which sO_2 was derived (Fig. 2.9c). The methodology for spectroscopic PAM of sO_2 has been established and described before[32]. As a testament to its robust performance, PAM clearly identified a pair of cortical arteriole and venule partially shadowed by the microvessels in the interparietal skull (indicated by the white arrows in Fig. 2.9c). Relying on the RBC flow-induced decorrelation between the same 100 A-lines acquired at 532 nm, PAM quantified the speed of the blood flow in individual vessels (Fig. 2.9d). It is worth noting that the blood flow in the mouse brain has both transverse and axial components, which is in contrast to the ear where blood circulates within the transverse plane (i.e., perpendicular to the imaging head). In light of this, we quantified the angle between the vessel axis and the transverse plane to derive the total CBF from its transverse component measured by the correlation analysis (see Methods for details). Taking into consideration the relative movement between the cross-sectional scanning (i.e., B-scan) stage and RBC, PAM

further determined the CBF direction by capturing the subtle difference in the relative flow speeds measured using forward and backward B-scans. As shown in Fig. 2.9d, PAM can accurately trace the direction of blood flow in individual vessels (indicated by warm and cold colors), which nicely corresponds to the sO_2 (i.e., the arterial blood flows from parent to daughter branches, while the venous blood flows oppositely). Strikingly, our PAM was able to pinpoint the direction of the blood flow in an arteriole, whose orientation was nearly orthogonal to the B-scan axis. As indicated by the white arrow in Fig. 2.9d, the two daughter branches bifurcated from the arteriole show different colors, indicating that they were flowing toward opposite directions along the B-scan axis but both away from the parent branch.

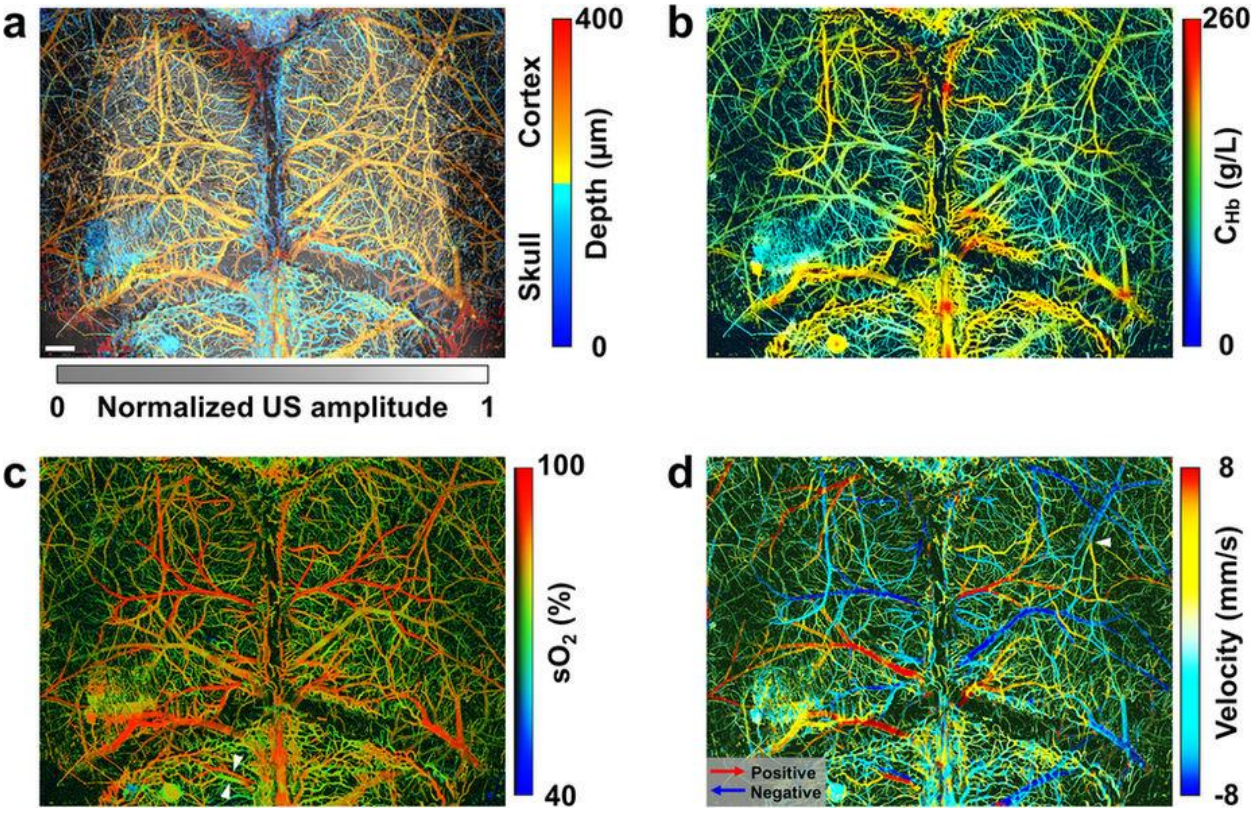

Fig. 2.9 (a) Depth-encoded skull vasculature (labeled in cold color) and cortical vasculature (in warm color) separated by the SAM-determined skull (in gray). US: ultrasound. (b–d) Simultaneously acquired high-resolution maps of C_{Hb}, sO_2, and

CBF (both speed and direction), respectively. The arrows in panel (c) indicate a pair of cortical arteriole and venule identified by their distinct sO_2 values. The red and blue arrows in panel (d) indicate the directions of the blood flow along the B-scan axis, and the white arrow indicates an arteriole whose orientation is nearly orthogonal to the B-scan axis. Scale bar: 0.5 mm. Reprinted from the reference (33).

2.3 Discussion

We have developed a multi-parametric PAM platform capable of simultaneous quantification of microvascular anatomy, oxygen saturation, and blood flow at the same spatial scale. By extending the correlation method previously reported for the low-speed capillary flow measurement, we have achieved a broad measurable range of 0.18–21 mm/s. With spectroscopic and correlation analysis, we are the first to demonstrate simultaneous wide-field PAM of vessel diameter, sO_2, and blood flow down to the capillary level in vivo. With the aid of vessel segmentation, this platform can further trace the dynamic changes in vascular anatomy and functions from trunk arteries and veins down to pre-capillary arterioles and post-capillary venules. By enabling simultaneous imaging of all the parameters prerequisite for MRO_2 quantification at the microscopic level, our multi-parametric PAM platform may shed new light on cancer and neuroscience research.

Furthermore, we have developed the ultrasound-aided multi-parametric PAM for simultaneous imaging of C_{Hb}, sO_2, and CBF—the three parameters required to derive CMRO2. The future development of complementary algorithms to extended the PAM-measured parameters from the vascular level to the tissue level will ultimately prepare us to compute microscopic $CMRO_2$ using the Fick's law. A dynamic view of the co-development of metabolic dysfunction and neuronal damage revealed by

PAM may revolutionize our current understanding of many neurological diseases and shed new light on neuroscience research.

Chapter III. Head-restraint PAM

3.1 Background and Motivation

Optical microscopy—providing detailed spatiotemporal views of neuronal networks[43], neuronal subtypes[44], subcellular compartments of neurons[45], and hemodynamics[23] in the rodent brain *in vivo*—has been revolutionizing neuroscience in recent decades. To minimize motion artifacts during the course of high-resolution imaging, the majority of these studies have been carried out in anesthetized animals. However, anesthesia is known to have profound effects on neuronal activities and cerebral hemodynamics. A recent study shows direct evidence that the brain activity during wakefulness cannot be reliably inferred from the observations under anesthesia [46]. Moreover, anesthetic-induced changes in cerebral hemodynamics have been observed across multiple species (human, primate, and rodent)[47–50]. Thus, there is a pressing need for novel microscopy technologies capable of imaging neuronal activities and hemodynamics in the awake rodent brain.

To meet this demand, head-mounted[51] and head-restrained[52–54] paradigms have been recently developed for fluorescence microscopy of the awake brain. The head-mounted approach allows imaging the neuronal activity in freely moving rodents but has limited field of view, insufficient mechanical stability, and suboptimal optical performance[55]. In contrast, head restraint provides extended imaging field, improved mechanical and optical performance, and the accessibility of electrode recording[56]. The restraint-induced animal stress, as a primary concern, can be mitigated by the use of a treadmill and proper training[52,54]. With the aid of molecular probes, these new paradigms have enabled large-scale and time-lapse recording of the neuronal

activity at the cellular level in awake mice, holding great potential to transform our understanding of neural circuits underlying behavior[53].

While molecular imaging of the neuronal activity in the awake brain rapidly advances, functional imaging of the coevolving hemodynamics falls far behind. With the aid of angiographic agents, fluorescence microscopy permits the quantification of CBF in awake mice[51]. However, it remains a challenge for fluorescence microscopy to directly measure multiple hemoglobin-related hemodynamic parameters, including C_{Hb}, sO_2, and OEF. Recent advances in oxygen-sensitive fluorescent probes[2] and visible light optical coherence tomography[57,58] provide new means to assess blood oxygenation, which in combination with CBF allows the quantification of oxygen metabolism. Capable of comprehensively and simultaneously measuring all these hemodynamic parameters in a label-free manner[18,59], photoacoustic imaging is ideally suited for functional imaging of the awake brain. However, this research is still in a nascent stage, with only a couple of studies using macroscopic-resolution photoacoustic tomography[60,61].

Here, we report on a novel application of PAM for comprehensive and quantitative characterization of cerebral hemodynamics and metabolism at the microscopic level in awake mice. An angle- and height-adjustable head-restraint apparatus was exploited to enable high-resolution PAM of the awake brain with minimal motion artifacts, and an air-floated spherical treadmill was utilized to mitigate the restraint-induced stress. We first assessed the long-term stability of head-restrained PAM measurements in the awake mouse brain. Upon validation, we compared the cerebrovascular diameter, C_{Hb}, sO_2, CBF, OEF, and $CMRO_2$ in the same region of interest under wakefulness and different levels (i.e., light, medium, and deep) of anesthesia, which revealed dose-dependent cerebral hemodynamic and metabolic responses to isoflurane—a commonly used volatile general anesthetic. We further

studied the multifaceted cerebral responses under systemic hypoxia, whose results suggested a possible mechanism for the widely reported but poorly understood neuroprotective effect of volatile anesthetics[62,63].

This section was modified and reprinted with permission from "Functional and oxygen-metabolic photoacoustic microscopy of the awake mouse brain." Neuroimage 150 (2017): 77-87. I designed and built this imaging system and head-restraint apparatus. I performed the animal experiments and data analysis for this study.

3.2 Design and Implementation of the Head-restraint PAM

3.2.1 System Schematic and Apparatus Design

As shown in Fig. 3.1, the head-restrained PAM uses two nanosecond-pulsed lasers (BX40-2-G and BX40-2-GR, Edgewave) operating at the same pulse repetition rate of ~10 kHz. The two beams with orthogonal polarizations are combined by a polarizing beam splitter (48–545, Edmund Optics) and then coupled into a single-mode optical fiber (P1-460B-FC-2, Thorlabs) through a microscope objective (M-10X, Newport). Before entering the fiber, the dual-wavelength (i.e., 532 nm and 559 nm) beam is attenuated by a neutral density filter (NDC-50 C-2M, Thorlabs), reshaped by an iris (SM1D12D, Thorlabs), focused by a condenser lens (LA1608, Thorlabs), and filtered by a 50-μm-diameter pinhole (P50C, Thorlabs). To compensate for the fluctuation in the laser intensity, ~5% of the laser pulse energy is picked off by a beam sampler (BSF10-A, Thorlabs) and monitored by a high-speed photodiode (FDS100, Thorlabs). The beam coming out of the fiber is launched into the imaging head of the system, where it is collimated by an achromatic doublet (AC127-025-A, Thorlabs), reshaped by an iris (SM05D5, Thorlabs), and focused by

an identical doublet through a correction lens (LA1207-A, Thorlabs) and the central opening of a customized ring-shaped ultrasonic transducer (inner diameter: 2.2 mm; outer diameter: 4.0 mm; focal length: 6.0 mm; center frequency: 35 MHz; 6-dB bandwidth: 70%) into the mouse brain. The optical and acoustic foci are confocally aligned for maximum sensitivity. Restraint of the awake mouse head is achieved using a nut-bolt configuration. As shown in the red-boxed inset of Fig. 3.1, a small nut (90730A005, McMaster-Carr) is attached to the exposed mouse skull using dental cement (S380, Parkell). Once being fixed in a customized head plate with a bolt, the mouse head can be angularly adjusted using a rotation mount (RSP-1T, Newport) to align the region of interest perpendicular to the imaging head and vertically adjusted using a right-angle clamp (RA90, Thorlabs) to allow the mouse limbs to comfortably rest on the surface of the spherical treadmill (blue-boxed inset of Fig. 1). The treadmill, consisting of two 8-inch-diameter hollow polystyrene hemispheres (03170-1008, Blick Art Materials), sits in a homemade cylindrical holder. The slightly compressed air (15 psi) from the bottom of the holder creates a thin cushion to float the treadmill, allowing the mouse to move freely with reduced reaction force.

To scan the optical-acoustic dual foci over the cortical region of interest, the exit end of the optical fiber and the imaging head are mounted on a 3-axis motorized scanning system, which consists of two transverse linear stages (PLS-85, PI miCos GmbH) for raster scan and a vertical linear stage (KR15, THK; motor: 28BYG201, Circuit Specialists) for automatic and precise adjustment of the dual foci. The cross-sectional scan (i.e., B-scan) speed is set to 1 mm/s, during which the two lasers are alternately triggered at a 50-μs interval to produce dual-wavelength A-line pairs with a spatial interval of 0.1 μm. Statistical, spectral, and correlation analysis of 100

successive A-line pairs[33] allows simultaneous quantification of C_{Hb}, sO_2, and CBF at the same spatial scale (10 μm).

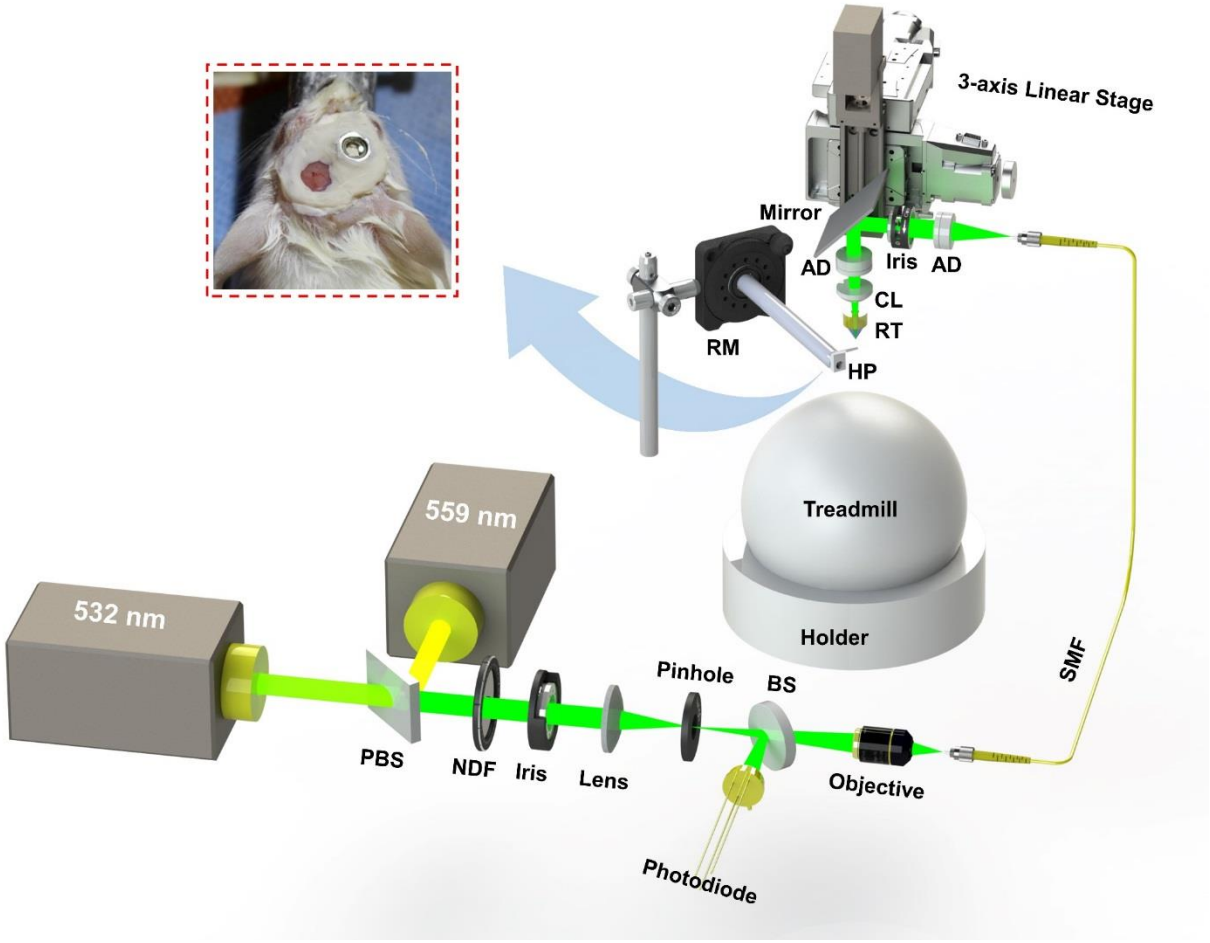

Figure 3.1 Schematic of the head-restrained PAM. PBS, polarizing beam splitter; NDF, neutral density filter; BS, beam sampler; SMF, single-mode fiber; AD, achromatic doublet; CL, correction lens; RT, ring-shaped ultrasonic transducer; RM, rotation mount; HP, head plate. Red-boxed inset: photograph of a mouse brain with a thinned-skull window and a nut attached using dental cement.

3.2.2 Animal Preparation

Male CD-1 mice (9–13 weeks old, Charles River Laboratories) were used for the studies. Under anesthesia, the hair in the mouse head was removed and a surgical incision was made in the scalp to expose the skull. The dental cement was then applied to cover the surface of the exposed skull, except for the region of interest, and the nut was attached. After the cement was solidified and the nut was firmly adhered to the skull, the mouse was transferred to the head-restrained apparatus. To help acclimate the mouse to head restraint and attenuate the stress, each mouse was subjected to 5 training sessions on 5 consecutive days. Each session lasted for 45 minutes, during which the mouse was provided with drink as a positive reward.

One day before the PAM experiment, the skull over the region of interest was thinned by a surgical hand drill following the fascia removal for optimal image quality. The skull thinning was implemented following the well-established protocol[64,65] to alleviate potential inflammation and avoid possible damage to the brain. Once the desired skull thickness (~100 μm) was reached, the thinned-skull window was cleaned and dried. According to previous studies[64], no obvious inflammation or detectable microglia activation is expected if the thickness of the thinned skull is larger than 20 μm. One hour prior to the PAM experiment, the trained mouse was restrained and placed beneath the water tank for acoustic coupling (green-boxed inset of Fig. 1). Ultrasound gel was applied between the skull window and the ultrasonically and optically transparent polyethylene membrane at the bottom of the water tank. The temperature of the water tank was set at 37°C, and a heating lamp was used to help maintain the mouse body temperature. All experimental procedures were carried out in conformity with the animal protocol approved by the Animal Care and Use Committee at the University of Virginia.

3.3 PAM of the Awake Mouse Brain

3.3.1 Long-term Stability

Prior to characterizing the cerebral hemodynamic and oxygen-metabolic responses to isoflurane, we assessed the stability of head-restrained PAM for time-lapse measurements in the awake mouse brain to ensure that PAM-revealed changes were indeed due to physiological rather than technical variations. Specifically, we repeatedly imaged the same cortical region of interest 5 times over a 75-minute period, during which the physiological state of the mouse was carefully maintained. A total of 48 feeding arteries and draining veins that PAM imaged in 3 mice were segmented, and the relative changes in C_{Hb}, sO_2, vessel diameter, and blood flow speed from their corresponding baseline values measured at the very beginning were quantified. As shown in Fig. 3.2, the statistical analysis showed no significant changes in any of the four parameters over time, indicating the stability of our system.

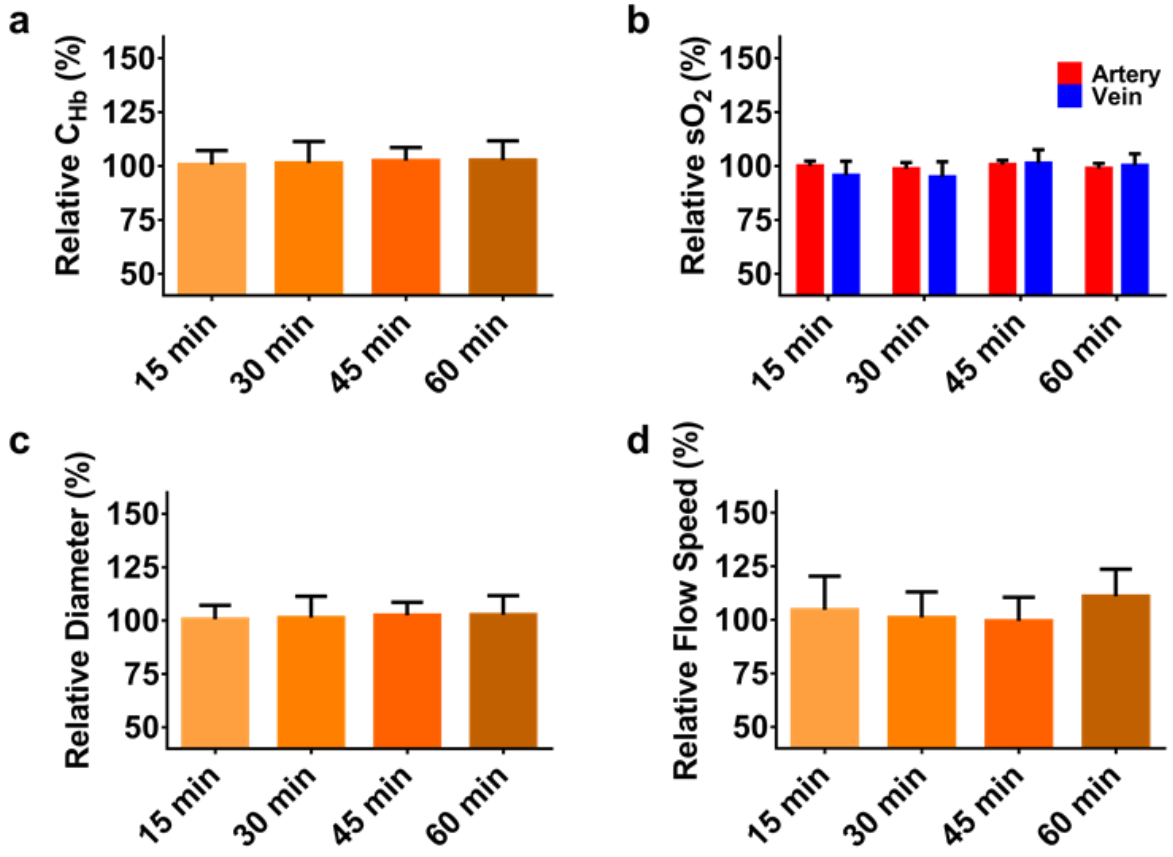

Figure 3.2 Long-term stability of the head-restrained PAM of (a) C_{Hb}, (b) sO_2, (c) vessel diameter, and (d) blood flow speed in the awake mouse brain. The multi-parametric PAM measurements were repeatedly taken over a 75-minute period, and each scan took ~15 minutes. The relative values were derived by normalizing to their corresponding baselines measured at the beginning (i.e., 0 min). Statistical analysis (20 feeding arteries and 28 draining veins in 3 mice) showed no significant changes in any of the four parameters over the entire monitoring period. Data are presented as mean ± SD.

3.3.2 Repeatability

Upon validating the stability of head-restrained PAM for longitudinal and quantitative monitoring, we comprehensively characterized the cerebral

hemodynamic and oxygen-metabolic responses to isoflurane under normoxia. For side-by-side comparison of the mouse brain in the absence and presence of isoflurane, we performed a 2-hour PAM monitoring, during which the isoflurane vaporizer (set at 1.0 MAC) was switched off and on. After each switch, at least 15 minutes was waited to ensure the equilibrium.

Under anesthesia, the mouse brain presented no evident changes in C_{Hb} but apparent upregulations in s_vO_2 and flow speed (indicated by the arrows in the 2nd and 3rd rows of Fig. 3.3a). Furthermore, vessel segmentation-enabled analysis of the feeding arteries and draining veins (colored in red and blue, respectively, in Fig. 3.3b) provided quantitative and more comprehensive insights into the cerebral responses to isoflurane (Fig. 3.3c). As expected, the C_{Hb} in both the arteries and veins remained roughly constant during the alternations between wakefulness and anesthesia. Similarly, the s_aO_2 maintained at a stable level, which was in striking contrast to the markedly increased s_vO_2 in the presence of isoflurane. The high s_aO_2 indicated sufficient oxygen supply to the mouse brain, while the elevated s_vO_2 suggested reduced oxygen extraction of the cerebral tissue under anesthesia. In contrast to the decreased OEF, both the feeding and draining vessels underwent significant vasodilation and upregulation in the blood flow speed, which together should lead to a boost in CBF according to Equation 4. Indeed, the total volumetric flow rates (CBF_{total}) of both the arterial blood into the region of interest and the venous blood out of it nearly doubled under anesthesia. Notably, the two rates were almost identical throughout the monitoring period. Thus, the total $CMRO_2$ of the region can be derived by Equation 5 without possible bias induced by the unbalanced flow. Apparently, the reduced OEF and increased CBF exerted opposite effects on the cerebral oxygen metabolism. The combined effects resulted in a significant suppression of $CMRO_2$ in the anesthetized mouse brain.

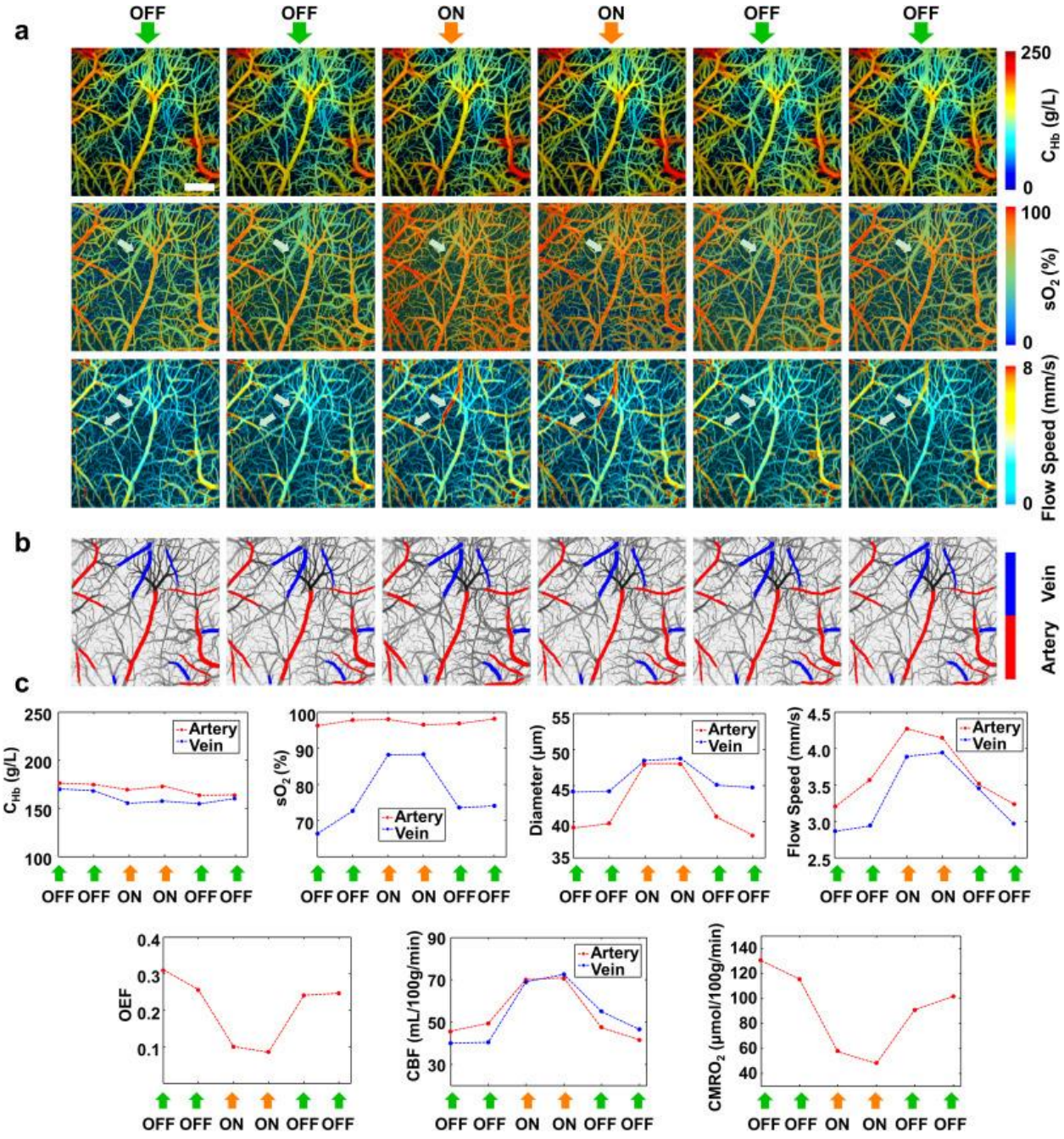

Fig. 3.3 Hemodynamic and oxygen-metabolic responses of the normoxic mouse brain to 1.0-MAC isoflurane. (a) Head-restrained PAM of cerebral C_{Hb}, sO_2, and blood flow speed in the absence (OFF) and presence (ON) of isoflurane. The white arrows in the 2nd and 3rd rows highlight the isoflurane-induced changes in s_vO_2 and blood flow speed. (b) Feeding arteries and draining veins identified and isolated by

vessel segmentation. (c) Quantitative analysis of the isoflurane-induced changes in the average C_{Hb}, sO_2, diameter, and flow speed of the feeding and draining vessels, from which OEF, CBF, and $CMRO_2$ of the region of interest under wakefulness and anesthesia were derived. Scale bar, 500 μm.

3.3.3 Quantitative Comparison between Awake and Anesthetized Brain

Repeating this experiment in 5 mice enabled us to characterize the cerebral hemodynamic and oxygen-metabolic responses to isoflurane at the statistical level. As shown in Fig. 3.4, no statistical difference was found between the C_{Hb} under wakefulness (160±7 g/L for arteries and 165±19 g/L for veins) and that under anesthesia (165±8 g/L for arteries and 162±11 g/L for veins). In contrast to the unchanged s_aO_2 (94±2% and 94±4% under wakefulness and anesthesia, respectively), s_vO_2 was increased from 65±4% to 86±6% following the exposure to isoflurane. In addition, marked arterial dilation (from 34±4 μm to 44±4 μm) and moderate venous dilation (from 43±5 μm to 48±6 μm) were observed. Further analysis of individual vessel segments revealed a striking negative correlation ($r = -0.66$) between the relative dilation of small arteries (diameter less than 40 μm) and the baseline (i.e., under wakefulness) diameter. In contrast, arteries with larger diameters (>40 μm) and veins showed less pronounced and diameter-independent dilation (13±8% and 12±6%, respectively). Accompanying vasodilation was significant increase in the flow speed (on average, 54% in arteries and 37% in veins), which together boosted the arterial CBF_{total} from 39.2±5.7 mL/100g/min to 73.5±15.2 mL/100g/min and the venous CBF_{total} from 35.0±13.5 mL/100g/min to 66.6±27.9 mL/100g//min. The PAM-measured CBF is comparable to that measured by optical coherence tomography[39] and autoradiography[66]. Combining the multiple hemodynamic parameters, we revealed that the 1.0-MAC isoflurane induced a 73%

decrease in OEF (from 0.26±0.07 to 0.07±0.04) and a 50% decline in $CMRO_2$ (from 114.5±30.6 μmol/100g/min to 57.8±23.3 μmol/100g/min).

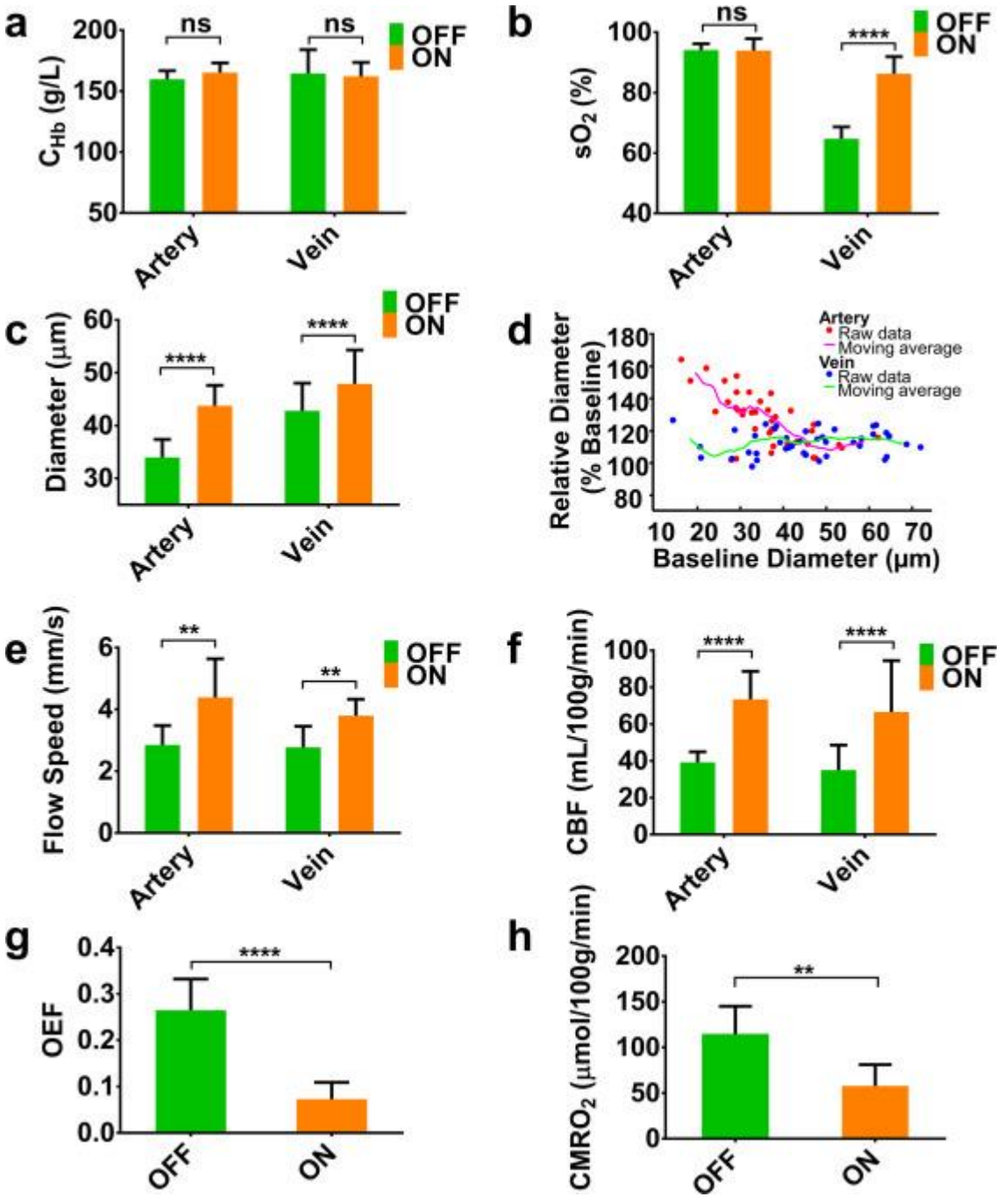

Fig. 3.4 Statistical comparison ($N = 5$) of C_{Hb}, sO_2, vessel diameter, blood flow speed, CBF, OEF, and $CMRO_2$ in the awake and anesthetized mouse brains. In the

paired *t*-test, ns, **, and **** respectively represent no significance, p<0.01, and p<0.0001. The right panel in the second row shows a strong dependence of isoflurane-induced arterial dilation on the baseline diameter measured under wakefulness. Data are presented as mean ± SD.

3.4 Effects of Anesthesia on Cerebral Hemodynamics and Metabolism

3.4.1 Dose-dependent Cerebral Response to Isoflurane under Normoxia

Next, we examined whether the observed multifaceted cerebral responses to isoflurane were dose-dependent or not under normoxia. Specifically, 6 head-restrained mice were monitored by PAM for ~2 hours, during which their states were gradually altered from wakefulness to light then medium and finally deep anesthesia by a stepwise increase of the isoflurane concentration (0, 0.5, 1.0, and 1.5 MAC). After each switch, a minimum of 15 minutes was waited to allow for equilibrium.

Consistent with the observation in Fig. 3.3a, the mouse brain showed unchanged C_{Hb} and s_aO_2 but apparently increased s_vO_2 and flow speed under all three different levels of anesthesia compared with that under wakefulness (indicated by the arrows in Fig. 3.5). With the aid of vessel segmentation, the C_{Hb}, sO_2, blood flow speed, and diameter of individual feeding arteries and draining veins were quantified and averaged for each mouse. Then, the average hemodynamic readouts under the four states were statistically compared (Fig. 3.6a and Fig. 3.7).

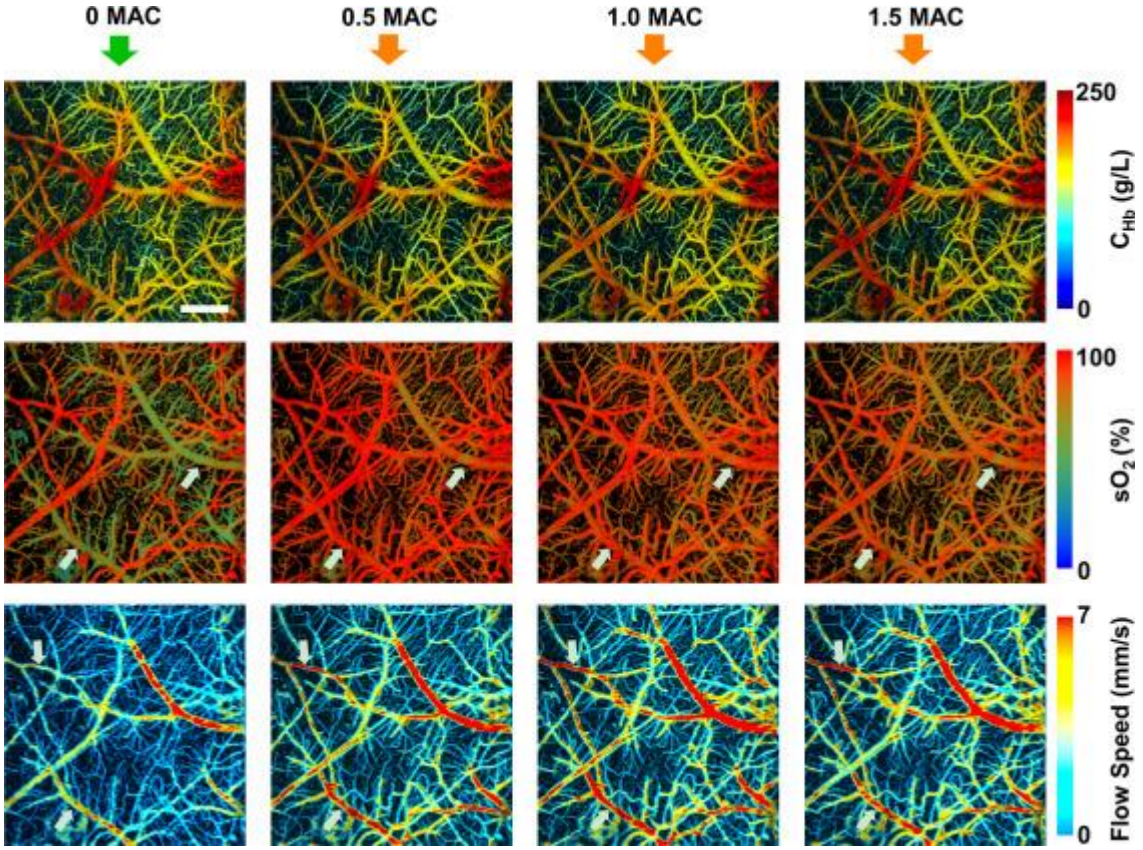

Fig 3.5 Head-restrained PAM of C_{Hb}, sO_2, and blood flow speed in the normoxic mouse brain in the absence (0 MAC) and presence of different concentrations (0.5, 1.0, and 1.5 MAC) of isoflurane. The white arrows in the 2nd and 3rd rows highlight the isoflurane-induced changes in s_vO_2 and blood flow speed. Scale bar, 500 μm.

As expected, C_{Hb} and s_aO_2 were well maintained throughout the incremental exposure to isoflurane. In contrast, marked s_vO_2 increase, flow speed upregulation, and vasodilation were observed under all three levels of anesthesia. Different from the dose-independent vasodilation, s_vO_2 and blood flow speed partially regressed when switching from medium to deep anesthesia, likely due to the anesthetic depression of myocardial contractility[67]. The synchronous responses in s_vO_2 and flow speed implied an inverse coupling between OEF and CBF. Indeed, when the state was switched from medium to deep anesthesia, $rOEF$ (normalized to the

baseline measured during wakefulness) dramatically increased from 21±8% to 37±9% along with a significant drop in $rCBF_{total}$ from 215±39% to 180±42% (Fig. 3.6b). Given the unchanged C_{Hb} and s_aO_2, the tight CBF-OEF coupling managed to maintain $CMRO_2$ at a statistically constant level—only about half of that under wakefulness—across different depths of anesthesia.

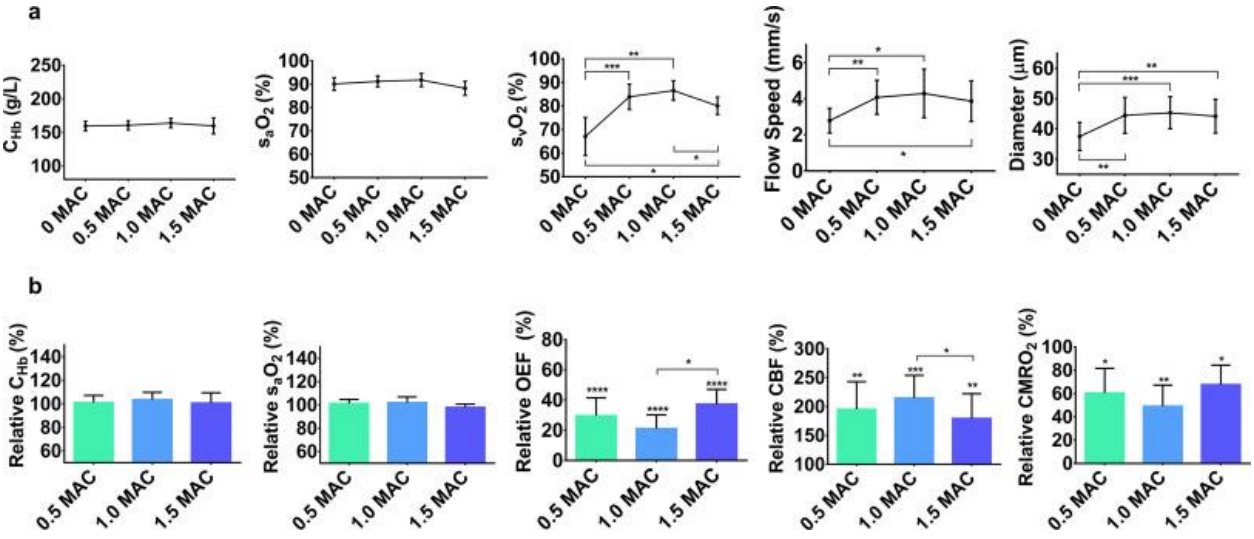

Fig. 3.6 Dose-dependent effects of isoflurane on cerebral hemodynamics and oxygen metabolism. (a) Statistical comparison ($N = 6$) of the absolute arterial C_{Hb}, sO_2, blood flow speed, and diameter, as well as s_vO_2, under wakefulness (0 MAC) and different concentrations (0.5, 1.0, and 1.5 MAC) of isoflurane. (b) Statistical comparison of the relative C_{Hb}, s_aO_2, OEF, CBF, and $CMRO_2$ with their corresponding baselines (significance levels, if any, are marked on the top of the columns) and between different concentrations of isoflurane (significance levels, if any, are marked between the two compared columns). *, p<0.05; **, p<0.01; ***, p<0.001; ****, p<0.0001. Data are presented as mean ± SD.

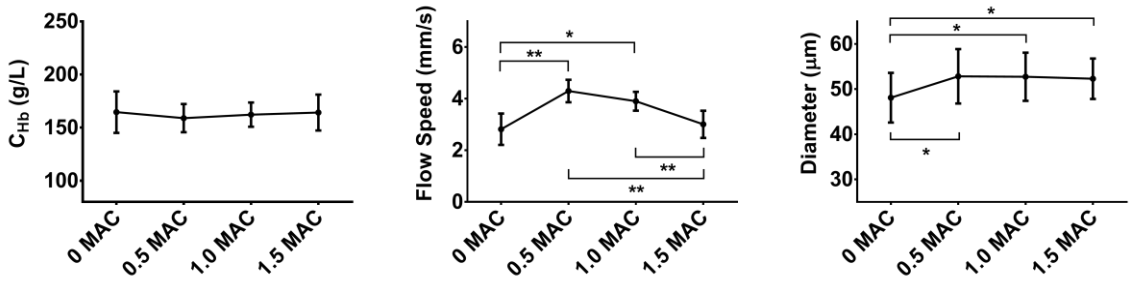

Fig. 3.7 Statistical comparison (N=6) of the venous C_{Hb}, blood flow speed, and diameter under wakefulness (0 MAC) and different concentrations (0.5, 1.0, and 1.5 MAC) of isoflurane in the normoxic mouse brain. *, $p<0.05$; **, $p<0.01$. Data are presented as mean ± SD.

It is worth noting that we did not observe the isoflurane dose-dependent $CMRO_2$ decrease reported in a previous study[68]. The discrepancy might be attributed to the differences in animal species (dog vs. mouse) and experimental conditions. Unlikely the previous study, which used active ventilation (P_aCO_2 was maintained roughly constant) with hyperoxic inhalation gas (40% oxygen), we used medical-quality air without ventilation. Thus, deep anesthesia-induced respiratory depression may lead to hypercapnia. While the cerebral metabolic response to hypercapnia is still in controversy[69], previous studies have shown that hypercapnia can induce $CMRO_2$ increase in rodents[70]. The metabolic effect of hypercapnia may counterbalance and thereby diminish the dose-dependent effect of isoflurane on $CMRO_2$.

Considering the diameter-dependent dilation of small arteries (<40 μm in diameter) revealed in Fig. 3.4, we further analyzed whether the dilation of this subset of vessels had any dependence on isoflurane concentration. To this end, we divided the segmented vessels into four groups, including small arteries (<40 μm in diameter), small veins (<40 μm in diameter), large arteries (>40 μm in diameter), and large veins (>40 μm in diameter). As shown in Fig. 3.8, all four groups showed statistically

significant vasodilation in comparison with their baselines and the diameter-dependent arterial dilation was observed under all three levels of anesthesia. However, no dose-dependent effect of isoflurane on vasodilation was observed in any of them at the three clinically relevant concentrations.

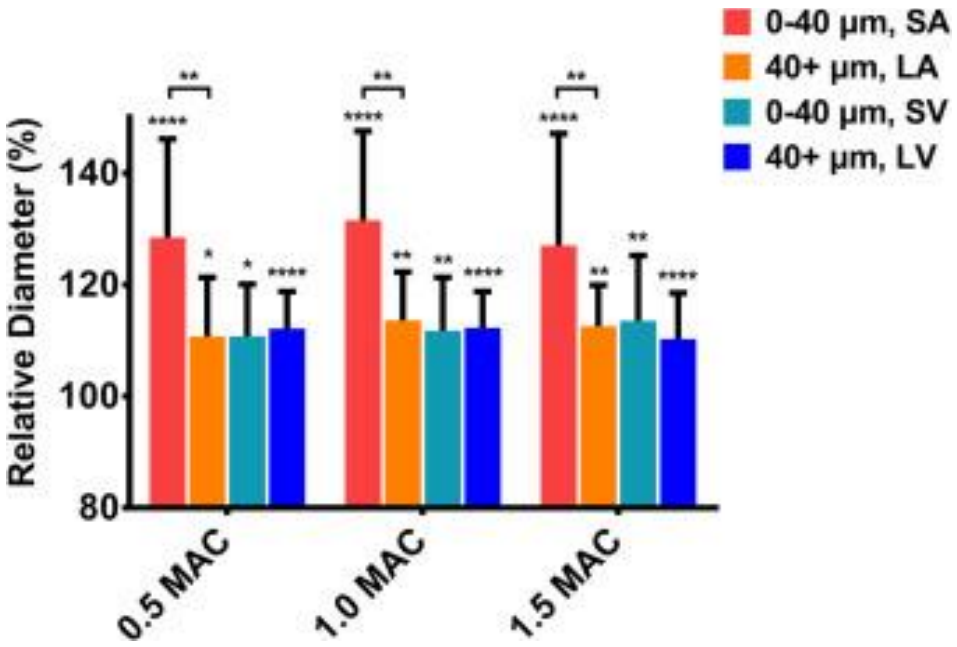

Fig. 3.8 Cerebral vasodilation in response to different concentrations of isoflurane (0.5, 1.0, and 1.5 MAC) under normoxia. The segmented feeding arteries and draining veins were divided into four different groups: small arteries (SA) and small veins (SV) with diameters less than 40 µm and large arteries (LA) and large veins (LV) with diameters larger than 40 µm. Statistical comparison (39 feeding arteries and 42 draining veins in 6 mice) of the vessel diameters measured under anesthesia with their corresponding baseline values measured under wakefulness shows significant vasodilation for all four groups across all three different anesthetic depths (significance levels are marked on the top of the columns). Moreover, statistical comparison between different groups of vessels under the same concentration of isoflurane shows a strong diameter-dependent vasodilation in the arteries but not veins (significance levels, if any, are marked between the two compared columns).

Vasodilation shows no statistically significant dependence on isoflurane concentration. *, $p<0.05$; **, $p<0.01$; ****, $p<0.0001$. Data are presented as mean ± SD.

3.4.2 Anesthetic Neuroprotection against Brain Hypoxia

The anesthesia-induced profound reduction in $CMRO_2$, as revealed by the head-restrained PAM in the normoxic mouse brain, suggested the potential of using isoflurane to protect the brain against hypoxia or ischemia. To gain more direct, quantitative, and comprehensive insights, we examined the influence of different concentrations of isoflurane on the multifaceted cerebral responses to systemic hypoxia. Similar to the normoxia study, 5 mice were monitored for ~2 hours under hypoxia, during which their states were altered by a stepwise increase of the isoflurane concentration (0, 0.5, 1.0, and 1.5 MAC). After each switch, a minimum of 15 minutes was waited to allow for equilibrium.

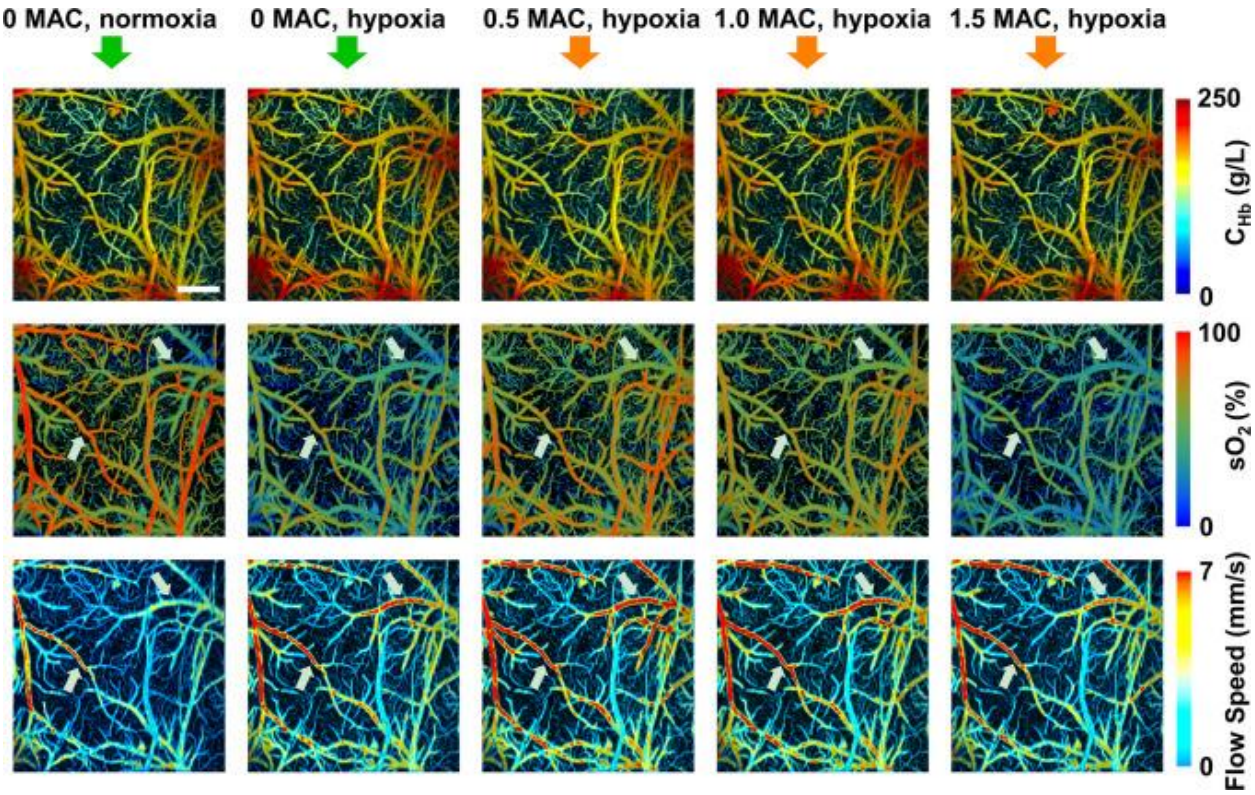

Fig. 3.9 Head-restrained PAM of C_{Hb}, sO_2, and blood flow speed in the hypoxic mouse brain in the absence (0 MAC) and presence of different concentrations (0.5, 1.0, and 1.5 MAC) of isoflurane. The white arrows in the 2nd and 3rd rows highlight the hypoxia- and isoflurane-induced changes in sO_2 and blood flow speed. Scale bar, 500 μm.

As shown in Fig. 3.9, the cerebral C_{Hb} remained unchanged when the awake mouse was switched from normoxia to hypoxia and later anesthetized with different doses of isoflurane, which was in contrast to the hypoxia-sensitive and isoflurane dose-dependent responses in sO_2 and blood flow speed. As highlighted by the arrows, the arterial and venous sO_2 dropped significantly in response to hypoxia. To compensate for the hypoxia-impaired cerebral oxygen supply, the flow speed was highly upregulated. Light anesthesia further elevated the blood flow, which partially retrieved sO_2. However, increasing the isoflurane exposure to 1.5 MAC led to

significant reduction in both sO_2 and flow speed. By segmenting the feeding arteries and draining veins, we were able to calculate the average arterial and venous C_{Hb}, sO_2, flow speed, and diameter for each mouse under both wakefulness and the three levels of anesthesia (Fig. 3.10a and supplementary Fig. 3.11).

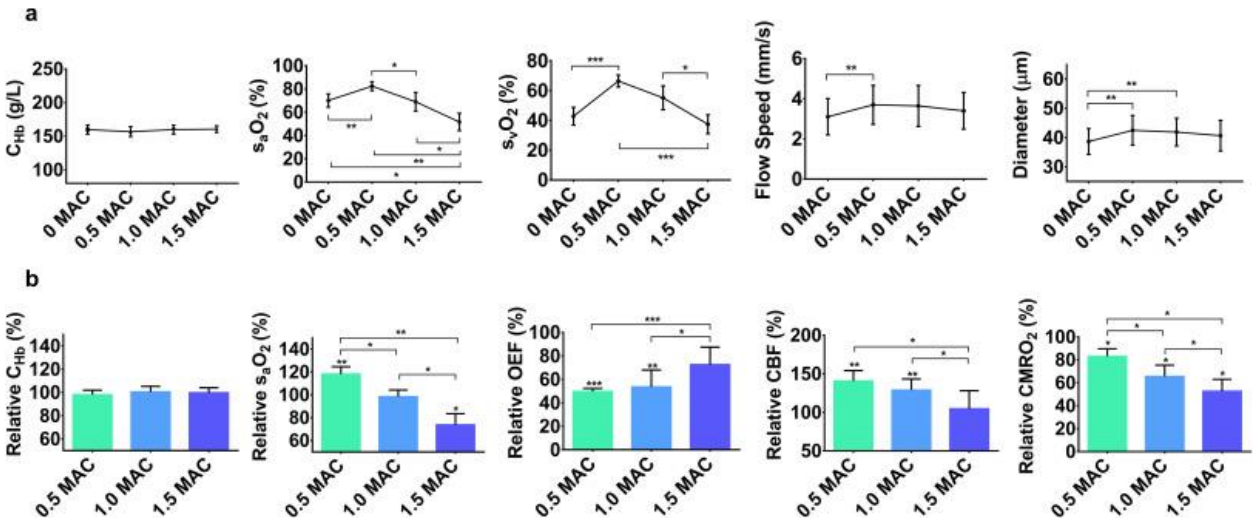

Fig. 3.10 Influence of isoflurane on cerebral hemodynamic and oxygen-metabolic responses to systemic hypoxia. (a) Statistical comparison ($N = 5$) of the absolute arterial C_{Hb}, sO_2, blood flow speed, and diameter, as well as s_vO_2, under wakefulness (0 MAC) and different concentrations (0.5, 1.0, and 1.5 MAC) of isoflurane. (b) Statistical comparison of the relative C_{Hb}, s_aO_2, OEF, CBF, and $CMRO_2$ with their corresponding baselines (significance levels, if any, are marked on the top of the columns) and between different concentrations of isoflurane (significance levels, if any, are marked between the two compared columns). *, $p<0.05$; **, $p<0.01$; ***, $p<0.001$. Data are presented as mean ± SD.

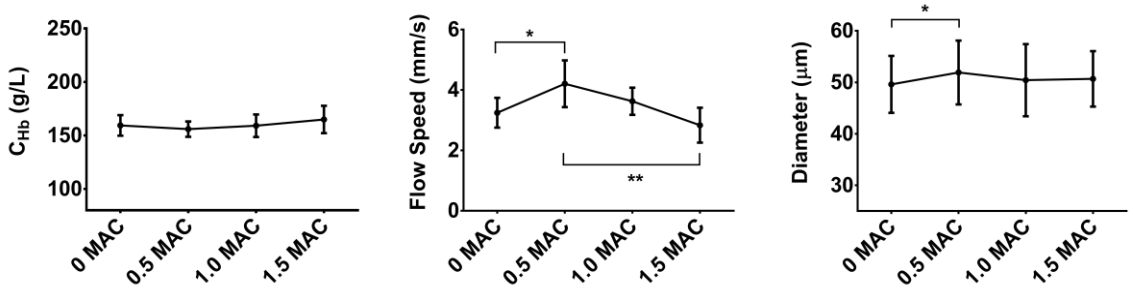

Fig. 3.11 Statistical comparison (N=5) of the venous C_{Hb}, blood flow speed, and diameter under wakefulness (0 MAC) and different concentrations (0.5, 1.0, and 1.5 MAC) of isoflurane in the hypoxic mouse brain. *, $p<0.05$; **, $p<0.01$. Data are presented as mean ± SD.

Again, C_{Hb} showed no statistically significant changes throughout the entire monitoring period. Different from that under normoxia, the average s_aO_2 in the hypoxic brain exhibited a strong dependence on isoflurane concentration, increasing from 70±6% (awake baseline) to 82±4% (0.5 MAC) and then decreasing to 69±8% (1.0 MAC) and eventually to 52±7% (1.5 MAC). The significant decrease in s_aO_2 was likely due to deep anesthesia-induced depression of respiration [71]. As shown in supplementary Fig. 3.12a, the respiratory rate of the mouse under systemic hypoxia decreased from 91±19 breaths/min to 22±4 breaths/min when the isoflurane concentration was increased from 0.5 MAC to 1.5 MAC. Blood-gas analysis revealed that the respiratory depression impaired oxygen supply and reduced P_aO_2 from 74±17 mmHg to 44±7 mmHg (supplementary Fig. 3.12b), which echoed the decrease in s_aO_2 observed by our PAM. The low respiratory rate also compromised CO_2 excretion, which consequently decreased the blood pH (supplementary Figs. 3.12c and 3.12d). The average s_vO_2 followed the same trend as s_aO_2, increasing to a peak at 66±4% (0.5 MAC) and then regressing to 37±6% (1.5 MAC). The sharp regression in s_vO_2 exceeded that in s_aO_2, which led to a significant increase in $rOEF$ from 50±3% (0.5 MAC) to 73±15% (1.5 MAC) as shown in Fig. 3.10b.

Similar to the biphasic response in sO_2, both the blood flow speed and vessel diameter experienced moderate increases under light anesthesia and then gradually regressed back to the baselines with increased anesthetic depths. As a consequence of the combined effects on flow speed and vessel diameter, $rCBF_{total}$ showed a statistically significant drop from 141±14% (0.5 MAC) to 105±23% (1.5 MAC), which echoed our observation in the normoxic brain and was likely due to the anesthetic depression of myocardial contractility.

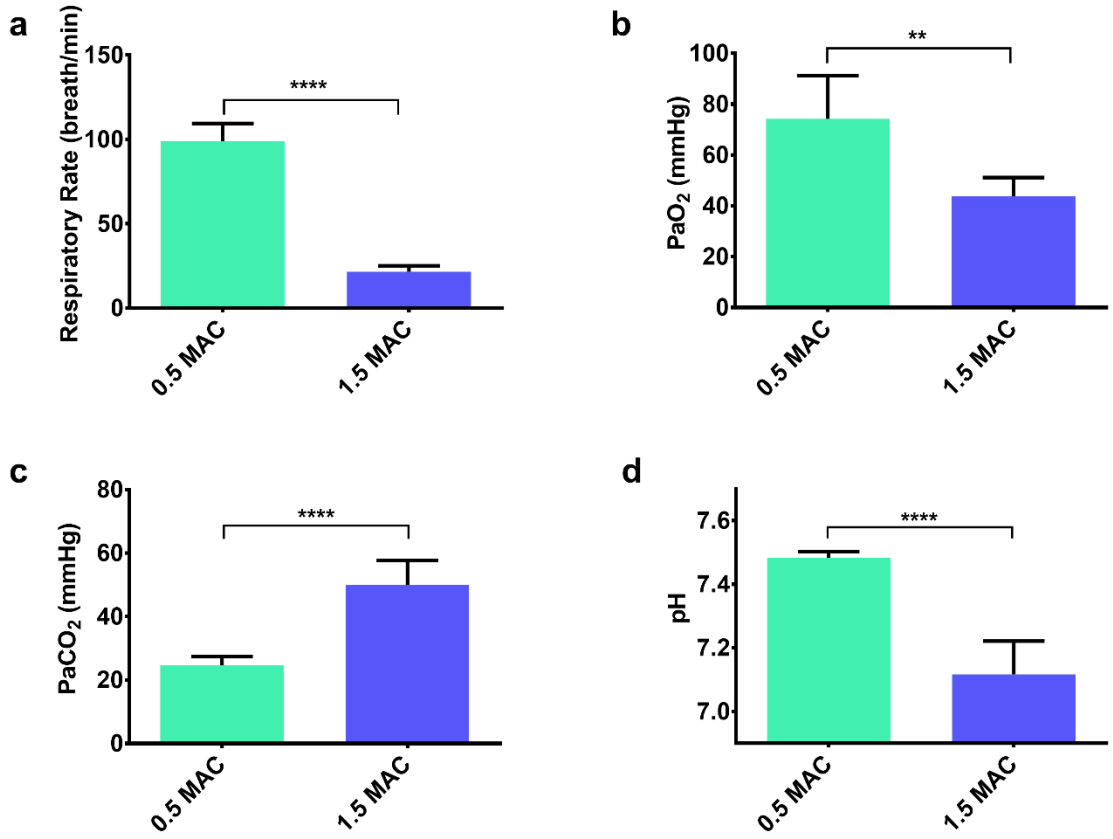

Fig. 3.12 Statistical comparison (N=6) of (a) respiratory rate, (b) PaO_2, (c) $PaCO_2$, and (d) blood pH in the hypoxic mouse brain under light (0.5-MAC isoflurane) and deep (1.5 MAC) anesthesia. **, $p<0.01$; ****, $p<0.0001$. Data are presented as mean ± SD.

Interestingly, the CBF-OEF coupling seemed to remain effective in the hypoxic brain. As shown in Fig. 3.10b, the incremental exposure to isoflurane resulted in gradually elevated $rOEF$ and reduced $rCBF_{total}$, whose product was roughly a constant across different levels of anesthesia (70±6%, 68±14%, and 70±13% for light, medium, and deep anesthesia, respectively). Taking into consideration of the respiratory depression-induced decrease in s_aO_2, however, $rCMRO_2$ (normalized to the baseline measured in the hypoxic brain under wakefulness) showed an isoflurane dose-dependent decline from 83±7% (0.5 MAC) through 67±10% (1.0 MAC) to 53±10% (1.5 MAC). The anesthesia-induced reduction of $CMRO_2$ from the awake baseline suggested a potential mechanism underlying the anesthetic neuroprotection against hypoxia- or ischemia-induced brain injury.

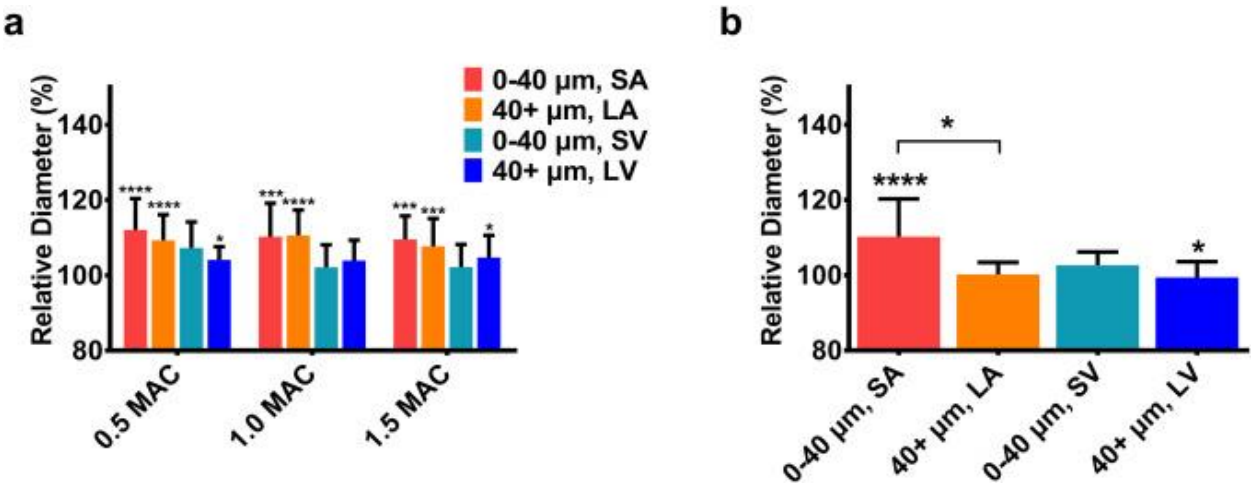

Figure 3.13 (a) Cerebral vasodilation in response to different concentrations of isoflurane (0.5, 1.0, and 1.5 MAC) under systemic hypoxia. Statistical comparison (41 feeding arteries and 26 draining veins in 5 mice) of the vessel diameters measured under anesthesia with their corresponding baseline values measured under wakefulness shows significant arterial dilation but only moderate venous dilation

across all three different anesthetic depths (significance levels, if any, are marked on the top of the columns). Moreover, statistical comparison between different groups of vessels under the same concentration of isoflurane shows no diameter-dependent dilation in either arteries or veins. Vasodilation shows no statistically significant dependence on isoflurane concentration under hypoxia. (b) Statistical comparison of the vessel diameters measured in the awake mouse brain under hypoxia with their baselines measured under normoxia shows statistically significant vasodilation in small arteries and veins (significance levels, if any, are marked on the top of the columns). Moreover, statistical comparison reveals a strong diameter-dependent dilation in the arteries but not veins (significance levels, if any, are marked between the two compared columns). *, $p<0.05$; ***, $p<0.001$; ****, $p<0.0001$. Data are presented as mean ± SD.

In striking contrast to the observation in the normoxic mouse brain, the isoflurane-induced dilation of small arteries (<40 μm in diameter) was much weaker under hypoxia and showed no statistically significant difference from that of large arteries (Fig. 3.13a). The reason was likely that these small arteries had been partially dilated under hypoxia (110±10%), prior to the isoflurane exposure (Fig. 3.13b). Besides vasodilation, hypoxia also showed profound impacts on other hemodynamic and metabolic parameters (supplementary Fig. 3.14), including decreased rs_aO_2 (79±7% of the baseline value measured under normoxia) and increased $rOEF$ (148±14%), $rCBF_{total}$ (141±40%), and $rCMRO_2$ (156±21%). These observations in the hypoxic mouse brain nicely echoed a recent human study using magnetic resonance imaging[72].

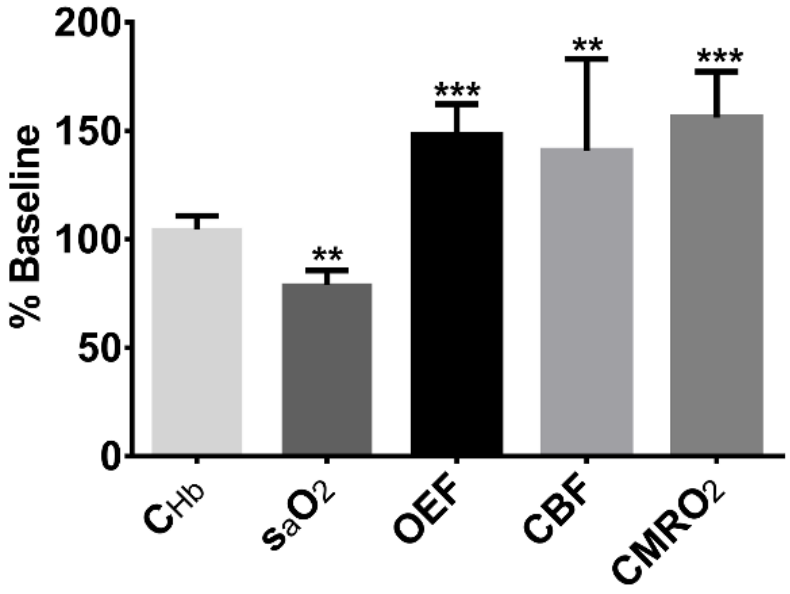

Fig. 3.14 Statistical quantification (N=5) of systemic hypoxia-induced relative changes in the arterial C_{Hb}, $s_a O_2$, OEF, CBF, and $CMRO_2$ from their normoxic baselines in the awake mouse brain. **, p<0.01; ***, p<0.001. Data are presented as mean ± SD.

3.5 Discussion and Conclusion

Anesthetic protection of the heart against ischemic injury has been established and widely applied in clinical practice [73]. There is enormous interest in translating this great success from the heart to the brain, but the outcomes of clinical trials on anesthetic neuroprotection are controversial and the underlying mechanism remains inconclusive [74]. Preclinical research in rodents, providing well controlled experimental conditions and relatively low heterogeneity among samples, is ideally suited for this mechanistic study. However, it has been a tremendous challenge to directly assess the anesthesia-induced changes in cerebral hemodynamics and oxygen metabolism from the "true" baseline under wakefulness, due to the lack of

an appropriate tool to image the awake mouse brain [75]. The head-restrained PAM fills this technology gap.

Quantitative PAM characterization of cerebral hemodynamics and oxygen metabolism enables direct, reproducible, and comprehensive assessment of the brain responses to anesthesia, advancing our current understanding based on the cerebral flow-metabolism coupling [76]. It has been shown that CBF and $CMRO_2$ are tightly and dynamically coupled in the awake normal brain [77]. Interestingly, volatile anesthetics elevate CBF via vasodilation and reduce $CMRO_2$ by suppressing brain activities, leading to the "uncoupling" of CBF and $CMRO_2$ or so-called "luxury" perfusion [78]. By simultaneous quantification of the evolutions of CBF, OEF, and $CMRO_2$ from wakefulness to anesthesia, our head-restrained PAM reveals that the flow-metabolism uncoupling is mediated via a marked decrease in OEF (Fig. 3g). Follow-up studies in the normoxic mouse brain under different depths of anesthesia further reveals that, instead of the flow-metabolism coupling, a tight inverse coupling exists between CBF and OEF, which dynamically maintains $CMRO_2$ at a statistically constant level (about half of that under wakefulness) across different anesthetic states. The anesthesia-induced reduction in the oxygen demand may delay the hypoxia- or ischemia-induced brain injury, thereby holding the potential to expand the therapeutic window for other primary interventions to be effective. Along this direction, our study shows that the anesthesia-induced $CMRO_2$ reduction remains effective in the hypoxic brain and that light anesthesia can partially retrieve the hypoxia-impaired s_aO_2. However, increasing the depth of anesthesia without mechanical ventilation eventually results in respiratory depression, which suppresses the oxygen supply to the hypoxic brain and significantly reduces s_aO_2. As a consequence, the CBF-OEF coupling is no longer able to maintain a constant metabolic level. The dose-dependent effects of isoflurane on OEF, CBF, and

$CMRO_2$ provide a possible explanation for the lack of consistency in previous experimental and clinical studies [75].

Although the present study has demonstrated that volatile anesthetics can alleviate the metabolic crisis during hypoxia, the neuroprotective effect needs to be further examined in the diseased brain. Furthering this mechanistic study in mouse models of ischemic stroke will allow us to interrogate whether volatile anesthetics can attenuate cerebral infarction and improve neurological functions by reducing cerebral oxygen demand during ischemia.

On a different but related note, the profound effects of anesthesia on cerebral hemodynamics and metabolism revealed by our study suggest volatile anesthetics as potential confounding factors in understanding neurovascular and neurometabolic coupling—the foundation of all hemodynamic-based neuroimaging technologies. Moreover, different anesthetics may have different influence on the quantitative evaluation of the coupling [76,79]. Extending the isoflurane study to other volatile and intravenous anesthetics will help resolve the discrepancy between existing studies using different anesthetic settings. Carrying out neurovascular coupling studies in the awake mouse brain using the head-restrained PAM may lead to new observations that have been masked by anesthesia and allow more reliable evaluation of the effects of neuroactive drugs and interventions on cerebral hemodynamics and metabolism at the microscopic level.

There is plenty of space to improve our technology. One limitation of our current system is the relative slow speed, requiring ~15 minutes to scan an area of 2.5×2.5 mm^2. This limitation prevents it from imaging rapid cerebral hemodynamic responses to neurostimulation and disease onsets (e.g., epileptic seizures). Integrating the head-restraint setting and our recently reported high-speed multi-

parametric PAM [80] may provide a potential solution. Another limitation lies in the quantification of $CMRO_2$. The current $CMRO_2$ was quantified with the help of the product of CBF and OEF, while OEF was calculated by average sO_2 values of the feeding arteries and draining veins within the region of interest. Since vessels with higher flow typically exhibit higher SO_2 and the sO_2 is usually heterogeneous, this current $CMRO_2$ quantification method using average sO_2 may have problems of overestimation. One alternative solution to more precisely compute $CMRO_2$ will be calculating the product of C_{Hb}, sO_2 and CBF for each individual feeding artery and draining vein to get the total oxygen inflow and outflow. By subtracting the total oxygen inflow and outflow, the $CMRO_2$ can be estimated. However, there is a practical challenge in implementing this approach. To estimate $CMRO_2$ by subtracting the total oxygen outflow of a cortical region of interest (ROI) from the total inflow, it requires that the ROI has a perfectly closed circulation—the arterial flux is identical to the venous flux. Otherwise, the mismatch/unbalance between the arterial and venous fluxes may cause considerable calculation errors.

We have developed first-of-a-kind head-restrained PAM for time-lapse and quantitative imaging of hemodynamics and oxygen metabolism in the awake mouse brain. Side-by-side comparison of the awake and anesthetized brain using this enabling technology revealed strong and multifaceted cerebral responses to isoflurane—including the diameter-dependent arterial dilation, elevated CBF, reduced OEF, and declined $CMRO_2$. Further comparison of these responses to different depths of anesthesia uncovered intriguing dose-dependent effects of isoflurane on OEF, CBF, and $CMRO_2$ under both systemic normoxia and hypoxia. Our results suggest that the widely reported but poorly understood anesthetic neuroprotection may be mediated through anesthesia-induced suppression of the cerebral oxygen demand and that the protection may be dose-dependent. The head-

restrained PAM bridges the critical gap between functional and molecular microscopy of the awake mouse brain. Future integration of the two microscopy techniques with highly complementary contrasts into one head-restrained setting will open up exciting new opportunities in basic and translational neuroscience.

Chapter IV. Comprehensive Characterization of the Cerebral Vasculature

4.1 Background and Motivation

4.1.1 Cerebral Small-vessel Disease

Supporting the brain with more than 20% of the oxygen consumed by the whole body at the resting state[81], the cerebral vasculature is essential for brain function and survival. Indeed, subtle changes in the autoregulation of the diameter, blood oxygenation or flow of the ubiquitously presented microvessels can disrupt the delicate balance between the oxygen demand and supply, thereby impairing the integrity of the brain[82]. Cerebral small vessel disease (CSVD), resulting from pathologies in the cerebral microvasculature, has been associated with substantial cognitive[83], psychiatric[84] and physical disabilities[85] in the elderly population. Moreover, it is involved in 45% and 20% of all cases of dementia and stroke, respectively[86–88].

Although attracting increasing attention, the CSVD remains largely understudied. A major challenge to investigating the CSVD is the limited accessibility of these small vessels in the live brain[89]. Recent advances in computed tomography (CT), magnetic resonance imaging (MRI), and positron emission tomography (PET) have facilitated diagnosis and treatment monitoring of cerebrovascular diseases in the clinic[90]. However, it remains challenging for MRI and PET to visualize microvessels in the brain, due to the insufficient spatial resolution[91]. Although capable of imaging microvessels less than 40 μm, CT cannot access some of the important functional parameters, including blood oxygenation[92]. Given the limitations of the clinical

technologies, there is an urgent need for new imaging tools that allow high-resolution comprehensive characterization of the cerebral microvasculature in animals. A recent breakthrough in medical ultrasound has enabled microvascular imaging in the rodent brain[93]. However, similar to CT, it cannot measure blood oxygenation and requires injection of angiographic agents, which might cause physiological perturbations and discourages longitudinal monitoring. Advances in two-photon microscopy (TPM), the technology of choice for intravital imaging of the rodent brain, has enabled visualization of the cerebral microvasculature at a much finer spatial scale. However, injection of angiographic agents is also required[2,94]. Even with the aid of exogenous angiographic agents, comprehensive evaluation of disease-induced alterations in the cerebral microvasculature remains unachievable.

4.1.2 Obesity and Cerebral Small Vessel Disease

Associated with blood pressure increase, dyslipidemia, glucose abnormality, and/or insulin resistance[95], obesity is increasingly being considered as an important risk factor for CSVD and ischemic stroke[96,97]. Emerged as a major global health problem, 39.6% of adults in the United States are obese, leading to a cost of more than $150 billion annually[98,99]. Associated with increased arterial blood pressure, dyslipidemia, glucose abnormalities and/or insulin resistance[95,100], obesity is increasingly being recognized as an important risk factor for multiple brain dysfunctions and diseases, such as hypertension, diabetes mellitus, and vascular diseases[97]. Emerging evidences shows that obesity and overweight are closely linked to the high incidence of the heart disease and stroke[101–104], two of the most prevalent severe diseases in United States[105].

However, the relationship between obesity and the cerebrovascular (and cardiovascular) diseases remains inconclusive and controversial[106]. Recent studies have shown that obesity is not always associated with poor outcomes in patients[107] and, paradoxically, may be associated with lower morbidity and mortality[108–111]. Although obesity has been proved to be a major risk factor for many vascular diseases and may increase the incidence of stroke and heart diseases, recent studies show that obesity may not be associated with poor outcome in all patient populations[107]. The "obesity paradox" has been reported in different studies, which shows a paradoxical decrease in morbidity and mortality with increasing body mass index (BMI) in cardiovascular diseases[108–111]. Currently, the obesity paradox is very controversial since various studies showed conflicting results[112,113]. It still lacks convincing explanations, partly due to the unclear relationship between obesity and the vascular changes, which are directly related to cardiovascular and cerebrovascular diseases. This ongoing controversy underscores the critical need for improved understanding of obesity-induced changes in the vasculature, especially at the microscopic level. Here we report the application of an advanced head-restraint PAM system for the study of obesity induced cerebral vascular changes, which may provide valuable information for understanding the relationship between obesity-induced cerebrovascular remodeling and cerebrovascular diseases, especially CSVD.

4.1.3 Mouse Model of High-fat Diet-induced Obesity

Male CD-1 mice were acquired at the age of 10 weeks (Charles River Laboratory) and randomly divided into two groups on either the normal diet or high-fat diet (D12451, Research Diets). Consisting of 45% fat calories, 35% carbohydrate calories, and 20% protein calories, the high-fat diet had a food energy of 4.73 kcal/g. The two groups of mice were fed on different diets for 12 months before the present

study. To confirm the validity and effect of this obesity model, the body weight, random bold glucose level, cholesterol, triglycerides as well as the high-density and low-density lipoproteins (HDL and LDL, respectively) were measured.

Specifically, right after the group assignment, the mouse body weight was measured to be 32.9±1.1 g for the control group and 33.3±0.9 g for the high-fat diet (i.e., obese) group, showing no bias. After 12 months of feeding, the mice in the obese group became significantly overweight (70.8±7.2 g) compared to those in the control group (61.1±2.5 g). Although obesity is often accompanied by hyperglycemia, the blood glucose levels in the control group (152.2±15.1) and the high-fat diet group (147.0±21.9) did not show significant difference in this study, so did the levels of triglycerides and HDL and the ratios of LDL/HDL and cholesterol/HDL. Nevertheless, the cholesterol and LDL levels were significantly higher in the obese group (Fig. 4.1).

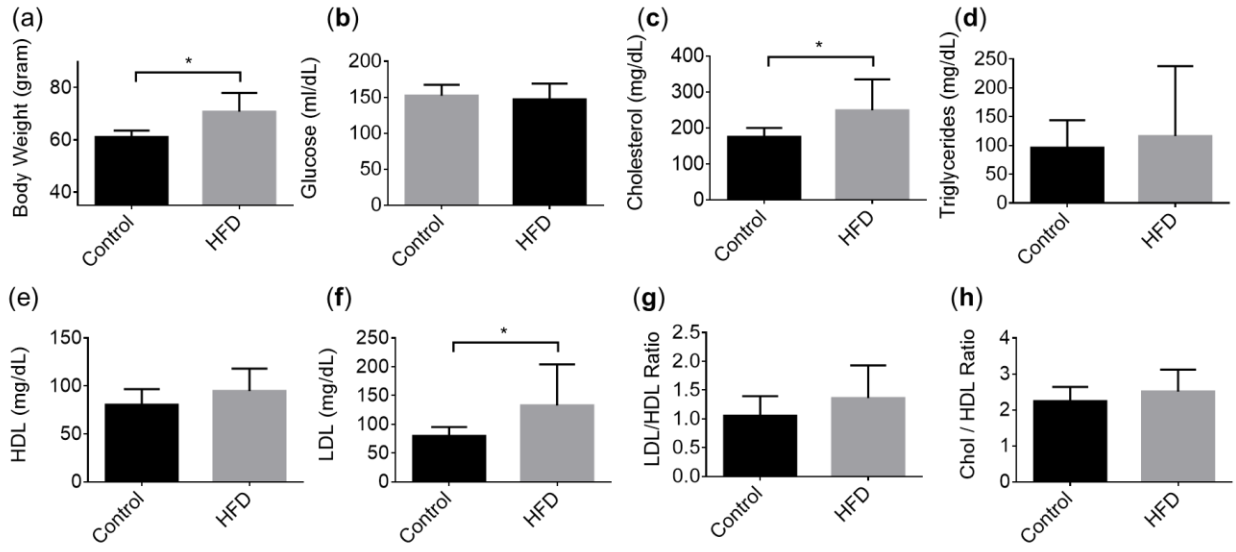

Fig. 4.1 Physiological data of the control mice (n=8) and high-fat diet (n=8) mice. (a) body weight, (b) blood glucose level, (c) cholesterol, (d) triglycerides, (e) HDL, (f) LDL, (g) LDL/HDL, and (h) Cholesterol/ HDL. Values in graphs are the means ± SD; *, $p<0.05$.

4.2 PAM Characterization of the Cerebral Vasculature

4.2.1 Vessel Density and Tortuosity

To quantify the vascular density, an amplitude threshold (i.e., 4 times of the standard deviation of the background) was applied to isolate the vascular signal. Then, the pixel number occupied by blood vessels was quantified, from which the vascular density can be estimated as the ratio of the vessel pixel number to the total pixel number.

To quantify the vascular tortuosity, the skeleton of the vessel segment was extracted. Then, the linear distance (S) between the start point and the end point of the skeleton was calculated based on their coordinates, and the actual length (l) of the skeleton was estimated by counting the pixel number. Thus, the vascular tortuosity can be calculated as

$$Tortuosity = \frac{l}{S}. \quad \text{(eq. 4.1)}$$

4.2.2 Vessel Shear Stress and Resistance

The thickness and skeleton of individual microvessels extracted by the segmentation-based analysis granted us the access to important mechanical properties of the cerebral microvasculature. Specifically, the vascular resistance was calculated using Poiseuille's law as

$$R = \frac{8\eta L}{\pi r^4}, \quad \text{(eq. 4.2)}$$

where η is the blood viscosity (assumed to be 4.88 cP)[114], L is the vessel length, and r is the vessel radius. Moreover, with the measured volumetric blood flow and vessel radius, the wall shear stress was calculated as[115]

$$\tau = 4 \times \eta \times \frac{Flow_v}{\pi \times r^3}. \quad \text{(eq. 4.3)}$$

4.2.3 Measurement of BBB Permeability Dynamics in the Awake Mouse

Evans blue dye was used to measure the permeability of the blood brain barrier (BBB). To avoid general anesthesia during the PAM experiment, a 28-gauge needle connecting to a soft micro-tube was inserted into the tail vein of the mouse and fixed in position right before the imaging experiments, allowing the awake mouse to freely move its tail. A light-weight wood stick (~0.25g) was attached to the tail to avoid dislocation of the needle. After the baseline imaging, 2% (w/v) Evans blue dye was injected at the dose of 4 ml/kg animal's body weight.

Dynamic quantification of the BBB permeability was achieved by counting the total number of pixels occupied by the extravascular dye in individual time-lapse images. Following the method described in the section on vascular density measurement, the vessel pixel number was quantified in the baseline image acquired prior to Evans blue injection. Thus, the increase in non-background pixels in the post-injection images was due to the dye extravasation. With this, the experimentally measured amount of Evans blue diffused out of the cerebral vasculature was fitted to an exponential recovery model

$$A(t) = P \times [1 - exp(-kt)], \quad (8)$$

where P is the amount of extravasated dye at the steady state and k is the diffusion coefficient. To extract the dynamic diffusion rate, the first-order derivative of $V(t)$ was taken as

$$\frac{\partial V(t)}{\partial t} = P \times k \times \exp(-kt). \quad (9)$$

4.2.4 PAM of CVR via Acetazolamide in the Awake Mouse

Traditionally, the cerebrovascular reactivity (CVR) is the ratio of the volumetric blood flow after vasodilatory stimulation to the baseline value. Given the unique capability of the present PAM platform in comprehensive characterization of the cerebral vasculature, we have expanded the CVR to other structural, functional and metabolic parameters, including diameter, sO_2, flow speed, OEF and $CMRO_2$. In this study, acetazolamide (ACZ) was used as a vasodilatory stimulus. Before the stimulation, multi-parametric PAM was performed to acquire the baseline values. Then, 50 mg/kg ACZ was intravenously injected into the awake mouse through the implanted needle. The CVR was then comprehensively characterized by comparing the individual structural, functional and metabolic parameters against their baseline values.

4.3 Obesity-induced Cerebrovascular Alterations

4.3.1 Obesity-induced Alterations in Cerebrovascular Structure and Function

To comprehensively evaluate obesity-induced alterations in cerebrovascular structure and function without the influence of general anesthesia, side-by-side comparisons of the vascular density, tortuosity, sO_2, blood flow speed, OEF, resistance and wall shear stress between the control and obese groups were performed in the awake brain. Further, vessel type-specific analysis was carried out for all parameters quantified at the single-vessel level, by dividing these vessels into four categories—small arteries (<40 μm), small veins (<40 μm), big arties (≥40 μm), and big veins (≥40 μm).

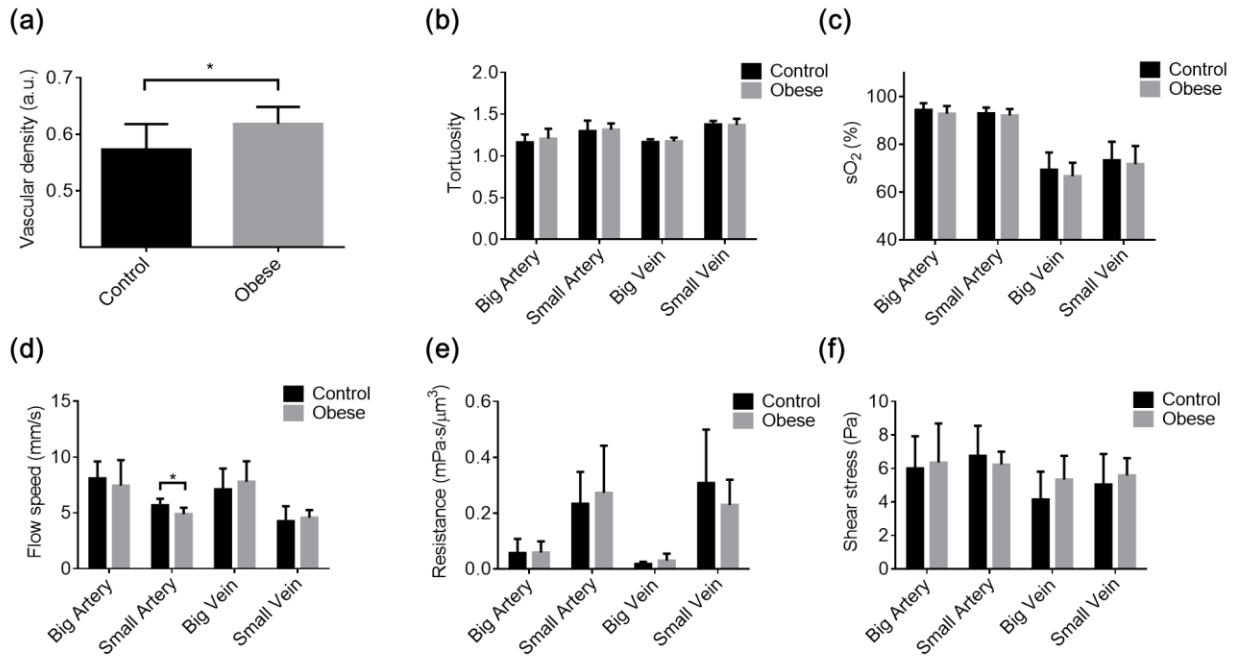

Fig. 4.2 PAM measurements of the cerebrovascular remodeling in (a) vascular density, (b) average vessel tortuosity, (c) average sO2, (d) average blood flow speed, (e)average vessel wall resistance, and (f) average vessel shear stress in control (n=6) and obese (n=8) mice. Values in graphs are the means ± SD; *, $p<0.05$.

The vascular density was found to be significantly higher (by 7.9%) in the brains of obese mice (Fig. 4.2a). On average, there was no statistically significant difference in the vascular tortuosity between the control and obese groups (Fig. 4.2b); however, individual arteries with pronounced tortuosity and relatively high flow speed were observed in the obese mice but not the control mice (yellow arrows in Fig. 4.3).

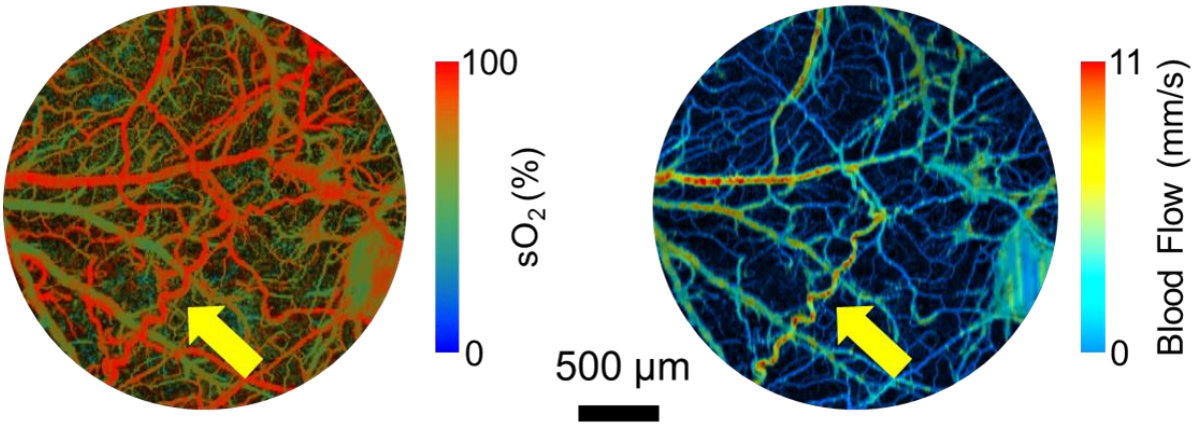

Fig. 4.3 The vessel pointed by yellow arrows are representative tortuous vessel in obese mouse brain.

Although no significant difference was found in the vessel type-specific sO_2 between the two groups (Fig. 4.2c), the average venous sO_2 in the obese mice was lower than that in the control mice (by 3.9% and 2.1% in the big and small veins, respectively), resulting in a significantly higher OEF (Fig. 4.4d).

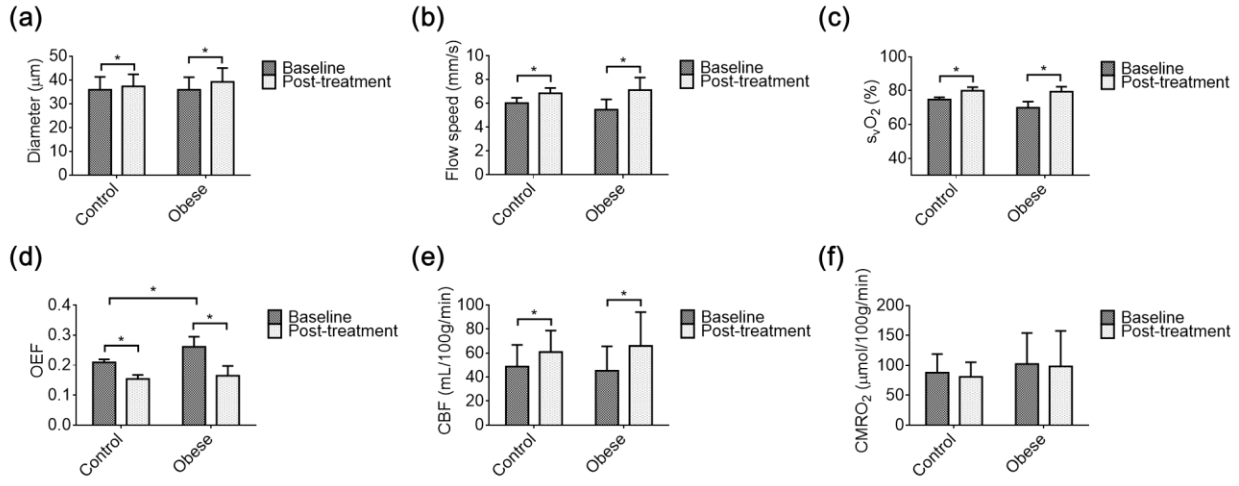

Fig. 4.4 The cerebrovascular and hemodynamic responses to acetazolamide. (a) vessel diameter, (b) average blood flow speed, (c) average venous sO_2, (d) regional

OEF, (e) regional CBF, and (f) regional $CMRO_2$. Values in graphs are the means ± SD； *, $p<0.05$.

Interestingly, the higher tissue oxygen extraction was partially counterbalanced by the lower arterial flow speed (Fig. 4.2d), particularly in small arteries (4.9±0.6 mm/s for the obese group vs. 5.7±0.6 mm/s for the control group). As a result, the obese mice showed only slightly higher but statistically undifferentiated regional $CMRO_2$ from the control mice (Fig. 4.4f). In contrast to the obesity-induced impairment in the arterial flow, no significant changes were observed in the resistance (Fig. 4.2e), wall shear stress (Fig. 4.2f), and C_{Hb} (Fig. 4.5).

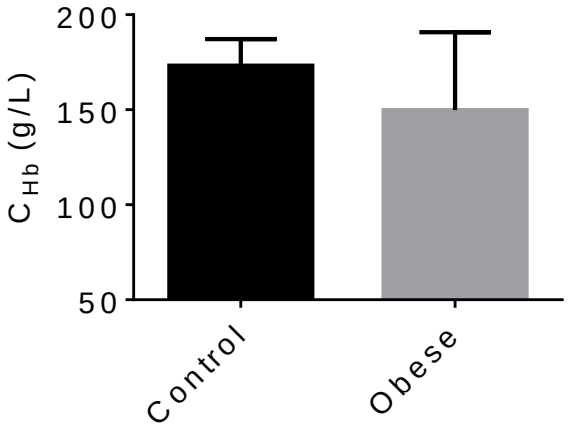

Fig. 4.5 PAM measurements of the CHb in control (n=6) and obese (n=8) mice. Values in graphs are the means ± SD； *, $p<0.05$.

4.3.2 Obesity-induced Increase in Cerebrovascular Permeability

As an important barrier between the brain tissue and the cerebral blood circulation, the BBB has limited permeability, protecting the brain against toxic molecules and rapid changes in ionic or metabolic conditions[116]. The PAM-based Evan blue assay was used to study the influence of obesity on the BBB integrity. Capitalizing on the

strong optical absorption of Evans blue, the dye extravasation was dynamically imaged and quantified to evaluate the BBB permeability.

Time-lapse monitoring of the same ROI in the awake mouse brain for 155 minutes following the dye injection showed visually striking difference between the control (Fig. 4.6a) and obese mice (Fig. 4.6b). Further, quantitative analysis by fitting the experimentally measured Evans blue extravasation against the exponential recovery model showed that, 35 minutes after injection, the amount of dye diffused out of the cerebral vasculature in the obese mice was significantly higher than that in the control mice, ultimately leading to a 29.8% higher extravasation at the steady state (Fig. 4.6c). Further, by taking the first-order derivative of the exponential-fitted diffusion curve, the diffusion rate can also be quantified (Fig. 4.6d). Interestingly, the dye extravasation in the control mice started at a rate comparable to that in the obese mice (0.10 vs. 0.09). However, the diffusion rate in the obese mice surpassed that in the control mice 6 minutes after injection and sustained at a higher level, lasting for 64 minutes before dropping to less than 10% of the initial rate compared to the 45 minutes in the control mice.

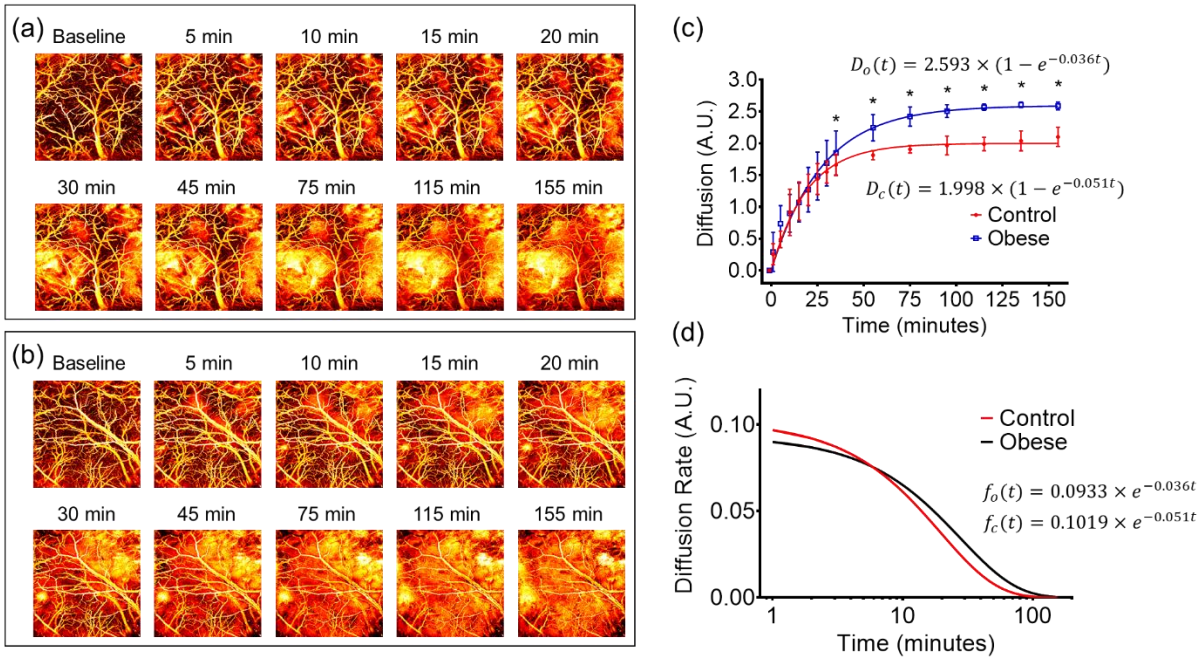

Fig. 4.6 PAM monitor of Evans blue diffusion dynamics in (a) control and (b) obese mouse before and after the i.v. injection, up to 155 minutes. (c) Statistical analysis and fitting curve of the diffusion dynamic in the control (n=5) and obese (n=5) mice. (d) The diffusion rate of Evans blue in control and obese mice. Values in graphs are the means ± SD; *, $p<0.05$.

4.3.3 Obesity-induced Increase in Cerebrovascular Reactivity

Indicating the vasodilatory capability and perfusion reserve in the brain, the CVR is a valuable addition to the baseline CBF for evaluating cerebrovascular dysfunction[117,118]. The multifaceted CVR to acetazolamide-based vasodilatory stimulation was measured by PAM in the control (Fig. 4.7a) and obese (Fig. 4.7b) mouse brains under wakefulness, circumventing the influence of general anesthesia.

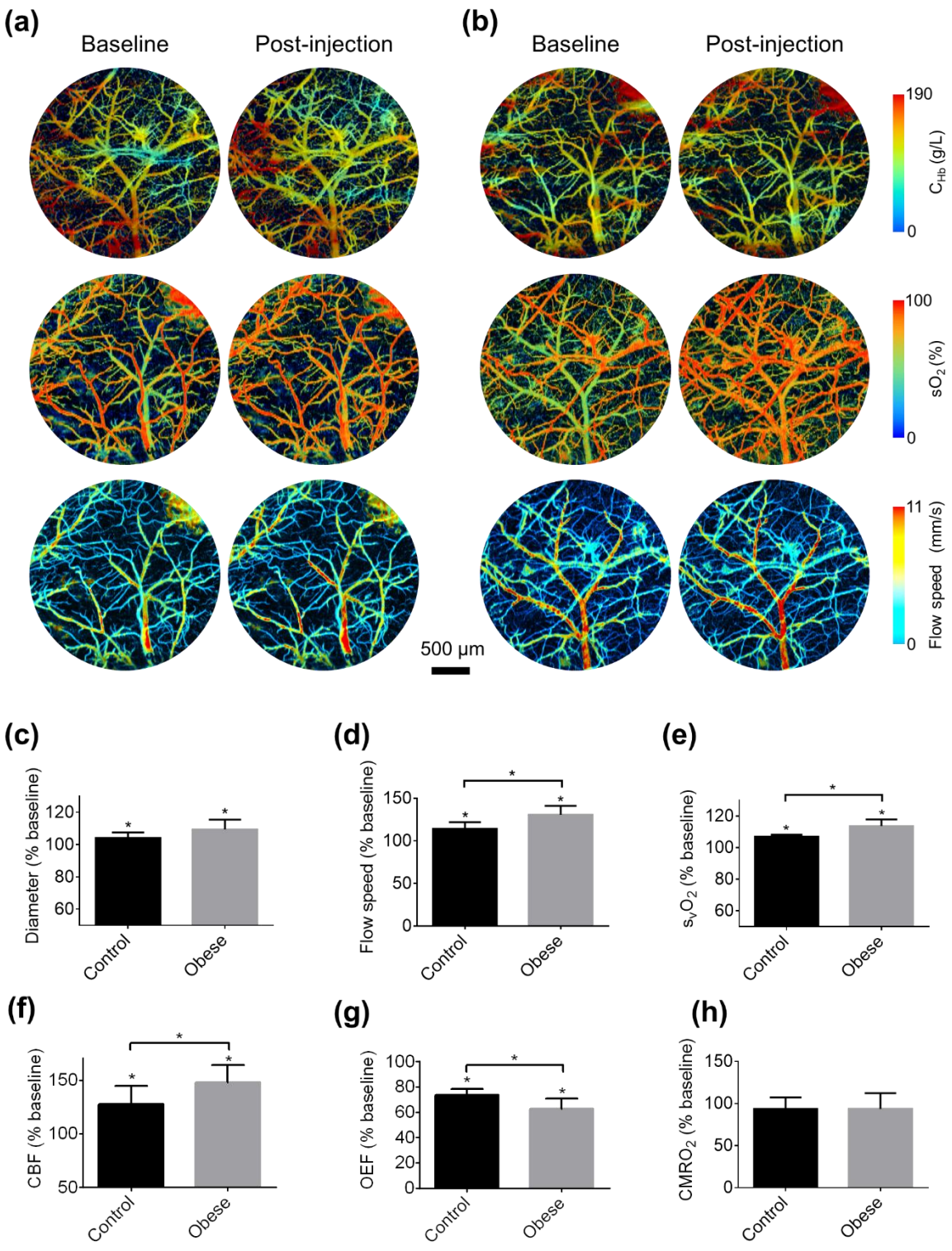

Fig. 4.7 Blood oxygenation and flow acquired before and after the injection of acetazolamide in (a) a control mouse and (b) an obese mouse. (c) average venous

sO_2, (d) vessel diameter, (e) average blood flow speed, (f) regional OEF, (g) regional CBF, and (h) regional $CMRO_2$ in response to ACZ injection in control (n=6) and obese (n=8) mice. Values in graphs are the means ± SD； *, $p<0.05$.

After ACZ injection, significant vasodilation was observed in both animal groups (Fig. 4.7c). Interestingly, the average relative vasodilation in the obese group (9.4%) was more pronounced than that in the control group (4.1%), although the difference was not yet statistically significant (p=0.08). Along with the vasodilation, the ACZ stimulation resulted in increased blood flow speed (Fig. 4.7d) and venous sO_2 (Fig. 4.7e) in both groups. Again, the increases in flow speed (30.6%) and venous sO_2 (13.6%) in the obese mice were significantly higher than those (14.1% for flow speed and 6.9% for venous sO_2) in the control mice, respectively. As expected, the arterial sO_2 was not affected by ACZ (Fig. 4.8).

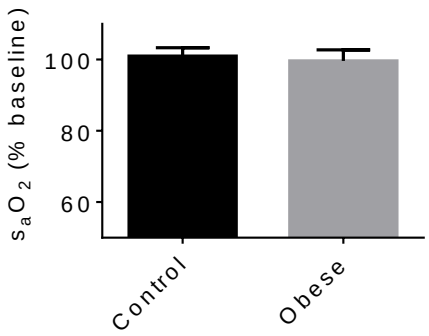

Fig. 4.8 Average arterial sO_2 in response to ACZ injection in control (n=6) and obese (n=8) mice. Values in graphs are the means ± SD； *, $p<0.05$.

The more pronounced vasodilation and flow speed upregulation in the obese mice led to a more significant increase in the regional CBF (47.8%) compared to that (27.4%) in the control mice (Fig. 4.7f), while the more significant venous sO_2 increase in the obese mice resulted in a larger decrease in the regional OEF (26.5% and 37.2% for the control and obese groups, respectively; Fig. 4.7g). The inverse

coupling of CBF and OEF managed to keep the regional $CMRO_2$ unaffected by the vasodilatory challenge in both groups (Fig. 4.7h), in good agreement with previous MRI and PET observations[119,120]. Again, no noticeable changes in the C_{Hb} were observed in both groups (Fig. 4.9).

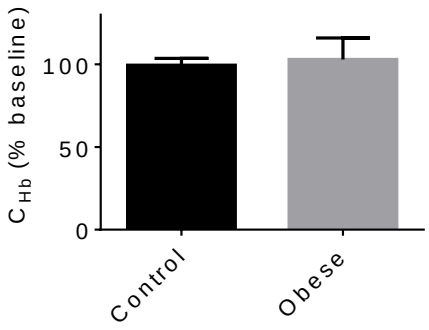

Fig. 4.9 Average C_{Hb} in response to ACZ injection in control (n=6) and obese (n=8) mice. Values in graphs are the means ± SD； *, $p<0.05$.

With the aid of vessel segmentation, the multifaceted CVR observed by PAM was further dissected to examine whether the obesity-induced cerebrovascular alterations were vessel type-specific or not. Interestingly, although no significant difference was observed in the average vasodilation between the two animal groups (Fig. 4.7c), the small arteries and small veins in the obese mice did show much greater vasodilation (Fig. 4.10a). Similarly, the ACZ-induced upregulation in the flow speed was mainly attributed to the small arteries, along with the big and small veins (Fig. 4.10b). Given that the volumetric flow is co-determined by the diameter and flow speed, not surprisingly, the vessel type-dependent response of volumetric flow to ACZ was consistent with those of the other two parameters (Fig. 4.10c).

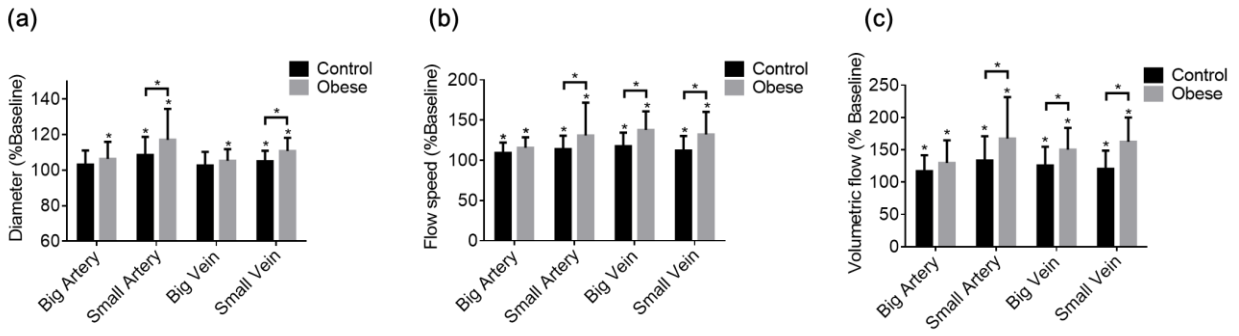

Fig. 4.10 Statistical comparison of the (a) vasodilation, (b) blood flow speed, and (c) CVR of different vessel types in response to acetazolamide. Sample size: 13 big arteries, 45 small arteries, 31 big veins, and 22 small veins in the control group and 17 big arteries, 52 small arteries, 35 big veins, and 28 small veins in the obese group. Values in graphs are the means ± SD; *, $p<0.05$.

4.4 Discussion and Conclusions

Comprehensive characterization of disease-induced microvascular changes in the brain remains as an unmet challenge, but is yet necessary for investigating the roles of small-vessel pathology in a wide range of brain disorders. To fill this technology gap, we have developed a new PAM-based imaging and analysis platform. Capitalizing on the optical absorption of blood hemoglobin, this platform is capable of imaging vascular anatomy, blood perfusion, oxygenation and flow in the awake mouse brain in a label-free manner. Exploiting the optical absorption of Evan blue, an exogenous dye long established for examining vascular permeability, it enables dynamic assessment of the BBB integrity. With the aid of vasodilatory stimulation, this technique provides a unique access to the multifaceted CVR. Furthermore, the vessel segmentation analysis allows extracting the PAM-measured vascular parameters at the single-vessel level, from which the vascular density, tortuosity, wall shear stress, resistance and associated tissue oxygen extraction fraction and

metabolism can be quantified and the vessel type-specific alterations can be identified.

We demonstrated the utility of this enabling technique by studying obesity-induced changes in the cerebral microvasculature. Reaching global epidemic proportions in both adults and children over the past few decades, obesity has been broadly associated with cerebrovascular and cardiovascular comorbidities, including but not limited to ischemic stroke, coronary heart disease, and heart failure[111]. However, the effect of obesity on the vasculature and thus the prognosis of these devastating diseases remains incompletely understood[109,121], particularly microvascular complication in the brain that has long been linked to obesity but is much understudied due to the poor accessibility[122].

Relying on the endogenous contrast from hemoglobin, the PAM-based platform has distinct advantages in cerebrovascular imaging over TPM, which requires angiographic and oxygen-sensitive agents that might perturb the microcirculation and severely limit the imaging speed due to the long phosphorescence lifetime[2]. Using this new platform, we were able to comprehensively quantify obesity-induced changes in cerebrovascular structure, mechanical property, hemodynamics, and associated tissue oxygen extraction and metabolism. Specifically, increased vascular density, reduced blood flow in small arteries, and elevated tissue oxygen extraction were observed in the obese mouse brain. Moreover, individual arteries with pronounced tortuosity were also observed. These *in vivo* results are in agreement with the previous observations of increased microvascular density and increased tortuosity of the middle cerebral artery (MCA) in the dissected obese mouse brain[123] and the observations of reduced MCA flow speed[124] and increased OEF[125] in obese patients. Interestingly, the obese but normoglycemic mice in our study did not show overt changes in average vascular tortuosity, resistance, wall shear stress, and blood

oxygenation at the microvascular level, in contrast to the higher resistance[124] and lower shear stress[126] observed in the individual trunk vessels (e.g., MCA or femoral vein) of obese and hyperglycemic patients.

Also, we extended the classic Evan blue assay from postmortem to the awake mouse brain for dynamic evaluation of the cerebrovascular permeability without the influence of general anesthesia[127]. Consistent with the previous studies[128], the PAM-based platform revealed a ~30% higher dye extravasation at the steady state in the obese mouse brain, indicating a compromised BBB integrity. Interestingly, the dynamic monitoring of dye extravasation enabled by our platform showed that the obesity-induced BBB disruption resulted in a prolonged diffusion period rather than an elevated diffusion rate. Enabling dynamic and time-lapse monitoring of molecule diffusion through the BBB, this assay will allow us to trace BBB dysfunction over the progression of cerebrovascular diseases (e.g., CSVD, stroke, traumatic brain injury, and cerebral amyloid angiopathy)[129–132] and might find useful applications in drug delivery and pharmacokinetics in the brain[133].

Taking advantage of the unique ability of our platform for comprehensive imaging of the cerebral vasculature, we also extended the assessment of CVR from conventional blood flow to multiple parameters—spanning from structure to hemodynamics to the associated oxygen metabolism. Similar to the BBB permeability, the CVR is known to be altered under anesthesia[134,135]. The ability of our platform for imaging the awake brain ensured unbiased measurements. Unlike the whole-brain CVR measured by MRI[136,137], our platform enabled CVR quantification in individual microvessels, from which vessel type-specific reactivity was revealed. Intriguingly, more pronounced multifaceted CVR in response to the ACZ-induced vasodilatory stimulation was observed in obese mice, including stronger vasodilation in small arteries and veins, greater flow upregulation in small

arteries and all veins, and more significant elevation in venous sO_2. The increased oxygen supply through the flow upregulation and the decreased oxygen extraction as indicated by the elevated venous sO_2 counterbalanced each other and managed to keep the $CMRO_2$ unaffected by the ACZ challenge. Our observation of increased CVR in the obese mice was somewhat counterintuitive and in contrast to previous studies[138], which showed that obesity led to impaired vasodilatory ability. It is worth noting that, unlike the obese but normoglycemic mice used in this study, obesity is often accompanied by hyperglycemia, which also has strong influence on vasodilation. Previous studies have shown that obesity affects the endothelial cell function but not the smooth muscle cell function, while diabetes affects both[139]. The selective effect of obesity may explain why the obese but nondiabetic mice did not show impaired vasodilation to the ACZ, which likely acts on the smooth muscle cell rather than the endothelial cell[140].

Given that nitric oxide is involved in ACZ-induced vasodilatory stimulation[141], we examined the eNOS level in the obese and control mouse brains (Fig. 4.11a). Our results showed that the phospho-eNOS in the obese mice was more than 3-fold higher than that in the control mice (Fig. 4.11b), while the total eNOS showed no difference between the two groups (Fig. 4.11c). The significantly increased activation of eNOS, which plays an important role in vasodilation and microvascular permeability[142], echoed the increased vasodilation and BBB permeability in the obese mice observed by our platform.

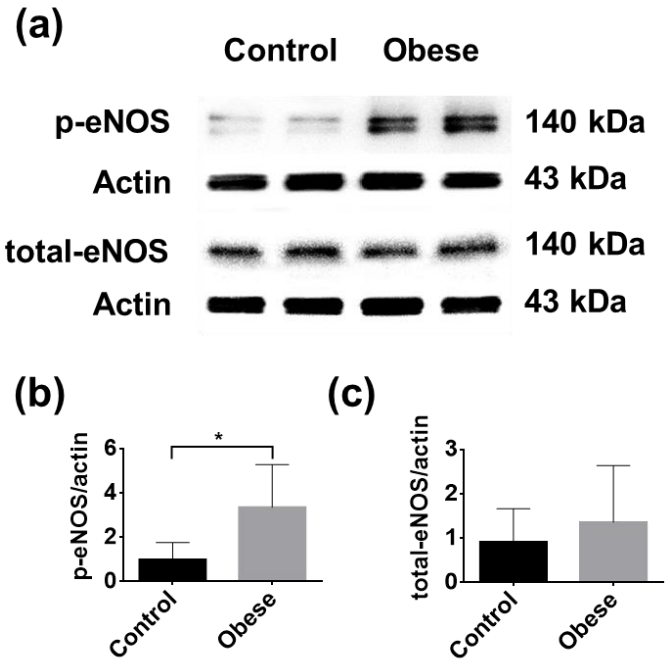

Fig. 4.11 (a) Representative western blotting images of phospho-eNOS and total eNOS. Statistical comparison of (b) phospho-eNOS and (c) total eNOS in control (n=8) and obese (n=8) mice. Values in graphs are the means ± SD; *, $p<0.05$.

The observed microvascular changes in the obese mouse brain, including increased vascular density, enhanced OEF, and increased CVR, might be neuroprotective against ischemic stroke[143–145]. In contrast, the obesity-induced impairment of the BBB integrity may lead to hemorrhagic transformation after ischemic stroke[146]. Indeed, recent studies have reported interesting observations that the diabetic but nonobese rat brain showed increased vascular density and permeability compared to the control brain, resulting in reduced infarct size but greater hemorrhagic transformation after ischemic stroke[147,148]. The two-sided effect suggests that the influence of obesity-induced vascular alterations on cerebrovascular and cardiovascular diseases is complex. Further studies with careful considerations of the multifaceted vascular responses to obesity are required to resolve the long-standing controversy on this topic.

In summary, we have developed a hardware-software integrated intravital imaging platform for comprehensive characterization of disease-induced changes in the cerebral microvasculature. Uniquely capable of quantifying alterations in the cerebrovascular structure, function and reactivity, as well as the associated tissue oxygen metabolism, this new technique opens a new window to investigate the mechanistic roles of obesity in cerebrovascular diseases. Transforming this technique to other vital organs (e.g., the heart and kidney) may further leverage its impact in cardiovascular research.

Chapter V. Comprehensive Characterization of Cerebrovascular Dysfunction in Blast Traumatic Brain Injury Using Photoacoustic Microscopy

5.1 Background and Motivation

As a major cause of disability and death, traumatic brain injury (TBI) poses a massive health and financial burden in the United States, affecting over 2 million people and costing more than $76 billion in medical expenses and lost productivity every year[149,150]. In particular, TBI due to explosive blast exposure is a leading casualty in the battlefield and a key contributor to combat-related mental health diseases[151]. Although increasing attention has been drawn recently, comprehensive research on the pathophysiology of TBI remains marginal. Mainly focusing on the injury-induced neuronal dysfunction, current research fails to translate effective therapies to the trauma clinic[152–154]. Emerging evidence suggests that the coexisting cerebrovascular dysfunction might be a potential therapeutic target and merits in-depth investigation[155–162].

Indeed, different forms of cerebrovascular dysfunction have been observed in TBI patients, including alteration in CBF[163,164], impairment of vascular autoregulation[165,166], hemorrhage[167,168], vasospasm[169–172], and disruption of the BBB[131,173–176]. Moreover, a rodent study shows that TBI can lead to a long-term impairment in the vasodilatory capability, accompanied by persistent deficits in the spatial memory[177]. These indications, although supporting a key role of vascular insult in TBI, were obtained in different clinical and experimental settings. It remains a challenge to integrate them into a complete picture.

It is impractical to form a holistic view of the influence of TBI on the cerebral vasculature in the clinical setting, due to the heterogeneity in patients[178]. Rodent models of TBI, which have well controlled disease conditions and relatively low heterogeneity, offer an ideal experimental setting to study the injury-induced cerebrovascular dysfunction[178,179]. Along this direction, a rat model has been developed to mimic the blast TBI (bTBI) that frequently happens in military conflicts. Using a high-pressure shock tube to simulate the blast effect[180–182], this model system well recapitulates the situation in blast-exposed military personnel—diagnosed with TBI while showing no external injuries[183,184]. Moreover, the rat model of bTBI permits high-resolution functional imaging of the brain. Capitalizing on the optical absorption of blood hemoglobin, our recently developed multi-parametric PAM enables label-free comprehensive characterization of the rodent cerebral vasculature at the microscopic level[25,33,185], including C_{Hb}, sO_2, , CBF, OEF, $CMRO_2$, and CVR, presenting an ideal tool to study bTBI-induced cerebrovascular dysfunction. Combining the rat model of bTBI and multi-parametric PAM, we investigated the anatomical, functional and metabolic dysfunction in the cerebral vasculature following bTBI. Also, with self-developed vessel segmentation algorithm[186], we characterized the differential responses of different vessel types to the blast injury.

5.2 Rat Model of blast TBI

In this study, 6–8 weeks old male Sprague Dawley rats (Charles River Laboratory) were randomly assigned to two different groups (control vs. bTBI). Prior to the experiments, the rats were housed in the vivarium under a 12 hour light/12 hour dark cycle with access to food and water. All animal procedures and experiments were approved by the Institutional Animal Care and Use Committee at the University of

Virginia. Four hours prior to PAM experiments, the animal was anesthetized with pentobarbital and put into the high-pressure shock tube (Fig. 5.1A) in the Aerospace Research Laboratory at the University of Virginia. The shock tube could generate blast waves with a static pressure of up to 30 psi (~208 kPa). In our bTBI setting, the shock wave rose to its peak pressure within 2 μs and quickly dropped to 20% of the peak pressure within 5 ms (Fig. 5.1B). During this procedure, the animal was closely monitored using a high-speed camera (10,000 fps) to confirm that it was in the right position and posture. The total time for animal handling and the blast procedure was less than 5 minutes. After that, the animal was wrapped with a heating pad and supplied with pure oxygen, until waking up from general anesthesia. Animals in the control group were handled in the same way as those in the bTBI group, except that they were not subject to the blast wave.

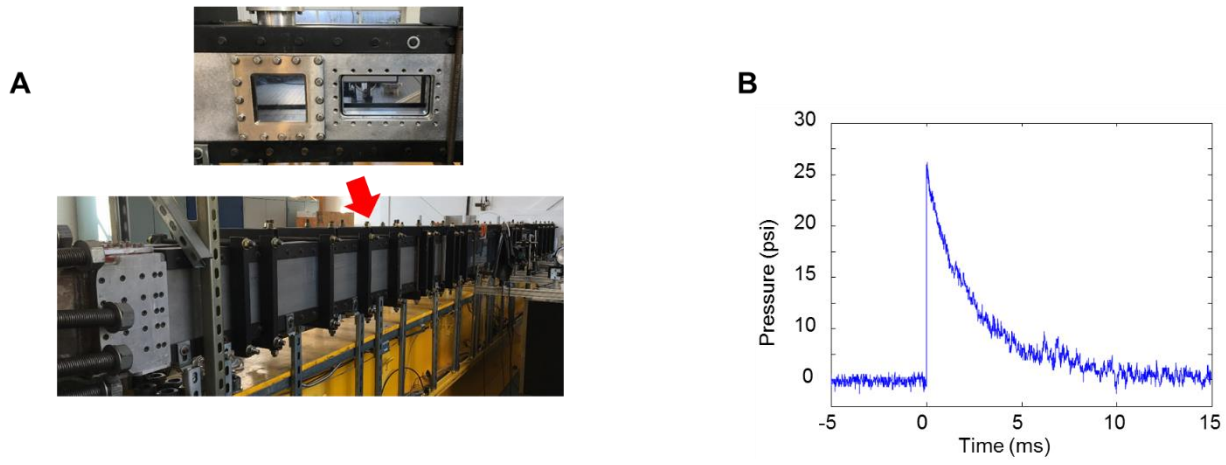

Fig. 5.1 A) The long tube for the high pressure shock and the window on the tube to place the animal with securing screws. B) The pressure profile of the blast shock

Before the PAM imaging, craniotomy was carefully performed following established protocols[187,188]. The animal was anesthetized with isoflurane (3% for induction and 1.5–2% for surgery). Toe pinch was performed to confirm that the

animal was fully sedated before starting the surgery. The scalp hair was shaved by a trimmer and then depilated by the hair removal cream (Surgi-cream). After the scalp was sterilized with 70% ethanol and povidone-iodine, a surgical incision was made and the periosteum was removed for craniotomy. A cranial window (~4 mm in diameter) was created using a dental drill. To avoid overheating, the drilling was paused every 30 seconds with saline flush. Once the skull became thin and deformable, it was removed using a fine forceps to expose the underlying tissue, followed by application of a pre-soaked soft-gel foam to prevent bleeding. After ultrasound gel was applied to the cranial window, the animal was transferred to the imaging site, where the exposed brain was in gentle touch with the transparent membrane at the bottom of a water tank for ultrasound coupling. During imaging, the animal was maintained under anesthesia with 1.5% isoflurane and the body temperature was kept at 37°C using a heating pad.

5.3 Cerebrovascular Dysfunction in bTBI

5.3.1 Influence of bTBI on the Cerebral Vasculature

Twelve bTBI rats and 7 control rats were imaged by PAM. The static pressure used to induce bTBI was measured to be 27.2±2.7 psi (187.8±18.3 kPa), falling into the range of moderate bTBI[189]. As shown in Fig. 5.2, the C_{Hb}, sO_2 and blood flow speed were directly measured by multi-parametric PAM in the control and bTBI rats, before and after ACZ injection. In response to the vasodilatory stimulation, marked increases in the venous sO_2 and blood flow speed were observed in the brain of the control rats (blue and red arrows in Fig. 5.2A, respectively). By contrast, no noticeable change was observed in the bTBI rats (Fig. 5.2B). To enable quantitative analysis, vessel segmentation was performed to extract C_{Hb}, sO_2, flow speed, and diameter of individual vessels, from which OEF, volumetric blood flow, and

$CMRO_2$ can be derived. To study vessel type-dependent responses, the imaged cerebral vessels were divided into four groups with a diameter threshold[190]: big arteries (≥45 μm), small arteries (<45 μm), big veins (≥45 μm), and small veins (<45 μm). As shown in Fig. 5.2C, the diameter distributions of the four types of vessels showed no statistically significant difference between the two groups, suggesting that no bias was introduced by vessel segmentation and that the moderate bTBI did not induce significant structural changes in the cerebral vasculature.

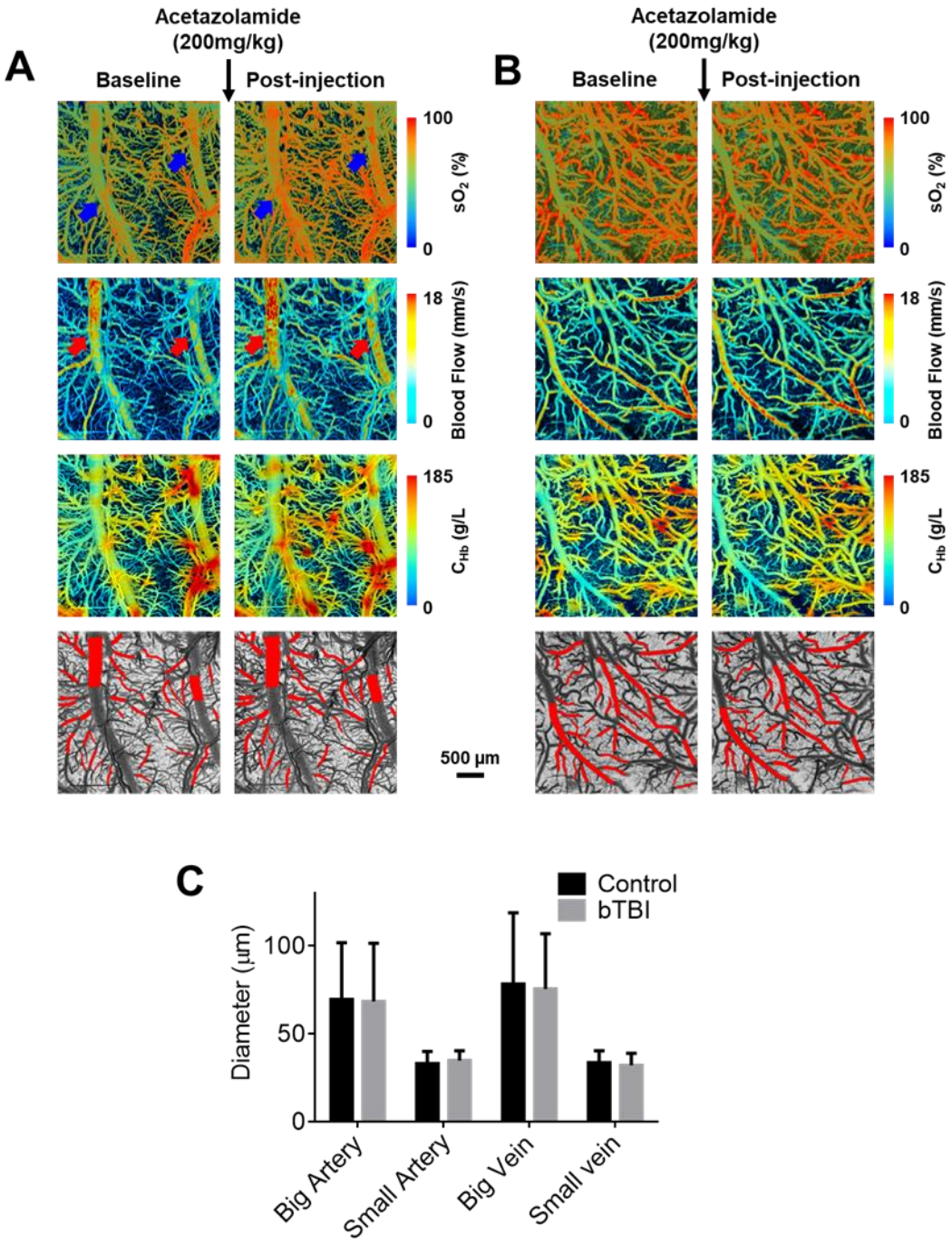

Fig. 5.2 Multi-parametric PAM and segmentation-based single-vessel analysis of bTBI-induced changes in the cerebral vasculature. The PAM images of the total hemoglobin concentration, blood oxygenation, and blood flow speed, as well as the corresponding vessel segment maps, acquired before and 15 minutes after injection

of acetazolamide in (A) a control rat and (B) a rat subjected to moderate bTBI (pressure: 196.5 kPa). (C) Statistical comparison of the vessel segment diameters between the control group and the bTBI group. Sample size: 35 big arteries, 55 small arteries, 62 big veins, and 57 small veins in the control group and 89 big arteries, 94 small arteries, 81 big veins, and 57 small veins in the bTBI group. Arrows: representative vessels showing changes in blood oxygenation and flow speed in response to the vasodilatory stimulation.

5.3.2 Cerebral Hemodynamic and Oxygen-metabolic Responses to Moderate bTBI

To investigate bTBI-induced functional changes in the cerebral vasculature, all hemodynamic and oxygen-metabolic parameters accessible to PAM were quantified and compared. As expected, the arterial and venous C_{Hb} showed no difference between the two groups (Fig. 5.3A). As shown in Fig. 5.3B, the average venous sO_2 in the bTBI rats (79.0±2.5%) was higher than that in the control rats (76.0±3.1%), while the average arterial sO_2 values of the two groups were similar (90.8±1.2% vs. 91.8±1.1% for the control and bTBI groups, respectively). Also, the average speed of venous blood flow in the bTBI rats was higher (but statistically insignificant) than that in the control rats (6.0±2.7 mm/s vs. 4.9±1.2 mm/s; Fig. 5.3C). The higher venous sO_2 resulted in a 14.7% lower OEF in the bTBI rats compared with that in the control rats (insignificant, p=0.138; Fig. 5.3D), while the higher venous flow speed was associated with an 18.8% higher total CBF (insignificant, p=0.562; Fig. 5.3E). Interestingly, the counterbalance effect the OEF and CBF led to similar $CMRO_2$ values in the two groups (71.0±36.0 μmol/100g/min vs. 73.3±46.8 μmol/100g/min for the control and bTBI groups, respectively; Fig. 5.3F).

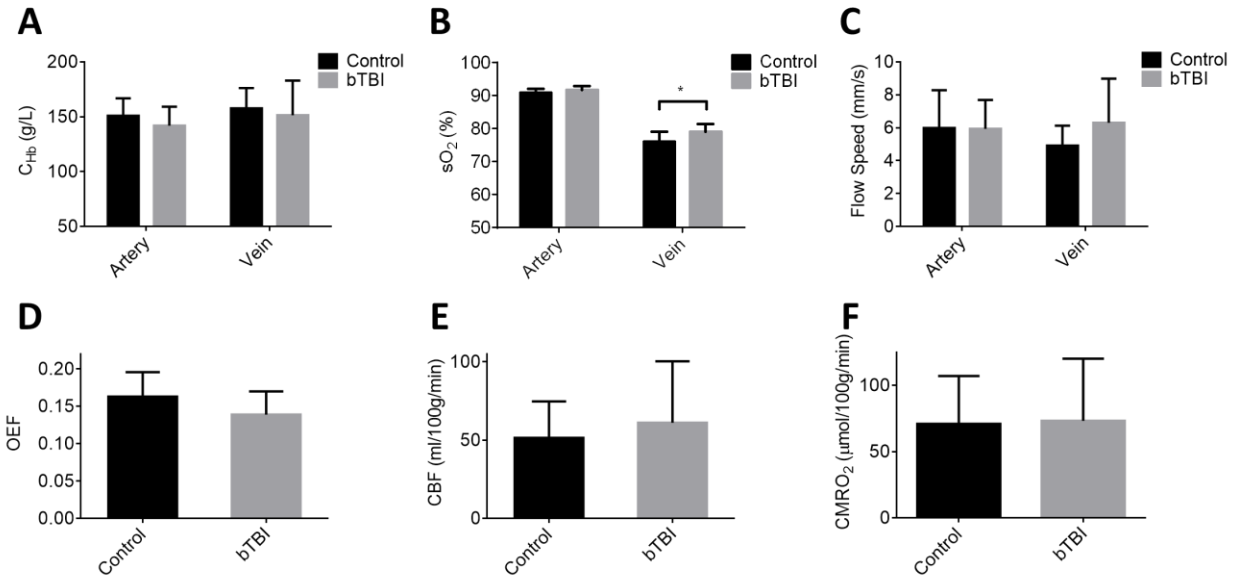

Fig. 5.3 Cerebral hemodynamic and oxygen-metabolic responses to bTBI. Statistical comparison of the (A) total hemoglobin concentration, (B) average arterial and venous blood oxygenation, (C) average arterial and venous blood flow speed, (D) regional oxygen extraction fraction, (E) regional cerebral blood flow, and (F) regional cerebral metabolic rate of oxygen between the control group and the bTBI group. Sample size: 7 control rats and 12 bTBI rats. *, $p<0.05$.

To examine whether the bTBI-induced functional changes were vessel type-dependent or not, we repeated this analysis for each of the four different types of vessels—including 35 big arteries, 55 small arteries, 62 big veins, and 57 small veins in the control group and 89 big arteries, 94 small arteries, 81 big veins, and 57 small veins in the bTBI group. The single-vessel analysis showed that the bTBI-induced change in venous sO_2 actually took place in the small rather than big veins (Fig. 5.4A) and that the increase in venous blood flow speed predominantly occurred in the big veins (Fig. 5.4B). Although the flow speeds in big veins were statistically different between the two groups, the corresponding volumetric flow values were

comparable (Fig. 5.4C), likely due to the smaller diameters of the big veins in the bTBI group (Fig. 5.2C).

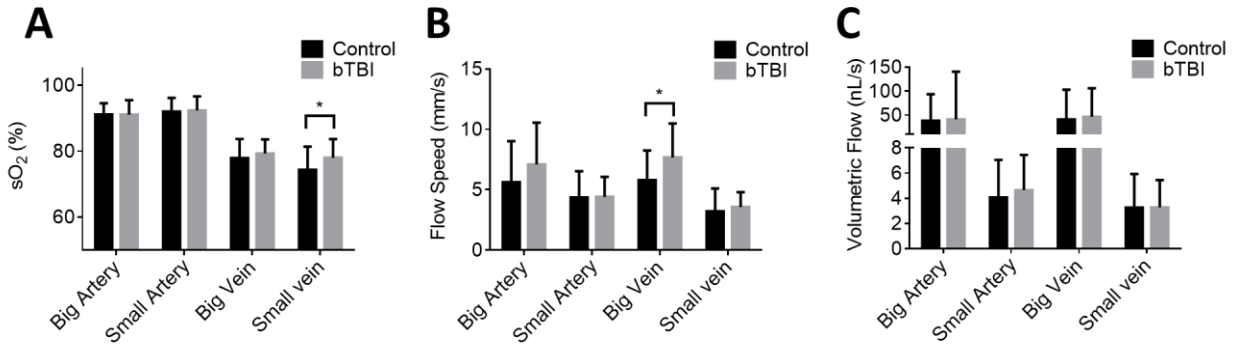

Fig. 5.4 Vessel type-dependent cerebrovascular responses to bTBI. Statistical comparison of the (A) blood oxygenation, (B) blood flow speed, and (C) volumetric blood flow between the control group and the bTBI group. Sample size: 35 big arteries, 55 small arteries, 62 big veins, and 57 small veins in the control group and 89 big arteries, 94 small arteries, 81 big veins, and 57 small veins in the bTBI group. *, $p<0.05$.

5.3.3 Cerebrovascular Reactivity to Vasodilatory Stimulation

Besides the comparison of cerebrovascular structure, function and associated metabolism between the bTBI and control rats, ACZ was employed to compare their cerebrovascular reactivity levels. As shown in Fig. 1A and 1B, visually different responses to ACZ were observed in the two groups. In contrast to the unchanged C_{Hb} (Fig. 5.5A), ACZ induced a 7.8% increase in the venous sO_2 of the control rats, which was significantly higher than the unchanged venous sO_2 in the bTBI rats (Fig. 5.5B). Along with the changes in sO_2, the arterial flow speeds in both groups and the venous flow speed in the control group were significantly elevated in response to the vasodilatory stimulation. However, the blood flow increase in the bTBI group was significantly less than that in the control group (Fig. 5.5C). The increased venous sO_2 in the control group resulted in a much reduced OEF (74.5% of the baseline), which was lower than that (87.2% of the baseline) in the bTBI group (not significant,

p=0.163; Fig. 5.5D). Accompanying the reduced OEF was the increased total CBF (Fig. 5.5E). The control rats showed a significantly larger increase in CBF (126.2% of the baseline) than the bTBI rats (106.2% of the baseline). The coupling of the OEF and CBF managed to keep the regional $CMRO_2$ unaffected by the vasodilatory stimulation for both groups (Fig. 5.5F), echoing previous reports[120,189,191].

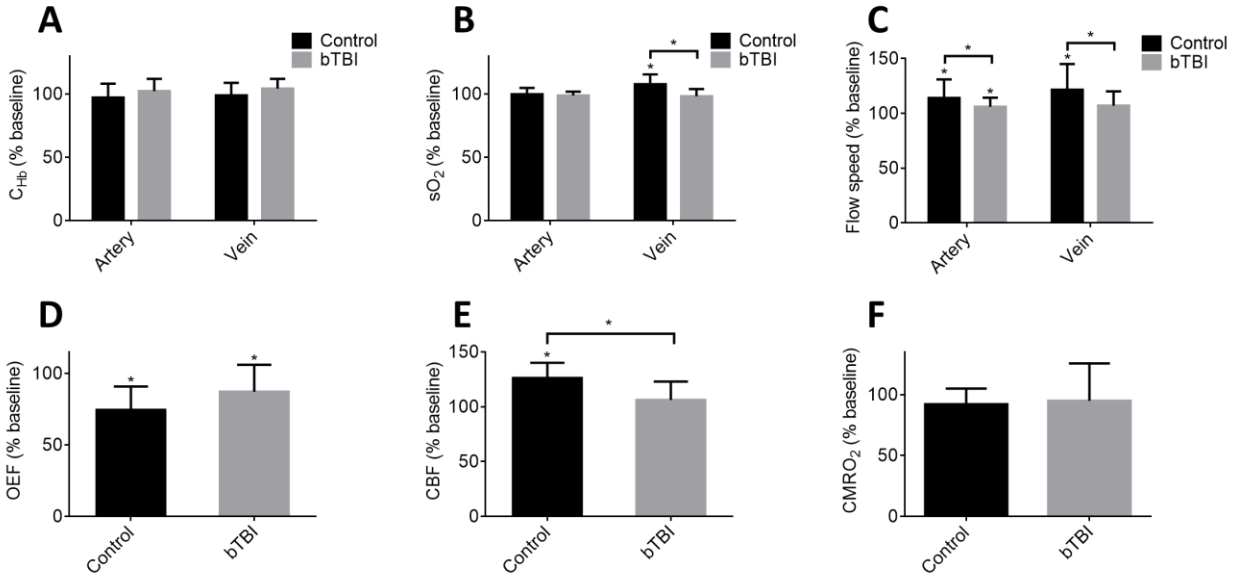

Fig. 5.5 Cerebral hemodynamic and oxygen-metabolic responses to the vasodilatory stimulation. Statistical comparison of acetazolamide-induced relative changes in the (A) total hemoglobin concentration, (B) average arterial and venous blood oxygenation, (C) average arterial and venous blood flow speed, (D) regional oxygen extraction fraction, (E) regional cerebral blood flow, and (F) regional cerebral metabolic rate of oxygen with their corresponding baselines (significance, if any, is indicated on the top of the columns) and between the control group and the bTBI group (significance, if any, is indicated between the two compared columns). Sample size: 7 control rats and 12 bTBI rats. *, $p<0.05$.

Again, to examine whether the bTBI-induced CVR changes were vessel type-dependent or not, we repeated this analysis for each of the four different types of vessels. As shown in Fig. 5.6A, ACZ induced significant sO_2 increases in both big and small veins in the control rats (107.9% and 111.5% of the baseline, respectively), but not in the bTBI rats (100.7% and 101.1% of the baseline for the big and small veins, respectively). Interestingly, the arterial sO_2 in the bTBI rats slightly dropped (statistically insignificant) after the ACZ injection, in contrast to the unchanged

arterial sO_2 in the control rats. Similarly, ACZ-induced arterial dilation was also abolished in the bTBI rats, but not in the control rats (106.6% and 114.0% of the baseline for the big and small arteries, respectively; Fig. 5.6B). Along with the increases in venous sO_2 and arterial diameter were flow speed increases in all types of vessels in the control rats (117.2%, 131.8%, 120.4% and 133.7% of the baseline for the big arteries, small arteries, big veins and small veins, respectively), in striking contrast to the much compromised flow responses in the bTBI rats (109.4%, 102.5%, 103.8% and 107.1% of the baseline for the big arteries, small arteries, big veins and small veins, respectively; Fig. 5.6C). Not surprisingly, the inability of the bTBI rats for vasodilation and regulation of flow speed led to the nearly abolished response in the volumetric blood flow to the ACZ stimulation (110.0%, 109.1%, 107.1% and 114.5% of the baseline for the big arteries, small arteries, big veins and small veins, respectively; Fig. 5.6D), in contrast to that in the control rats (134.0%, 180.5%, 126.2% and 146.2% of the baseline for the big arteries, small arteries, big veins and small veins, respectively).

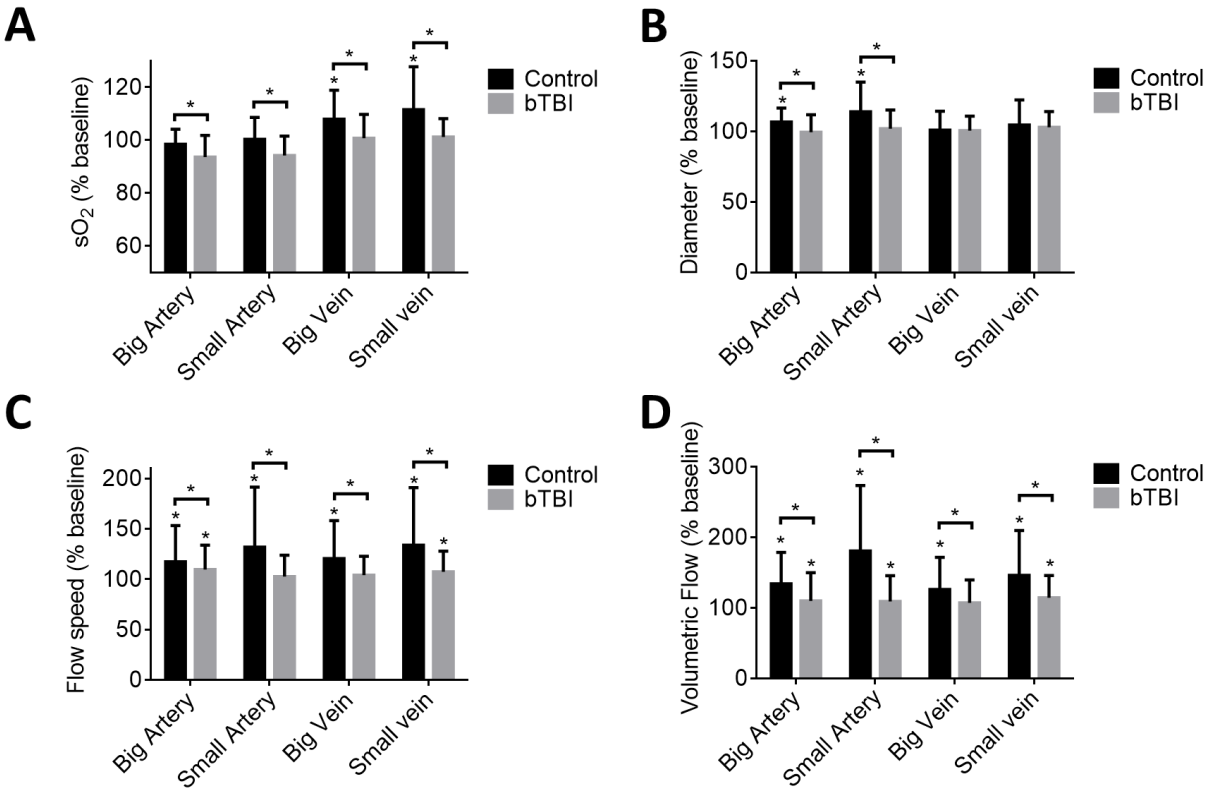

Fig. 5.6 Vessel type-dependent cerebrovascular reactivity to the vasodilatory stimulation. Statistical comparison of acetazolamide-induced relative changes in the (A) blood oxygenation, (B) vessel diameter, (C) blood flow speed, and (D) volumetric blood flow with their corresponding baselines (significance, if any, is indicated on the top of the columns) and between the control group and the bTBI group (significance, if any, is indicated between the two compared columns). Sample size: 35 big arteries, 55 small arteries, 62 big veins, and 57 small veins in the control group and 89 big arteries, 94 scmall arteries, 81 big veins, and 57 small veins in the bTBI group. *, $p<0.05$.

5.4 Discussion and Conclusion

In recent years, our understanding of the influence of TBI on the brain has undergone substantial expansion. Evidences emerging from preclinical and clinical studies

suggest that cerebrovascular dysfunction may play an important role in the neurodegeneration following TBI. Indeed, multiple forms of cerebrovascular dysfunction have been observed in TBI patients, including vasospasm, impaired CBF autoregulation, and BBB disruption. Post-TBI cerebral vasospasm is an important secondary insult occurring in more than one-third of the patients and is often associated with severe brain damage[192]. Impaired autoregulation of the CBF also contributes to the secondary injuries after TBI, likely by compromising oxygen delivery to the brain and consequently the cerebral oxygen metabolism[153]. It is worth noting that the degree of metabolic failure directly relates to the severity of brain damage—outcome is worse in TBI patients with lower cerebral metabolism compared to those with minor or no metabolic dysfunction[193]. Disruption of the BBB, happening even in mild TBI without overt bleeding, contributes to vasogenic edema—an important factor underlying the clinical outcome of TBI[153]. Complementary to these clinical evidences, a recent rodent study shows impaired dilatory capability of the cerebral vasculature after TBI[177].

Advances in clinical neuroimaging technologies, including computed tomography, magnetic resonance imaging, and positron emission tomography, have enabled direct imaging of the cerebral vasculatures in TBI patients. However, in cases of mild to moderate TBI with no external injuries, subtle changes in the cerebral vasculature, which may mainly happen in microvessels[194], are often invisible to these clinical imagers with macroscopic spatial resolutions. Two-photon microscopy, the technology of choice for intravital imaging of the rodent brain, has enabled visualization of the cerebral vasculature at the microscopic level. However, angiographic agents is required[94], which might cause physiological perturbations. Even with the aid of exogenous agents, comprehensive evaluation of the cerebrovascular function and associated oxygen metabolism remains inaccessible.

The lack of enabling tools for label-free comprehensive imaging of the cerebral vasculature at high spatial resolution has fundamentally limited our understanding of the vascular component of this devastating brain disorder[137,194–197].

The head-restrained multi-parametric PAM has filled this technology gap and shed new light on the bTBI-induced cerebrovascular dysfunction. Capitalizing on the optical absorption of blood hemoglobin, our PAM simultaneously imaged cerebrovascular anatomy, C_{Hb}, sO_2 and flow speed in both bTBI and control mice in a label-free manner (Fig. 1). With the aid of vessel segmentation, these structural and hemodynamic parameters were extracted at the single-microvessel level, from which volumetric blood flow, total CBF, OEF and $CMRO_2$ were also quantified. The capability of PAM for comprehensive characterization of the cerebral vasculature has enabled us to extend the evaluation of CVR from blood flow to other functional and metabolic parameters. Moreover, the high resolution and functional measurements of PAM allowed us to sort the cerebral vessels into different types, based on which the dependence of CVR on the vessel type was also revealed.

Using this enabling technology, we showed that the moderate bTBI did not induce significant changes in the cerebral microvascular structure and hemodynamics, as well as associated oxygen delivery and metabolism, except for slightly increased venous sO_2 and blood flow (Figs. 2 and 3). Interestingly, the reduced OEF (due to the increased venous sO_2) and the increased CBF remained tightly coupled in the TBI rats, maintaining the $CMRO_2$ at the same level of that in the control rats. This observation suggests that moderate bTBI is not likely to induce acute impairment in cerebral energy metabolism.

Although not inducing overt changes in cerebral hemodynamics and metabolism, the moderate bTBI significantly impaired the CVR, including abolished vasodilation and much compromised autoregulation of CBF and sO_2 (Figs. 4 and 5). Nicely

echoing previous chronic observations of impaired vasodilatory capability in TBI rats[177] and impaired CBF autoregulation in TBI patients[153], our result suggests a state of cerebrovascular hypo-reactivity immediately following blast exposure that may contribute to the long-term cerebrovascular pathology from the primary injury. Lacking the capability to regulate the cerebrovascular diameter, oxygenation and blood flow in response to hemodynamic/metabolic challenges, TBI patients may have increased vulnerability of the brain to hypoxia/ischemia insults[118,198].

There is plenty of room for improvement. Disruption of the BBB and the consequent vasogenic edema are essential vascular factors in the secondary injury process of TBI[174,199,200]. Exploiting the strong optical absorption of Evans blue, a commonly used dye for vascular permeability test[201], our PAM holds great potential to extend the classic Evans blue assay to *in vivo*. Moreover, label-free imaging of brain edema has been demonstrated by photoacoustic computed tomography[202]. Future development of the multi-parametric PAM to enable high-resolution imaging of BBB permeability and vasogenic edema will add to our understanding of TBI-induced cerebrovascular dysfunction. Another important form of vascular dysfunction in bTBI that has not been characterized by PAM is vasospasm. According to clinical observations, bTBI-induced cerebral vasospasm typically last for up to 30 days. To capture this chronic dysfunction, a long-lifetime cranial window technique needs to be developed for PAM. To date, the two major types of chronic windows for intravital brain imaging are the open-skull window and the reinforced thinned-skull window[65,188]. Although providing excellent visibility, the former is invasive and may activate microglia and astrocytes, thereby altering brain hemodynamics and activity. In contrast, the reinforced thinned-skull window provides chronic access to the brain with minimal inflammatory response and acceptable visibility, but requires labor-intensive maintenance. Future test and

adoption of these window technique(s) will not only grant PAM access to the chronically changed cerebrovascular parameters, but also enable it to longitudinally monitor how the TBI-induced multifaceted cerebrovascular dysfunction progresses over time.

We comprehensively and quantitatively characterized the moderate bTBI-induced cerebrovascular dysfunction in an established rat model of bTBI, using the state-of-the-art multi-parametric PAM technology. we found that moderate bTBI, although induces no external injuries and only minor changes in the blood oxygenation and flow, can significantly impair the cerebrovascular reactivity in terms of vasodilation, blood flow autoregulation, as well as blood oxygenation and extraction. These findings shed new light on the vascular component in the propagation of secondary injuries following bTBI and may facilitate the identification of new and promising therapeutic targets for this devastating disease.

Chapter VI: PAM of Hemodynamic and Metabolic Dysfunctions in Ischemic Stroke and Responses to Treatment

6.1 Background and Motivation

6.1.1 Neuroimaging for Ischemic Stroke

As the third leading cause of death and the leading cause of adult disability in the United States, Stroke affects 800,000 people in the United States every year, and ischemic stroke accounts for 87%[31]. According to the latest report, ischemic brain injury leads to more than 200,000 death annually in the U.S.A and lots of disabilities[203]. Although the risk of stroke increases with age and the stroke is most common among the elderly (60 or more years old), it can affect people of all ages, including children[204]. Typical risk factors for strokes include smoking, diabetes, hypertension, obesity, alcohol abuse, and carotid diseases[205]. The most common cause of ischemic stroke is the narrowing of the arteries in the neck or head, often caused by atherosclerosis, or gradual cholesterol deposition[206]. Within the narrowed arteries, blood cells have a higher possibility of forming blood clots and blocking the artery where they are formed. If the blocked artery is inside one of the brain's arteries, it triggers a thrombotic stroke. Meanwhile, the formed blood clots can also dislodge and become trapped in arteries close to the brain, leading to the embolic stroke.

Due to its high metabolic demand, the brain depends heavily on the blood supply, which bring fresh blood from the heart and lungs that carries oxygen and nutrients

to the brain and takes away carbon dioxide and cellular waste. Thus, the brain is very sensitive to the alternation of the blood flow. If some cerebral artery is blocked, the brain cells (mostly neurons) will be in short of oxygen and therefore energy, leading to cell deaths if the artery remains blocked for more than a few minutes[207]. Thus, immediate identification and medical treatment of the acute ischemic stroke is critical in clinical to reduce the severity and improve the outcome.

Brain ischemia can be classified into global and focal brain ischemia. Clinically, more patients suffer from focal brain ischemia. Based on cerebral blood flow, three zones have been recognized after focal brain ischemia[208]. With a blood flow less than 15% of the normal area, the ischemic core have severely injured cells. The cells inside this zone will easily die via necrosis if reperfusion cannot be established in time. The penumbral region lies outside the ischemic core and has a reduced blood flow (less than 40% of the normal). The reduced blood flow in this zone is maintained at sufficient levels to sustain neuronal membrane potentials and, hence, obviate membrane failure and terminal anoxic depolarization for the short term. The fate of cells in this zone are undetermined and can be altered, depending on the reperfusion and corresponding therapy approaches. Outside the penumbra, the zone has a normal blood flow where cells often has no problem survive for the long term.

The rapid advances in neuroimaging techniques provides the opportunity to better understand the ischemic stroke process. With the state-of-art neuroimaging techniques, the temporal and spatial progression of the penumbra can be identified[209]. Although the duration of the penumbra in human beings is still uncertain, recent reports showed that only 20%-30% of penumbra remained survivable after 6 hours[210]. The duration and evolutionary characteristics of the penumbra are particularly important for clinical applications and translational research, where time windows for therapy need to be considered as well as the topographical location of tissue to

be salvaged. However, there are still divergences in how to accurately differentiate the ischemic core and penumbra[209]. What is worse, the resolution of the most common neuroimaging techniques (such as PET and MRI) is usually low (more than hundreds of microns). This makes it more difficult to precisely define the penumbra region, especially in the animal model where the ischemic core may only be ~500 microns[13]. Meanwhile, to validate the recognized "penumbra" area, it usually requires the use of animal models, mostly rodent model[211]. Thus, high-resolution functional imaging of the penumbra region is in great need for the preclinical study of the ischemic stroke.

6.1.2 Hemodynamic and Metabolic Dysfunctions in Ischemic Stroke

Caused by the arterial block and severely reduced blood flow, the ischemic stroke involves significant hemodynamic alterations. Within certain range of blood supply alternation, the CBF will be auto-regulated to match metabolic demands of the brain through various mechanism, preventing potential cerebral ischemia[212]. Only when the CBF drops below certain values which exceed the CBF autoregulation capability, a series of functional and structural changes will be triggered which will culminate into irreversible impairment and lead to cell deaths[213]. The CBF changes were widely used to define the penumbra region, which is the most clinically relevant target in ischemic stroke and is the focus of active research due to its potential to recover from the ischemic challenge[211]. Thus, the measurement of CBF alteration in acute ischemic stroke is critical for evaluating the stroke severity, locating the ischemic core, monitoring the stroke progression and the therapy effect. Recent studies have shown that the CBF can well predict the final infarct volume and clinical outcome[214]. On the other hand, the reperfusion injury after ischemia has been observed and widely reported[215,216]. Although the reperfusion of blood help mitigating initial tissue

hypoxia, exacerbation of tissue injury may occur. Furthermore, the reperfusion injury will result in an impaired autoregulation of cerebral blood flow, contributing to further damage[217]. Thus, the blood flow measurement and control of reperfusion during recanalization using drugs like tPA is important for clinical applications.

Beyond the CBF quantification, gaining insights into brain oxygen metabolism is also of great interest in the study of ischemic stroke[218]. Cerebral oxygen metabolism is essential for generating a steady supply of energy for the normal neuronal activity of the brain. Accompany with the cerebral artery occlusion in the acute ischemic stroke, the alteration of $CMRO_2$ always happens in response to the ischemia[219]. Direct associated with the energy consumption of neurons, the imaging of $CMRO_2$ may provide a more direct assessment of tissue viability and therefore may be better imaging biomarkers for penumbral imaging than CBF. Since our multi-parametric PAM can measure all the parameter required for absolute $CMRO_2$ quantification (C_{Hb}, sO_2, CBF, OEF) at micron level resolution, it stands at a good position for the study of the hemodynamic and metabolic dysfunctions in ischemic stroke.

6.2 PAM of Middle Cerebral Arterial Occlusion (MCAO)-induced Ischemic Stroke

6.2.1 tMCAO Model for Ischemic Stroke

To better understand the brain pathophysiology and design new therapies for the ischemic stroke, numerous animal models have been explored to mimic the clinical ischemic stroke in the past several decades[220]. Accounting for approximately 70% of infarcts, the middle cerebral artery (MCA) and its branches are the most often affected cerebral vessels in human ischemic stroke[221]. Thus, the MCAO techniques are closely related to practical human ischemic stroke. As one of the most widely

used stroke models, MCAO can be accomplished by mechanical, pharmacological, photothrombotic or embolic means[222]. Although mostly used in rodents, the MCAO has also been reported in primate, canine, ovine and porcine studies using the same methodologies, demonstrating its translational potential[223].

Among those MCAO stroke models, intra-arterial suture/filament based tMCAO is the most common method in rodents[223]. Comparing to the invasive direct surgical occlusion of cerebral vessels, the intraluminal suture/filament based tMCAO is less invasive and does not require craniotomy, avoiding damage to cranial structures. Besides, plenty of studies show that the advantage of consistency in lesion size and location using intraluminal suture/filament based tMCAO compared to embolic models[223]. This technique involves temporarily occluding the common carotid artery, introducing a suture directly into the internal carotid artery or transected external carotid artery. Then, the suture will be advanced until it interrupts the blood supply to the MCA. It can be used for both permanent MCAO and transient MCAO. For the tMCAO, the most common durations are 60 minutes, 90 minutes, and 120 minutes[224]. In this study, we chose 90 minutes to be consistent with our previous study[225].

6.2.2 PAM of Cerebral Hemodynamics in tMCAO

The transient focal brain ischemia model was applied by using intraluminal filament to achieve MCAO (Fig. 6.1A), which was removed after 90 minutes. The laser Doppler flowmetry was applied to confirm the success of both the occlusion and reperfusion of the MCA. This model is well-characterized and widely-used and involves a relatively minor procedure. The transient focal brain ischemia allows a reperfusion phase, which may increase brain injury and give us an opportunity to document the hemodynamics and dynamics of oxygen supply and demand during

reperfusion. The surgery took no more than 15 minutes, during which the mouse will be anesthetized with 1.6% isoflurane and kept at 37°C. The animals was waken up soon after the MCAO is achieved. This practice limits anesthetic exposure during brain ischemia and reduces anesthetic effects on brain ischemic outcome.

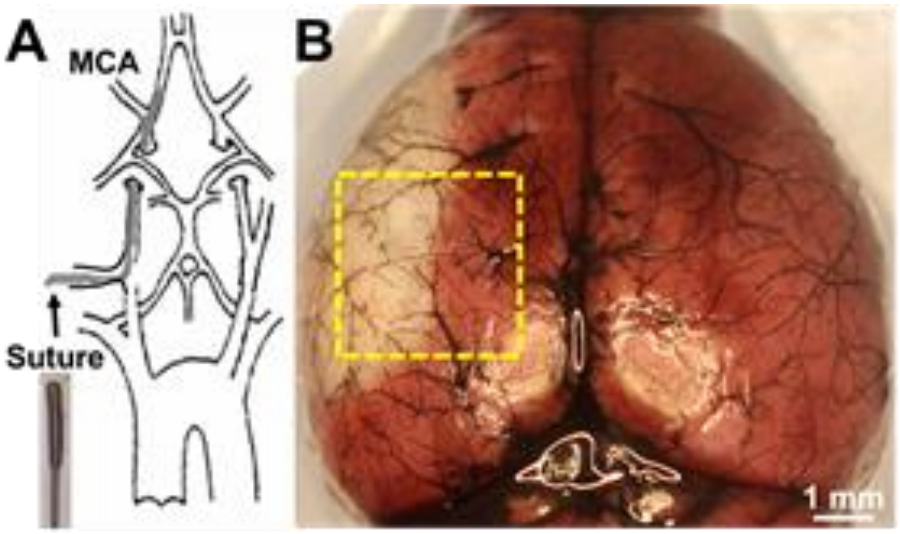

Fig 6.1 (A) MCAO procedure. (B) TTC stain 1 day after reperfusion from 90-minute tMCAO. Dashed box: ROI (3x3 mm2) for PAM.

To acquire the TTC stained brain that can be co-registered and compared with PAM images, the animal was perfused with 10-mL saline followed by 2-mL concentrated carbon black ink via the left cardiac ventricle until tissue turns black under deep anesthesia. After decapitation, the brain was incubated in phosphate-buffered saline (pH: 7.4) containing 2% TTC at 37°C for 30 minutes. The TTC-stained infarct picture (Fig. 6.1B) clearly showed both the infarct region and the cortex vasculature.

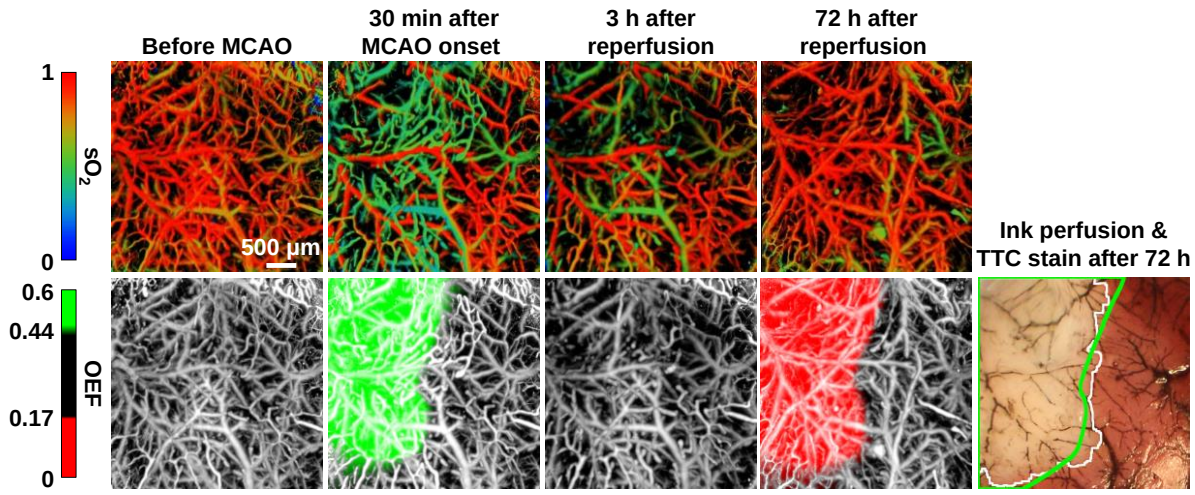

Fig. 6.2 Time-lapse PAM of the anesthetized mouse brain before, during, and up to 72 h after MCAO. The green and white curves in the ink+TTC picture correlate the low-OEF region identified by PAM with the infarct region determined by TTC staining.

To monitor the progression of the ischemic stroke, the longitudinal imaging of blood vessels and sO_2 was achieved (Fig. 6.2). The time-lapse PAM of the anesthetized mouse brain before, during, and 24 h after the tMCAO. After the PAM experiment, we perfused the cortical vasculature with carbon-black ink and then dissected the brain for TTC staining. Thus, the PAM image and TTC picture can be readily co-registered using the vascular landmarks to correlate PAM-measured hemodynamics and metabolism with TTC-determined brain infarct. As shown in Fig. 6.2, the OEF is significantly increased during 30 minutes after the MCAO onset (green area), indicating the strong need for oxygen extraction during the occlusion. But after 72 hours, the sO_2 in that region increased a lot from the MCAO onset and reperfusion, showing a large drop of OEF within that area. The low OEF area measured by our PAM showed well matched location as the TTC staining, which demonstrate the capability of our PAM to detect the infarct region through the OEF alteration.

However, imaging the mouse brain under anesthesia introduced a bias in the sO_2 measurement, preventing us from getting the true baseline. According to the results shown in previous chapter, the venous sO_2 was significantly elevated under anesthesia, which make it difficult to differentiate the arteries from veins. What is worse, the anesthesia applied during the imaging may have the neuroprotective effect against ischemic stroke, making it unsuitable for the mechanistic study of other drug's neuroprotection. Thus, we further explored the feasibility of imaging the awake mouse brain using the system described in previous chapter.

Different than the anesthetized brain, the cerebral arteries and veins can be readily differentiated in the baseline image as shown in Fig. 6.3. The distal end of the MCA was also identifiable on the left within the region of interest. Comparing to the baseline sO_2 and CBF, the MCAO-induced ischemia and reduced CBF, were easily observed at 1 hour after MCAO. Meanwhile, the hypoxia was also observed within the region majorly supplied by MCA. In contrast, the images at 24 hour after MCAO showed increased venous sO_2 and partially recovered CBF. The increased sO_2 leaded to a lowered OEF and $CMRO_2$, indicating few surviving cells and therefore few oxygen consumption. The corresponding TTC picture also showed good match with our PAM images.

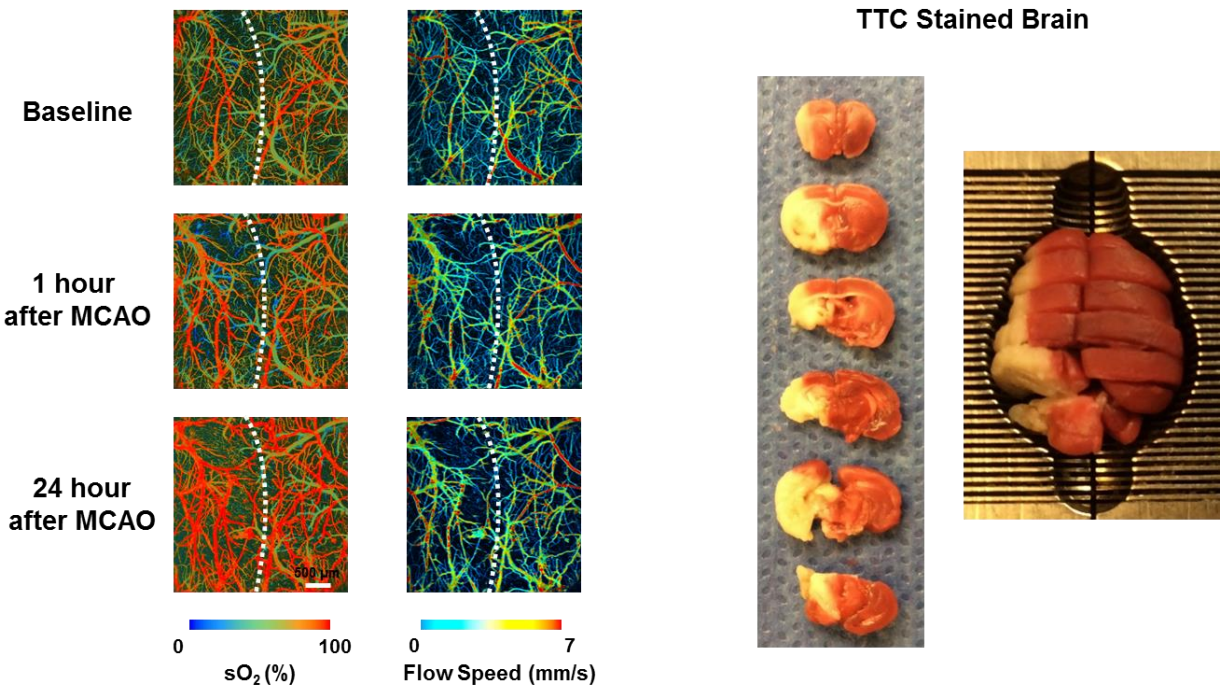

Fig. 6.3 The time-lapse PAM of the awake mouse brain before, during, and 24 h after MCAO. The TTC staining brain was shown on the right with cross-section view and top-down view.

6.3 PAM of Sphingosine-1-phosphate (S1P) Treatment against Ischemic Stroke

6.3.1 Blood S1P level

Despite many decades of intensive research, clinically practicable therapeutic options for the ischemic stroke patients are still very limited[226]. As the major therapy option, many neuroprotective agents have been explored to reduce the severity of ischemic stroke and improve the outcome[227]. However, although promising improvement have been shown in different preclinical studies using animal model, none of these drugs unequivocally has shown an improvement in clinical outcomes[228]. In clinical practice, the most common therapies focused on the

reperfusion of obstructed blood vessels using either thrombolytic or mechanical recanalization[229]. However, the CBF restoration with excessive reperfusion will increase the reactive oxygen species generation and exacerbates the brain injury, which requires extreme carefulness in clinical and limits the application of stroke reperfusion strategies. Although the lack of oxygen and nutrient is harmful to neurons, ischemia-reperfusion injury also induces the compromise of BBB, excessive metabolic stress and inflammatory responses in the neurovascular unit[230].

The bioactive metabolic product of sphingolipids, sphingosine-1-phosphate (S1P) is attracting more attention because of its neuroprotection against ischemic stroke[231]. Recent studies has shown that S1P is vasoprotective and neuroprotective via various mechanisms[232]. Another finding also showed that the S1P can promote erythrocyte glycolysis and oxygen release for adaptation to hypoxia, which may help lowering the impairment of ischemic brain injury[233]. However, the underlying mechanism how S1P affect the cerebral metabolism is still unclear. To investigate it, the effective regulation of S1P level and appropriate tool for cerebral metabolism measurement are both needed. S1P is generated solely by sphingosine kinases (SphKs), of which there are two isoforms (SphK1 and SphK2). Thus, the S1P level can be regulated via the activation or inhibition of the SphK1 and SphK2[234]. Although virtually all cells are capable of synthesizing S1P, the tissue levels are low compared with blood and lymph, where S1P circulates at single digit micromolar levels. Meanwhile, as shown in previous chapters, multi-parametric PAM is ideal for the measurement of the cerebral metabolism of oxygen. Therefore, the cerebral hemodynamics in response to S1P levels can be imaged using our multi-parametric PAM, which may reveal the underlying hemodynamic mechanism of S1P neuroprotective effect against ischemic stroke.

In this study, the blood S1P levels are regulated through the selective inhibitor of SphK2 (SLM6031434), while the less potent R-enantiomer (SLM6081442) was used for the control group. The details of the synthesis of SLM6041434 [S-2-(3-[4-(octyloxy)-3-(trifluoromethyl)phenyl]-1,2,4-oxadiazol-5-yl)pyrrolidine-1-carboximidamide], SLM6081442 [R-2-(3-[4-(octyloxy)-3-(trifluoromethyl)phenyl]-1,2,4-oxadiazol-5-yl) pyrrolidine-1-carboximidamide] can be found in previous reports[235].

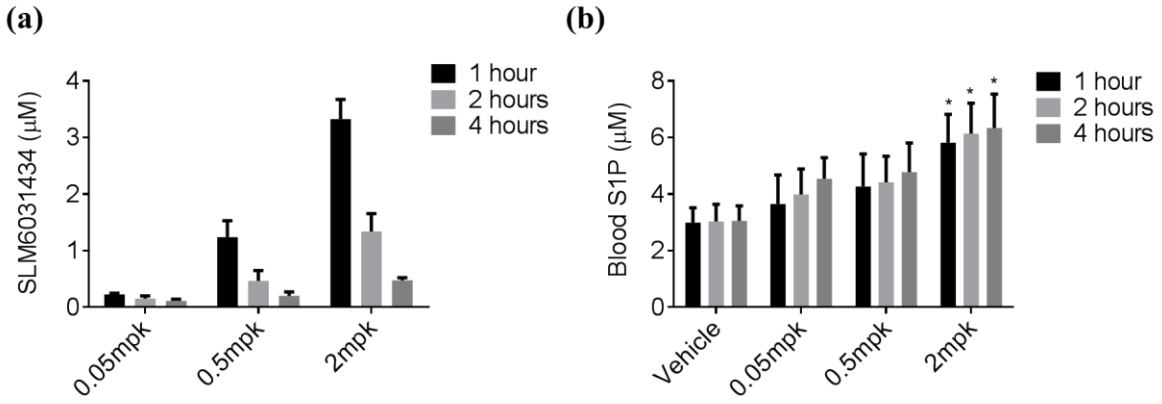

Fig. 6.4 (a) SLM6031434 level and (b) Blood S1P level at 1 hour, 2 hours, and 4 hours after injection of the saline (vehicle, n=4) or different dose of SLM6031434 compound (n=4).

To confirm the S1P regulation using our compound SLM6031434, groups of 8-9 week old male cd-1 mice were injected through the tail vein 2 mg/kg (mpk). After the injection, animals were bled at three time points (1 hour, 2 hours, and 3 hours). Whole blood was processed immediately for LC/MS analysis following the sample preparation protocols in previous report[236]. Then, analyses were performed by LC-ESI MS using a Waters system (Milford, MA) consisting of a triple quadrupole mass spectrometer (Xevo TQ-S) and a solvent pump (Acquity UPLC). As shown in Fig. 6.4, 3 different doses were used (0.05 mpk, 0.5 mpk, 2 mpk) to measure the dose-dependent response. After the injection, animals were bled at three time points (1

hour, 2 hours, and 4 hours) for the quantification of the SLM6031434 content and blood S1P level using LC/MS analyses. As shown in Fig. 6.4a, the increased SLM6031434 content in the blood quickly dropped to a low level in all dosages, indicating the SLM6031434 was continuously in effect. Meanwhile, the blood S1P showed the increasing trend in all three different dosages 1 hour after the injection (22 % for 0.05 mpk, 43% for 0.5 mpk, and 94% for 2 mpk), which showed a positive correlation to the dosage (Fig. 6.4b). Meanwhile, the blood S1P level continued to increase till 4 hours after the injection. In our later experiments, the dosage of 2 mpk was chosen for hemodynamics changes and neuroprotection study, which doubled the blood S1P level 2 hours after the injection..

6.3.2 Effect of S1P on Cerebral Hemodynamics

To investigate how S1P affect the cerebral hemodynamics, our head-restraint PAM was applied for the awake mouse brain imaging. The system configuration can be found in Chapter III. Using this PAM system, the awake mouse brain was imaged under normoxia before and 2 hours after the injection of 2mg/kg compound SLM6031434, which is expected to almost double the blood S1P level in two hours. As shown in Fig 6.5, no changes was observed after the injection. The purpose of choosing the time point at 2 hours after the injection is to accommodate with our pre-treatment experiment, in which the active drug was injected two hours before the MCAO procedure.

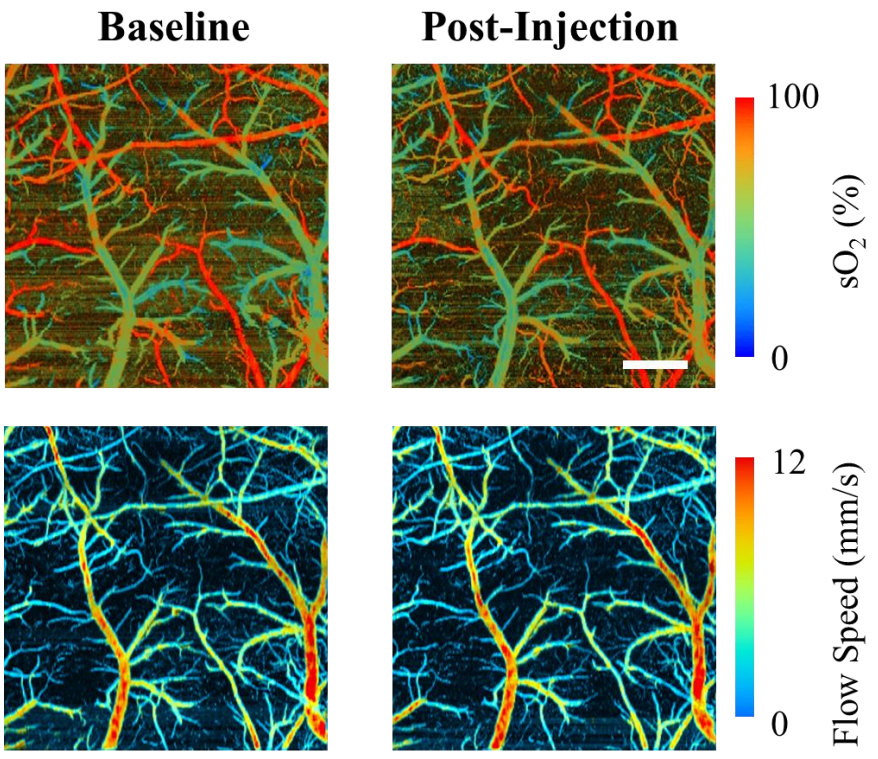

Fig. 6.5 Cerebral sO2 and blood flow of the awake mouse before and after the injection of "active" compound SLM6031434 under normoxia. Scale bar, 500 μm.

To further check the influence of S1P on cerebral hemodynamics, the hypoxia challenge was introduced, which usually happens in the ischemic brain. The hypoxia applied in this study refers to ~12% oxygen content, produced by mixing the medical air and pure nitrogen. Then the active and inactive drug was administrated into the awake mouse under hypoxia through the tail vein, with the help of the pre-implanted needle. As shown in Fig. 6.6, the drop of both arterial and venous sO2 was observed under hypoxia condition, accompany with the blood flow speed increase. With the "inactive" compound, both the blood oxygenation and flow speed remained almost unchanged 2 hours after the injection. On the contrary, the sO_2 recovery was observed with the active drug after 2 hours, while the blood flow is unchanged.

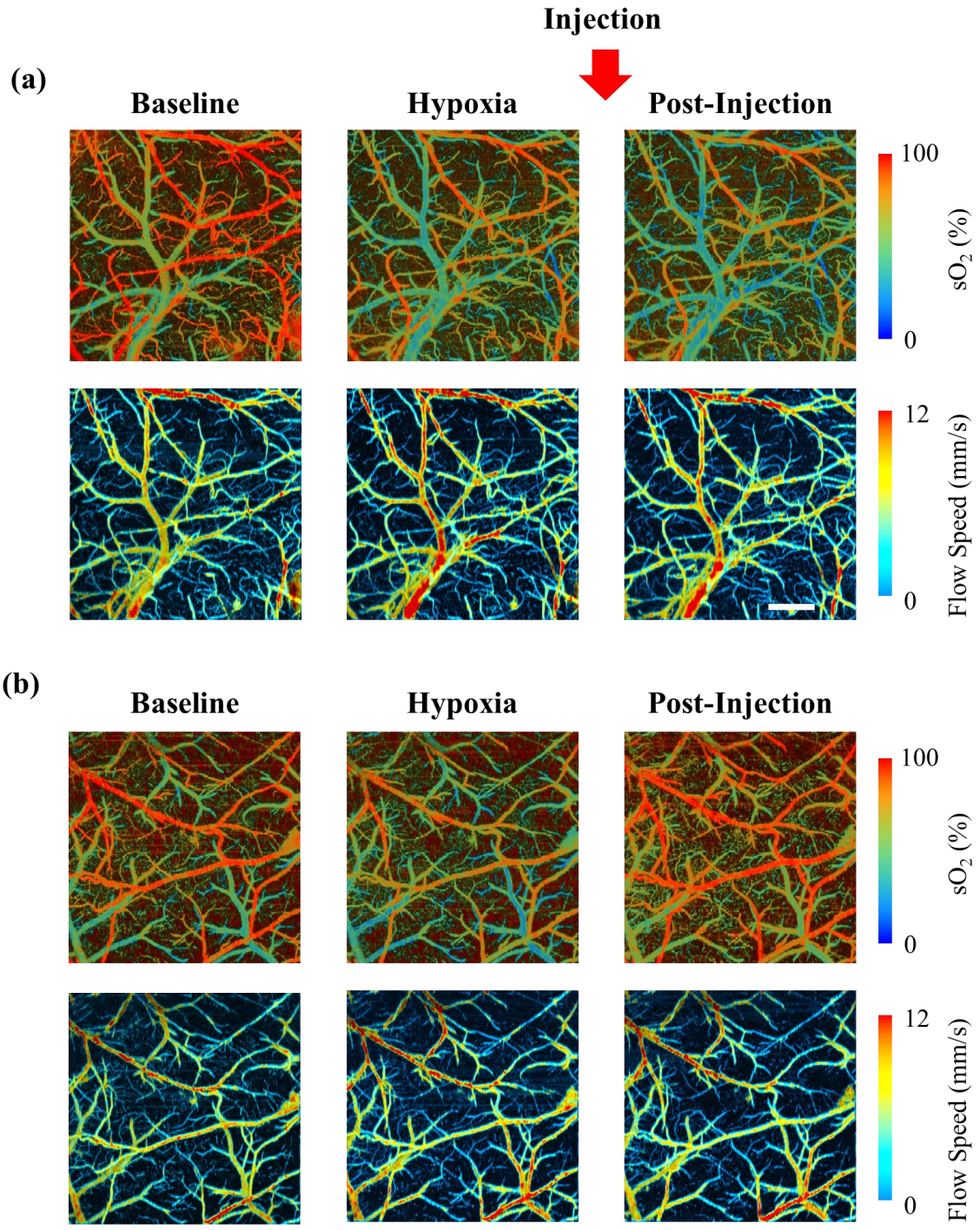

Fig. 6.6 Cerebral sO_2 and blood flow of the awake mouse before the injection of the (a) "inactive" compound SLM6081442 and (b) "active" compound SLM6031434 before the injection under normoxia and hypoxia and after the injection under hypoxia. Scale bar, 500 μm.

To better understand the observation, experiments were repeated in 4 mice to perform statistical analysis of the cerebral hemodynamic responses. As shown in Fig. 6.7a, C_{Hb} was not significantly affected by the active compound. While the arterial and venous sO_2 dropped due to hypoxia, they recovered back to the similar level as the baseline after the injection (Fig. 6.7b and Fig. 6.7c). This leads to the drop of OEF under hypoxia, comparable to the baseline level. Meanwhile, the blood flow speed and average vessel diameter was not affected by the drug. Combining the dropped OEF and unchanged CBF, the $CMRO_2$ was found to decrease, indicating a lower oxygen requirement for metabolism.

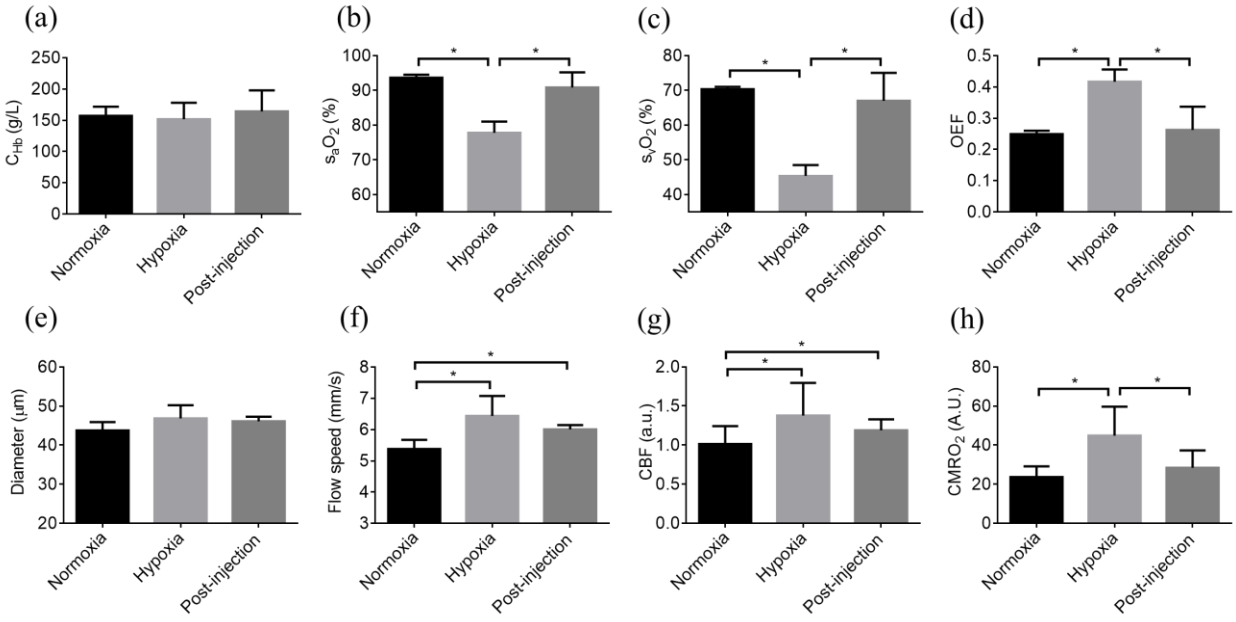

Fig. 6.7 (a) The hemoglobin concentration, (b) arterial sO_2, (c) venous sO_2, (d) OEF, (e) average vessel diameter, (f) average blood flow speed, (g) total CBF, and (h) $CRMO_2$ under normoxia and hypoxia before and after the injection of compound SLM6031434 (n=4). Data are shown as Mean ± SD. *, $p<0.05$.

Considering the fact that the S1P level kept increasing for several hours after the SLM6031434 compound injection (Fig. 6.4), the time course of cerebral

hemodynamic changes was also investigated. The mouse was firstly imaged under normoxia, then switched to hypoxia. Under hypoxia, the active compound was injected and the cerebral hemodynamics were imaged four times with 30 minutes interval. Each scanning took about 20 minutes. As shown in Fig 6.8a, the sO_2 did not significantly change immediately after the injection. The C_{Hb} remains unaffected (Fig. 6.8b). Instead, it is a gradually change of oxygenation after the injection (Fig 6.8c and Fig. 6.8d), while diameter, blood flow speed, and CBF remain the same. Thus, the significant drop of $CMRO_2$ was only observed after 1.5 hours.

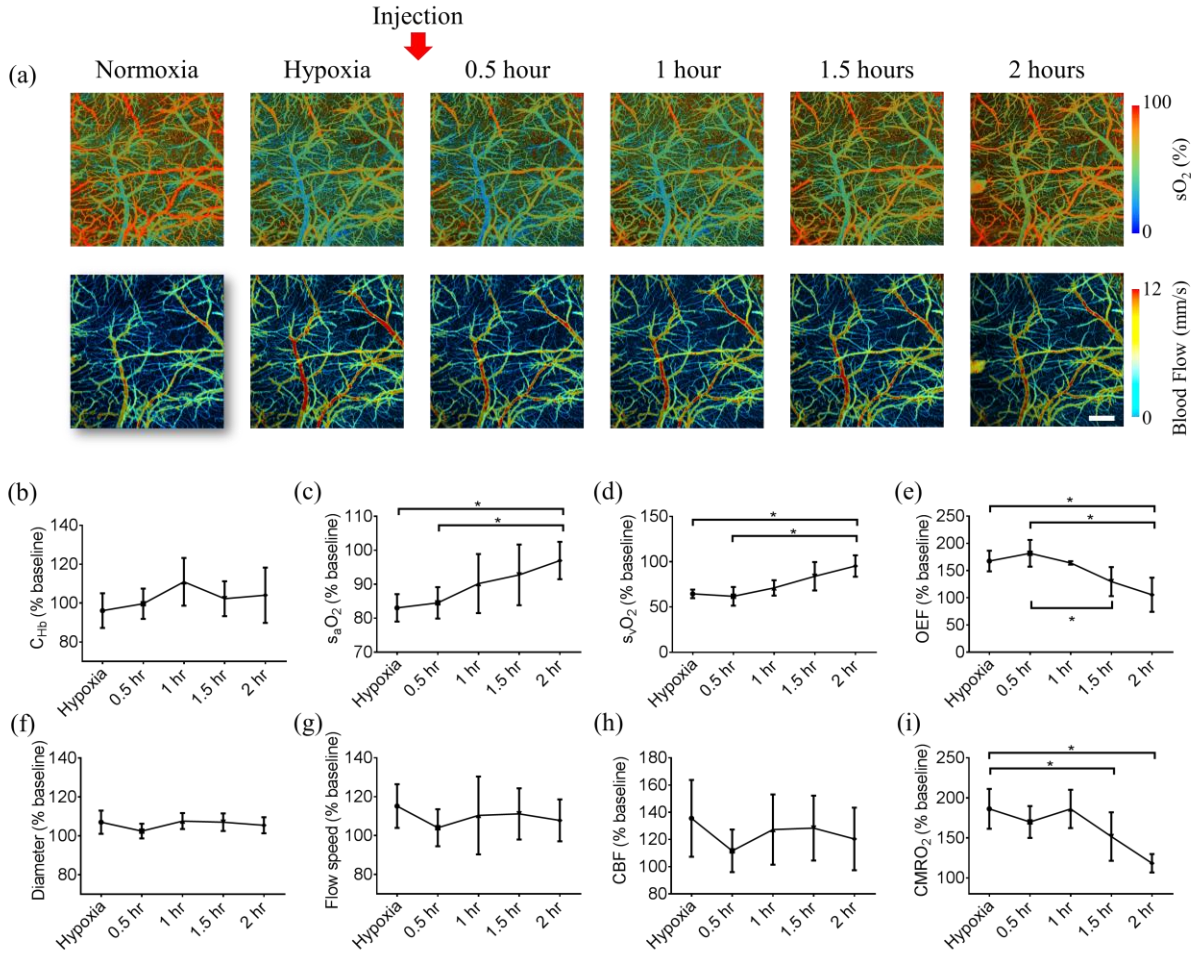

Fig. 6.8 (a) the time course of the cerebral hemodynamic changes before the injection (normoxia and hypoxia) and several time point after the injection (0.5h, 1h, 1.5h, 2h). (b) The hemoglobin concentration, (c) arterial sO_2, (d) venous sO_2, (e) OEF, (f)

average vessel diameter, (g) average blood flow speed, (h) total CBF, and (i) CRMO2 under normoxia and hypoxia before and after the injection of compound SLM6031434. Data are shown as Mean ± SD. *, $p<0.05$.

6.3.3 Stroke Outcome Evaluation after S1P Treatment

To evaluate the pre-treatment and post-treatment neuroprotection of S1P, mice were randomly assigned into 3 groups (control, pre-treatment, and post-treatment). The mouse in the pre- treatment group was injected with the active compound through the tail vein 2 hours prior to the MCAO procedure, while the post-treatment group was injected immediately after the reperfusion. After the injection, the animal was returned to cage and closely monitored until the outcome evaluation and brain harvest. As shown in the representative TTC images (Fig. 6.9a), the infract region is noticeable smaller in the pre-treatment mouse, comparing to the control mouse. However, the post-treatment mouse didn't show improved outcome in infarct volume. The statistical analysis (Fig. 6.9b, n=7 for each group) showed significant reduced infract volume in the pre-treatment group (26.8 ± 11.6 %) comparing to the control group (62.5 ± 6.9 %), while the post-treatment group did not show improvement in infarct volume (52.8 ± 17.4 %).

Besides, the rotarod performance test was also done to measure the ischemic stroke induced motor coordination impairment (Fig. 6.9c). Although all mice showed impaired motor coordination (ratio < 0.5), the pre-treatment group showed better motor function comparing to control group and post-treatment group. Furthermore, the neurological deficit score was also used to evaluate the stroke outcome (Fig. 6.9d). Both the control group (average score: 4.4) and the post-treatment group (average score: 4.2) showed severely affected behaving, most of which only circled or walked to one side. In the contrast, most mice in the pre-treatment group (average

score: 2.9) still have spontaneous movement in all directions and only do contralateral circling when pulled by the tail.

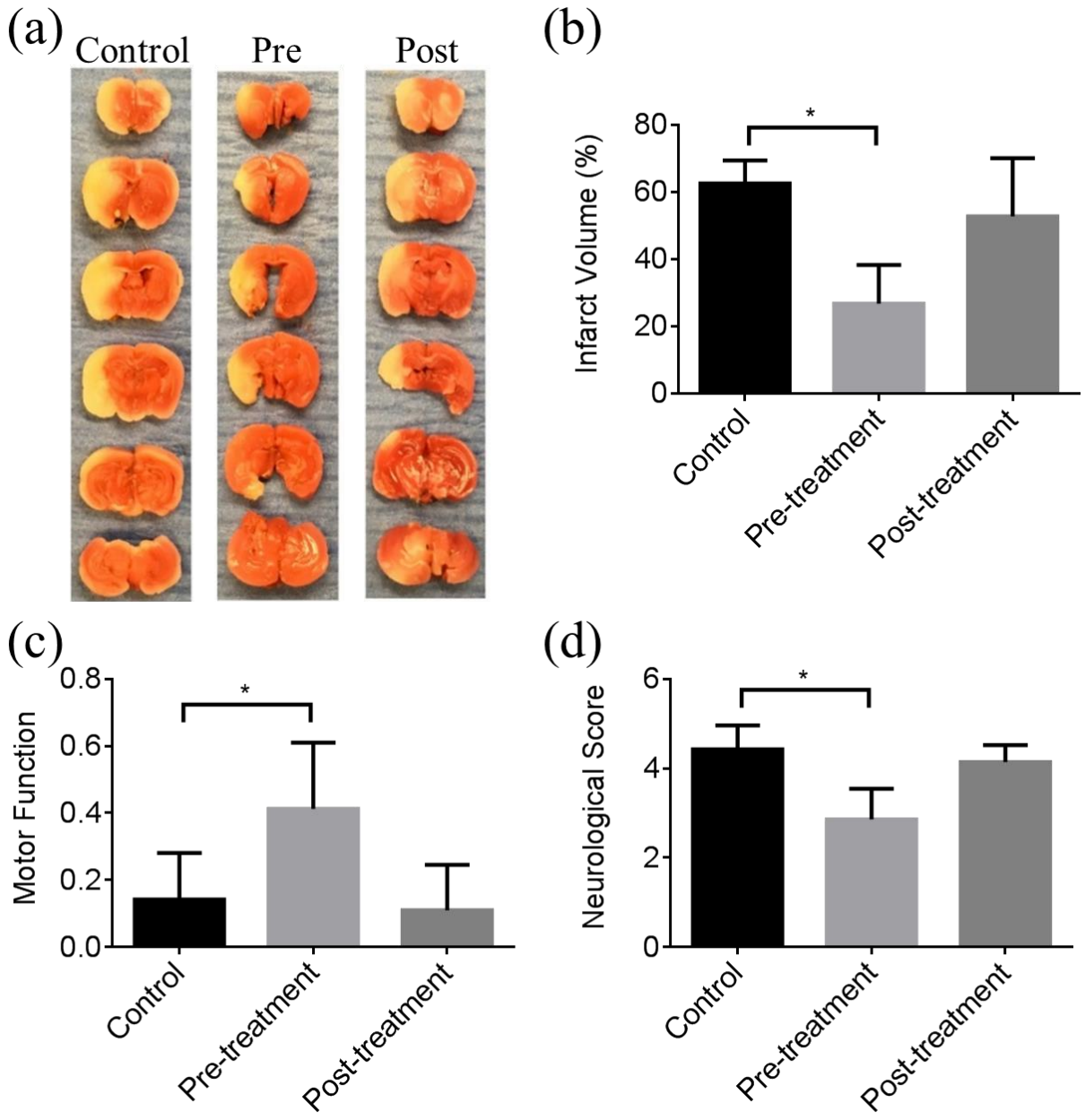

Fig. 6.9 (a) Representative images of TTC staining of six brain coronal slices harvested 24 hours after tMCAO. Statistical analysis of (b) infarct volume, (c) motor function, (d) neurological score in the control group (n=7), pre-treatment group (n=7), and post-treatment group (n=7). *, $p<0.05$.

6.4 Discussion and Conclusion

The blood S1P regulation was achieved using the selective inhibitor of SphK2 (SLM6031434). Although S1P synthesis relies on two different form of SphKs, SphK1 and SphK2, our results showed that the injection of our SphK2 inhibitor actually increased the blood S1P level within 4 hours, in contrast to S1P reduction by SphK1 inhibitor[237]. The result and previous studies suggest that blood S1P turns over may be due to the role of SphK2 in the clearance of S1P from the blood[235]. However, the mechanism whereby S1P is cleared from the blood is not fully understood, and the role of SphK2 in this process is still unknown. Besides, the whole blood S1P was measured in this study, which includes S1P in different components such as erythrocyte, platelet, and plasma. However, the roles of SphK1 and SphK2 in different components is not the same. For instance, SphK1 has a larger effect on erythrocyte and plasma S1P than SphK2, while the SphK2 plays a more important role in platelet S1P[238]. Therefore, further studies may be needed for better understanding of the S1P induced hemodynamics using our selective SphK2 inhibitor.

In previous studies, the S1P is reported to be neuroprotective against ischemic stroke via multiple mechanisms[239–242]. However, due to the lack of imaging tools, the response of cerebral hemodynamics and oxygen metabolism to S1P is still unclear, although it may play important roles in the ischemic stroke. Sun *et al* recently reported the elevated S1P promote the oxygen release for adaptation to high-altitude hypoxia[233]. Furthermore, the S1P pathway and its kinase were also reported to be related to the hypoxia signaling such as hypoxia-inducible factor in cancer and considered as potential targets for cancer therapy[243,244]. However, according to the best of our knowledge, there is no direct *in vivo* measurement of the S1P-induced

oxygenation and $CMRO_2$ changes in awake animals. In this study, our results show that the S1P elevation resulted in changes of brain oxygenation and $CMRO_2$ under hypoxia, but not under normoxia. These observation provides direct evidence that S1P may play an important role under hypoxia, which happens in multiple diseases (i.e., ischemic stroke, cancer) and extreme condition such as high altitude.

According to our measurements, the cerebral hemodynamics under hypoxia was altered 2 hours after the injection of our selective S1hK2 inhibitors, which was shown to double the baseline blood S1P level. Specifically, both the arterial and venous sO_2 increased, leading to the decreased OEF. Meanwhile, the blood flow speed and vessel diameter is not influenced by increased S1P level. Therefore, the reduced $CMRO_2$ under awake mouse brain was observed with elevated blood S1P. Our hypothesis is that the cerebral metabolism has been reprogrammed to slowly shift from oxygen respiration to glycolysis, which consumes less oxygen for energy metabolism. Recent findings showed evidence that the increased S1P enhances the release of membrane-bound glycolytic enzymes to the cytosol, induces glycolysis and thus the production of 2,3-bisphosphoglycerate (2,3-BPG)[233]. Other reports also showed that S1P increases glucose uptake through trans-activation of insulin receptor[245]. Interestingly, the cerebral sO_2 was unchanged under normoxia condition, even when the blood S1P level is elevated. This metabolic reprogramming may need to be triggered by the hypoxia related signaling factors, which may happen during ischemic stroke. Through the improved glucose uptake and promoted glycolysis, the oxygen metabolic requirement for oxygen is lowered, which may help the cells in the ischemic brain to survive through the challenge.

Furthermore, the neuroprotective effect of S1P against ischemic stroke was investigated using tMCAO model in both the pre-treatment group (2 hours prior to the occlusion) and post-treatment group (immediately after the reperfusion). While

obvious neuroprotection was observed in the pre-treatment group, no improvement was shown in the post-treatment group. The potential reason for the difference is that the cerebral metabolism changes in response to S1P elevation is a slow process, as shown in Fig. 4. The slow metabolism response after injection (~2 hours) may not be rapid enough to protect the cells within penumbra area in post-treatment group. Therefore, the S1P induced neuroprotection may be minimal in the post-treatment group.

In summary, the head-restraint multi-parametric PAM was applied to image the S1P-induced cerebral hemodynamic changes in awake mouse brain. Our results showed the S1P elevation led to the recovery of sO_2 under hypoxia, while the blood flow remained unchanged. Therefore, the $CMRO_2$ was reduced under hypoxia with the blood S1P increase, indicating the potential neuroprotective mechanism through lowering the metabolic needs of oxygen. Furthermore, the time course of cerebral hemodynamics was also shown, which showed the gradually changes of the sO_2, OEF, and $CMRO_2$ after the drug injection. Further experiments with tMCAO showed the neuroprotection of S1P in the pre-treatment group, which has smaller infarct volume, better neurological deficit score, and improved motor coordinate functions. Providing new insight of S1P-induced cerebral hemodynamics under hypoxia, this study may provide the opportunity better understanding the neuroprotection of S1P against ischemic stroke.

Chapter VII: Conclusion and Perspective

In this dissertation, I presented the design, implementation, validation, and the application of multi-parametric PAM, which are capable of simultaneously imaging C_{Hb}, sO_2, and CBF at the microscopic level for the first time. Therefore, the metabolic rate of oxygen can be quantified. This technical innovation is expected to shed new light on the mechanism and treatment of a broad spectrum of metabolic disorders. In Chapter III, first-of-a-kind head-restrained PAM was demonstrated, which extend our imaging capability to the awake mouse brain. This enabling technology offers the first opportunity to comprehensively and quantitatively characterize the hemodynamic and oxygen-metabolic responses of the mouse brain to isoflurane, a general anesthetic widely used in preclinical research and clinical practice. In Chapter IV, more comprehensive imaging analysis algorithm based on the head-restrained PAM was proposed to measure the vascular density, tortuosity, shear stress, and resistance. Beside, with the help of Evans blue dye, the evaluation of BBB permeability was achieved. Also, multifaceted cerebrovascular reactivity (CVR) to acetazolamide-based stimulation was also enabled in the awake mouse brain. In Chapter V, the capability of our PAM to evaluate the cerebrovascular dysfunctions after bTBI was demonstrated. Although no pronounced changes in the cerebral vasculature and oxygen metabolism was observed after moderate bTBI, the impaired cerebrovascular reactivity was found in the bTBI rats. This study is the first to comprehensively characterize the cerebrovascular responses to bTBI. In Chapter VI, the feasibility of using our PAM to image the hemodynamic changes during acute ischemic stroke was demonstrated using the tMCAO model in both the anesthetized mouse and awake mouse. Using this PAM system, the neuroprotective mechanism of S1P was investigated, which showed altered cerebral oxygenation

when challenged under hypoxia. This reduced metabolism need under hypoxia may play an important role in its neuroprotection.

The potential directions of future multi-parametric PAM development are anticipated as following:

- Faster system for multi-parametric PAM. The scanning speed of the current system is limited by the raster scanning strategy, which solely relied on the motor movement. Thus, the scanning of a 3x3 mm^2 area takes about 30 minutes, with the step size of 0.1 micron in B-scan direction and 10 microns in another direction. Although it is okay to use for some brain disease models, it is unable to catch the fast changes in the brain. Employing the hybrid scanning methods or designed scanning route with compressed sensing may greatly improve the scanning speed.
- PAM with deeper penetration depth. Visible wavelengths (532 nm and 559 nm) were used in the current system, limiting the penetration depth to be around 300 microns if we require good lateral resolution. A straightforward solution was to use longer wavelengths, i.e. 1064 nm to achieve deeper penetration, benefit from less scattering. However, this may require high sensitivity ultrasound transducer because of lower absorption of hemoglobin at this wavelength range. Another possible solution is using beam shaping and adaptive optics technique to compensate the tissue scattering, which can generate a good focus in deep tissue. To achieve this, enormous efforts will be need due to the complexity of brain structure.
- Wearable PAM for rodent brain imaging in freely move animal. In this dissertation, we showed the capability of using head-restraint PAM to image the awake mouse brain with high resolution. However, there is concern about

the potential stress related to the head-restraint apparatus, even with proper training. The wearable or head-mounted PAM will minimize the stress and allows the imaging of moving rodent.

- PAM of glucose uptake in the brain. As another major energy source for cell metabolism, the PAM measurement of glucose uptake will provide the opportunity to understand the specific role of cellular respiration and glycolysis under severe brain challenge, such as ischemic stroke or brain tumor. Although direct PAM measurement of glucose is possible, it suffers from the weak signal and strong water absorption. Appropriate glucose may be the potential solution for this direction.
- PAM of tissue level oxygenation in the brain. The oxygenation measurement in our current PAM system mainly relies on the hemoglobin, which cannot be used to measure the tissue oxygen. One promising solution is to apply the photoacoustic lifetime imaging, which may be capable to measure the partial pressure of oxygen (pO_2) in tissue. Another potential solution is to explore some contrast agent for tissue oxygen, such as some well-designed gold nanoparticles.

REFERENCES

1. Cogan, S. F. Neural Stimulation and Recording Electrodes. *Annu. Rev. Biomed. Eng.* **10,** 275–309 (2008).
2. Sakadzić, S. *et al.* Two-photon high-resolution measurement of partial pressure of oxygen in cerebral vasculature and tissue. *Nat. Methods* **7,** 755–759 (2010).
3. Horton, N. G. *et al.* In vivo three-photon microscopy of subcortical structures within an intact mouse brain. *Nat. Photonics* **7,** 205–209 (2013).
4. Wang, R. K. Optical microangiography: A label-free 3-D imaging technology to visualize and quantify blood circulations within tissue beds in vivo. *IEEE J. Sel. Top. Quantum Electron.* **16,** 545–554 (2010).
5. Chong, S. P., Merkle, C. W., Leahy, C., Radhakrishnan, H. & Srinivasan, V. J. Quantitative microvascular hemoglobin mapping using visible light spectroscopic Optical Coherence Tomography. *Biomed. Opt. Express* **6,** 1429 (2015).
6. Dunn, A. K., Bolay, H., Moskowitz, M. A. & Boas, D. A. Dynamic Imaging of Cerebral Blood Flow Using Laser Speckle. *J. Cereb. Blood Flow Metab.* **21,** 195–201 (2001).
7. Bouchard, M. B., Chen, B. R., Burgess, S. A. & Hillman, E. M. C. Ultra-fast multispectral optical imaging of cortical oxygenation, blood flow, and intracellular calcium dynamics. *Opt. Express* **17,** 15670 (2009).
8. Culver, J. P. *et al.* Diffuse optical tomography of cerebral blood flow, oxygenation, and metabolism in rat during focal ischemia. *J Cereb Blood Flow Metab* **23,** 911–924 (2003).
9. Eggebrecht, A. T. *et al.* Mapping distributed brain function and networks

with diffuse optical tomography. *Nat. Photonics* **8,** 448–454 (2014).

10. Smith, K. Brain imaging: FMRI 2.0. *Nature* **484,** 24–26 (2012).
11. Chang, C. & Glover, G. H. Time-frequency dynamics of resting-state brain connectivity measured with fMRI. *Neuroimage* **50,** 81–98 (2010).
12. Hafezparast, M., Ahmad-Annuar, A., Wood, N. W., Tabrizi, S. J. & Fisher, E. M. Mouse models for neurological disease. *Lancet Neurol* **1,** 215–24 (2002).
13. Shih, A. Y. *et al.* The smallest stroke: occlusion of one penetrating vessel leads to infarction and a cognitive deficit. *Nat. Neurosci.* **16,** 55–63 (2013).
14. Hillman, E. M. C. Optical brain imaging in vivo: techniques and applications from animal to man. *J. Biomed. Opt.* **12,** 51402 (2007).
15. Dorand, R. D., Barkauskas, D. S., Evans, T. A., Petrosiute, A. & Huang, A. Y. Comparison of intravital thinned skull and cranial window approaches to study cns immunobiology in the mouse cortex. *IntraVital* **3,** (2014).
16. Xu, H. T., Pan, F., Yang, G. & Gan, W. B. Choice of cranial window type for in vivo imaging affects dendritic spine turnover in the cortex. *Nat. Neurosci.* **10,** 549–551 (2007).
17. Raichle, M. E. & Gusnard, D. A. Appraising the brain's energy budget. *Proc. Natl. Acad. Sci.* **99,** 10237–10239 (2002).
18. Wang, L. V. *et al.* Photoacoustic Tomography: In Vivo Imaging from Organelles to Organs. *Science (80-.).* **335,** 1458–1462 (2012).
19. Nie, L. & Chen, X. Structural and functional photoacoustic molecular tomography aided by emerging contrast agents. *Chem. Soc. Rev.* **43,** 7132–70 (2014).
20. Wang, L. V. & Yao, J. A practical guide to photoacoustic tomography in the life sciences. *Nat. Methods* **13,** 627–638 (2016).
21. Hall, C. N., Klein-Flugge, M. C., Howarth, C. & Attwell, D. Oxidative

Phosphorylation, Not Glycolysis, Powers Presynaptic and Postsynaptic Mechanisms Underlying Brain Information Processing. *J. Neurosci.* **32,** 8940–8951 (2012).

22. Blass, J. P. Brain metabolism and brain disease: Is metabolic deficiency the proximate cause of Alzheimer dementia? in *Journal of Neuroscience Research* **66,** 851–856 (2001).
23. Yao, J. *et al.* High-speed label-free functional photoacoustic microscopy of mouse brain in action. *Nat. Methods* **12,** 407–410 (2015).
24. Yao, J., Maslov, K. I., Zhang, Y., Xia, Y. & Wang, L. V. Label-free oxygen-metabolic photoacoustic microscopy in vivo. *J. Biomed. Opt.* **16,** 76003 (2011).
25. Ning, B. *et al.* Simultaneous photoacoustic microscopy of microvascular anatomy, oxygen saturation, and blood flow. *Opt. Lett.* **40,** 910 (2015).
26. Yao, J., Maslov, K. I., Shi, Y., Taber, L. A. & Wang, L. V. In vivo photoacoustic imaging of transverse blood flow by using Doppler broadening of bandwidth. *Opt. Lett.* **35,** 1419–21 (2010).
27. Sheth, S. A. *et al.* Linear and nonlinear relationships between neuronal activity, oxygen metabolism, and hemodynamic responses. *Neuron* **42,** 347–355 (2004).
28. MacKenzie, H. A. *et al.* Advances in photoacoustic noninvasive glucose testing. in *Clinical Chemistry* **45,** 1587–1595 (1999).
29. Yao, J. & Wang, L. V. Photoacoustic brain imaging: from microscopic to macroscopic scales. *Neurophotonics* **1,** 11003 (2014).
30. Yao, J. *et al.* Noninvasive photoacoustic computed tomography of mouse brain metabolism in vivo. *Neuroimage* **64,** 257–266 (2013).
31. Roger, V. L. *et al.* Heart disease and stroke statistics-2012 update: A report from the American heart association. *Circulation* **125,** 188–197 (2012).

32. Zhang, H. F., Maslov, K., Sivaramakrishnan, M., Stoica, G. & Wang, L. V. Imaging of hemoglobin oxygen saturation variations in single vessels in vivo using photoacoustic microscopy. *Appl. Phys. Lett.* **90,** 53901 (2007).
33. Ning, B. *et al.* Ultrasound-aided Multi-parametric Photoacoustic Microscopy of the Mouse Brain. *Sci. Rep.* **5,** 18775 (2015).
34. Everds, N. *The Laboratory Mouse*. *The Laboratory Mouse* (Elsevier, 2004). doi:10.1016/B978-012336425-8/50070-4
35. Chen, S.-L., Ling, T., Huang, S.-W., Won Baac, H. & Guo, L. J. Photoacoustic correlation spectroscopy and its application to low-speed flow measurement. *Opt. Lett.* **35,** 1200–1202 (2010).
36. Chen, S.-L., Xie, Z., Carson, P. L., Wang, X. & Guo, L. J. In vivo flow speed measurement of capillaries by photoacoustic correlation spectroscopy. *Opt. Lett.* **36,** 4017–9 (2011).
37. Unekawa, M. *et al.* RBC velocities in single capillaries of mouse and rat brains are the same, despite 10-fold difference in body size. *Brain Res.* **1320,** 69–73 (2010).
38. DeFelipe, J. The evolution of the brain, the human nature of cortical circuits, and intellectual creativity. *Front. Neuroanat.* **5,** 29 (2011).
39. Chong, S. P., Merkle, C. W., Leahy, C. & Srinivasan, V. J. Cerebral metabolic rate of oxygen (CMRO_2) assessed by combined Doppler and spectroscopic OCT. *Biomed. Opt. Express* **6,** 3941 (2015).
40. Maslov, K., Zhang, H. F., Hu, S. & Wang, L. V. Optical-resolution photoacoustic microscopy for in vivo imaging of single capillaries. *Opt. Lett.* **33,** 929 (2008).
41. Hu, S., Maslov, K. & Wang, L. V. Second-generation optical-resolution photoacoustic microscopy with improved sensitivity and speed. *Opt. Lett.* **36,** 1134 (2011).

42. Yeh, C., Soetikno, B., Hu, S., Maslov, K. I. & Wang, L. V. Microvascular quantification based on contour-scanning photoacoustic microscopy. *J. Biomed. Opt.* **19,** 96011 (2014).
43. Stosiek, C., Garaschuk, O., Holthoff, K. & Konnerth, A. In vivo two-photon calcium imaging of neuronal networks. *Proc. Natl. Acad. Sci. U. S. A.* **100,** 7319–24 (2003).
44. Kleinfeld, D. & Griesbeck, O. From Art to Engineering? The Rise of In Vivo Mammalian Electrophysiology via Genetically Targeted Labeling and Nonlinear Imaging. *PLoS Biol.* **3,** e355 (2005).
45. Chen, X. *et al.* LOTOS-based two-photon calcium imaging of dendritic spines in vivo. *Nat. Protoc.* **7,** 1818–1829 (2012).
46. Greenberg, D. S., Houweling, A. R. & Kerr, J. N. D. Population imaging of ongoing neuronal activity in the visual cortex of awake rats. *Nat. Neurosci.* **11,** 749–751 (2008).
47. Qiu, M., Ramani, R., Swetye, M., Rajeevan, N. & Constable, R. T. Anesthetic effects on regional CBF, BOLD, and the coupling between task-induced changes in CBF and BOLD: An fMRI study in normal human subjects. *Magn. Reson. Med.* **60,** 987–996 (2008).
48. Kaisti, K. K. *et al.* Effects of sevoflurane, propofol and adjunct nitrous oxide on regional cerebral blood flow, oxygen consumption, and blood volume in humans. *Anesthesiology* **99,** 603–613 (2003).
49. Martin, C., Martindale, J., Berwick, J. & Mayhew, J. Investigating neural–hemodynamic coupling and the hemodynamic response function in the awake rat. *Neuroimage* **32,** 33–48 (2006).
50. Shtoyerman, E., Arieli, A., Slovin, H., Vanzetta, I. & Grinvald, A. Long-term optical imaging and spectroscopy reveal mechanisms underlying the intrinsic signal and stability of cortical maps in V1 of behaving monkeys. *J. Neurosci.*

20, 8111–8121 (2000).

51. Helmchen, F., Fee, M. S., Tank, D. W. & Denk, W. A miniature head-mounted two-photon microscope: High-resolution brain imaging in freely moving animals. *Neuron* **31,** 903–912 (2001).
52. Dombeck, D. A., Harvey, C. D., Tian, L., Looger, L. L. & Tank, D. W. Functional imaging of hippocampal place cells at cellular resolution during virtual navigation. *Nat. Neurosci.* **13,** 1433–1440 (2010).
53. Scott, B. B. B., Brody, C. D. D. & Tank, D. W. W. Cellular Resolution Functional Imaging in Behaving Rats Using Voluntary Head Restraint. *Neuron* **80,** 371–384 (2013).
54. Harvey, C. D., Collman, F., Dombeck, D. A. & Tank, D. W. Intracellular dynamics of hippocampal place cells during virtual navigation. *Nature* **461,** 941–6 (2009).
55. Hamel, E. J. O. J. O., Grewe, B. F. F., Parker, J. G. G. & Schnitzer, M. J. J. Cellular Level Brain Imaging in Behaving Mammals: An Engineering Approach. *Neuron* **86,** 140–159 (2015).
56. Dombeck, D. A., Khabbaz, A. N., Collman, F., Adelman, T. L. & Tank, D. W. Imaging Large-Scale Neural Activity with Cellular Resolution in Awake, Mobile Mice. *Neuron* **56,** 43–57 (2007).
57. Robles, F. E., Wilson, C., Grant, G. & Wax, A. Molecular imaging true-colour spectroscopic optical coherence tomography. *Nat. Photonics* **5,** 744–747 (2011).
58. Yi, J., Chen, S., Backman, V. & Zhang, H. F. In vivo functional microangiography by visible-light optical coherence tomography. *Biomed. Opt. Express* **5,** 3603–3612 (2014).
59. Hu, S. Listening to the Brain With Photoacoustics. *IEEE J. Sel. Top. Quantum Electron.* **22,** 1–10 (2016).

60. Jo, J., Zhang, H., Cheney, P. D. & Yang, X. Photoacoustic detection of functional responses in the motor cortex of awake behaving monkey during forelimb movement. *J. Biomed. Opt.* **17,** 110503 (2012).
61. Tang, J., Dai, X. & Jiang, H. Wearable scanning photoacoustic brain imaging in behaving rats. *J. Biophotonics* **9,** 570–575 (2016).
62. Zuo, Z. Are volatile anesthetics neuroprotective or neurotoxic? *Med. Gas Res.* **2,** 10 (2012).
63. Zwerus, R. & Absalom, A. Update on anesthetic neuroprotection. *Curr. Opin. Anaesthesiol.* **28,** 424–30 (2015).
64. Yang, G., Pan, F., Parkhurst, C. N., Grutzendler, J. & Gan, W.-B. B. Thinned-skull cranial window technique for long-term imaging of the cortex in live mice. *Nat. Protoc.* **5,** 201–208 (2010).
65. Drew, P. J. *et al.* Chronic optical access through a polished and reinforced thinned skull. *Nat. Methods* **7,** 981–984 (2010).
66. Nakao, Y. *et al.* Effects of anesthesia on functional activation of cerebral blood flow and metabolism. *Proc. Natl. Acad. Sci. U. S. A.* **98,** 7593–7598 (2001).
67. Rusy, B. F. & Komai, H. Anesthetic depression of myocardial contractility: a review of possible mechanisms. *Anesthesiology* **67,** 745–66 (1987).
68. Stullken, E. H., Milde, J. H., Michenfelder, J. D. & Tinker, J. H. The nonlinear responses of cerebral metabolism to low concentrations of halothane, enflurane, isoflurane, and thiopental. *Anesthesiology* **46,** 28–34 (1977).
69. Yablonskiy, D. A. Cerebral metabolic rate in hypercapnia: controversy continues. *J. Cereb. Blood Flow Metab.* **31,** 1502–1503 (2011).
70. Horvath, I., Sandor, N. T., Ruttner, Z. & McLaughlin, a C. Role of nitric oxide in regulating cerebrocortical oxygen consumption and blood flow

during hypercapnia. *J. Cereb. blood flow Metab.* **14,** 503–509 (1994).

71. Hedenstierna, G. & Rothen, H. U. in *Comprehensive Physiology* (John Wiley & Sons, Inc., 2012). doi:10.1002/cphy.c080111
72. Vestergaard, M. B. *et al.* Acute hypoxia increases the cerebral metabolic rate – a magnetic resonance imaging study. *J. Cereb. Blood Flow Metab.* **36,** 1046–1058 (2015).
73. Zaugg, M., Lucchinetti, E., Behmanesh, S. & Clanachan, A. S. Anesthetic cardioprotection in clinical practice from proof-of-concept to clinical applications. *Curr. Pharm. Des.* **20,** 5706–26 (2014).
74. Bilotta, F. *et al.* Pharmacological perioperative brain neuroprotection: a qualitative review of randomized clinical trials. *Br. J. Anaesth.* **110,** 113–20 (2013).
75. Kitano, H., Kirsch, J. R., Hurn, P. D. & Murphy, S. J. Inhalational Anesthetics as Neuroprotectants or Chemical Preconditioning Agents in Ischemic Brain. *J. Cereb. Blood Flow Metab.* **27,** 1108–1128 (2006).
76. Masamoto, K. & Kanno, I. Anesthesia and the quantitative evaluation of neurovascular coupling. *J. Cereb. Blood Flow Metab.* **32,** 1233–47 (2012).
77. Fox, P. T. & Raichle, M. E. Focal physiological uncoupling of cerebral blood flow and oxidative metabolism during somatosensory stimulation in human subjects. *Proc. Natl. Acad. Sci. U. S. A.* **83,** 1140–4 (1986).
78. Kaisti, K. K. *et al.* Effects of Surgical Levels of Propofol and Sevoflurane Anesthesia on Cerebral Blood Flow in Healthy Subjects Studied with Positron Emission Tomography. *J. Am. Soc. Anesthesiol.* **96,** 1358–1370 (2002).
79. Franceschini, M. A. *et al.* The effect of different anesthetics on neurovascular coupling. *Neuroimage* **51,** 1367–77 (2010).
80. Wang, T. *et al.* Multiparametric photoacoustic microscopy of the mouse

brain with 300-kHz A-line rate. *Neurophotonics* **3,** 45006 (2016).

81. Willie, C. K. *et al.* Utility of transcranial Doppler ultrasound for the integrative assessment of cerebrovascular function. *J. Neurosci. Methods* **196,** 221–237 (2011).
82. Peterson, E. C., Wang, Z. & Britz, G. Regulation of cerebral blood flow. *Int. J. Vasc. Med.* **2011,** 823525 (2011).
83. Van Der Flier, W. M. *et al.* Small vessel disease and general cognitive function in nondisabled elderly: The LADIS study. *Stroke* **36,** 2116–2120 (2005).
84. Herrmann, L. L. *et al.* White matter hyperintensities in late life depression: a systematic review. *J. Neurol. Neurosurg. Psychiatry* **79,** 619–624 (2007).
85. de Laat, K. F. *et al.* Loss of white matter integrity is associated with gait disorders in cerebral small vessel disease. *Brain* **134,** 73–83 (2010).
86. Sudlow, C. L. M. & Warlow, C. P. Comparable studies of the incidence of stroke and its pathological types: Results from an international collaboration. *Stroke* **28,** 491–499 (1997).
87. Gorelick, P. B. *et al.* Vascular contributions to cognitive impairment and dementia: a statement for healthcare professionals from the american heart association/american stroke association. *Stroke* **42,** 2672–713 (2011).
88. Wardlaw, J. M., Smith, C. & Dichgans, M. Mechanisms of sporadic cerebral small vessel disease: Insights from neuroimaging. *The Lancet Neurology* **12,** 483–497 (2013).
89. Wardlaw, J. M., Dennis, M. S., Warlow, C. P. & Sandercock, P. A. Imaging appearance of the symptomatic perforating artery in patients with lacunar infarction: Occlusion or other vascular pathology? *Ann. Neurol.* **50,** 208–215 (2001).
90. Banerjee, G., Wilson, D., Jäger, H. R. & Werring, D. J. Novel imaging

techniques in cerebral small vessel diseases and vascular cognitive impairment. *Biochim. Biophys. Acta - Mol. Basis Dis.* **1862,** 926–938 (2016).

91. Blair, G. W., Hernandez, M. V., Thrippleton, M. J., Doubal, F. N. & Wardlaw, J. M. Advanced Neuroimaging of Cerebral Small Vessel Disease. *Curr. Treat. Options Cardiovasc. Med.* **19,** 56 (2017).
92. Starosolski, Z. *et al.* Ultra High-Resolution In vivo Computed Tomography Imaging of Mouse Cerebrovasculature Using a Long Circulating Blood Pool Contrast Agent. *Sci. Rep.* **5,** 10178 (2015).
93. Errico, C. *et al.* Ultrafast ultrasound localization microscopy for deep super-resolution vascular imaging. *Nature* **527,** 499–502 (2015).
94. Shih, A. Y. *et al.* Two-photon microscopy as a tool to study blood flow and neurovascular coupling in the rodent brain. *J. Cereb. blood flow Metab.* **32,** 1–33 (2012).
95. Strazzullo, P. *et al.* Excess body weight and incidence of stroke: Meta-analysis of prospective studies with 2 million participants. *Stroke* **41,** (2010).
96. Dearborn, J. L. *et al.* Obesity, Insulin Resistance, and Incident Small Vessel Disease on Magnetic Resonance Imaging. *Stroke* **46,** 3131–3136 (2015).
97. Mokdad, A. H. *et al.* Prevalence of Obesity, Diabetes, and Obesity-Related Health Risk Factors, 2001. *JAMA* **289,** (2003).
98. Hales, C. M., Carroll, M. D., Fryar, C. D. & Ogden, C. L. Prevalence of Obesity Among Adults and Youth: United States, 2015–2016. *NCHS Data Brief* 1–8 (2017). doi:10.1017/S1368980017000088
99. Kim, D. D. & Basu, A. Estimating the Medical Care Costs of Obesity in the United States: Systematic Review, Meta-Analysis, and Empirical Analysis. *Value in Health* **19,** 602–613 (2016).
100. Ovbiagele, B., Bath, P. M., Cotton, D., Vinisko, R. & Diener, H. C. Obesity and recurrent vascular risk after a recent ischemic stroke. *Stroke* **42,** 3397–

3402 (2011).

101. Poirier, P. *et al.* Obesity and Cardiovascular Disease: Pathophysiology, Evaluation, and Effect of Weight Loss: An Update of the 1997 American Heart Association Scientific Statement on Obesity and Heart Disease From the Obesity Committee of the Council on Nutrition, Physical. *Circulation* **113,** 898–918 (2006).
102. Kurth, T. *et al.* Body mass index and the risk of stroke in men. *Arch. Intern. Med.* **162,** 2557–2562 (2002).
103. Suk, S.-H. *et al.* Abdominal obesity and risk of ischemic stroke: the Northern Manhattan Stroke Study. *Stroke* **34,** 1586–1592 (2003).
104. Freedman, D. S., Khan, L. K., Dietz, W. H., Srinivasan, S. R. & Berenson, G. S. Relationship of Childhood Obesity to Coronary Heart Disease Risk Factors in Adulthood: The Bogalusa Heart Study. *Pediatrics* **108,** 712–718 (2001).
105. Benjamin, E. J. *et al.* Heart Disease and Stroke Statistics'2017 Update: A Report from the American Heart Association. *Circulation* **135,** e146–e603 (2017).
106. Blüher, M. Obesity: The myth of innocent obesity. *Nature Reviews Endocrinology* **13,** 691–692 (2017).
107. Ortega, F. B., Lavie, C. J. & Blair, S. N. Obesity and cardiovascular disease. *Circulation Research* **118,** 1752–1770 (2016).
108. Kim, S. H., Després, J.-P. & Koh, K. K. Obesity and cardiovascular disease: friend or foe? *Eur. Heart J.* ehv509 (2015). doi:10.1093/eurheartj/ehv509
109. Lavie, C. J., De Schutter, A. & Milani, R. V. Healthy obese versus unhealthy lean: The obesity paradox. *Nature Reviews Endocrinology* **11,** 55–62 (2015).
110. Lavie, C. J., McAuley, P. A., Church, T. S., Milani, R. V. & Blair, S. N. Obesity and cardiovascular diseases: Implications regarding fitness, fatness,

and severity in the obesity paradox. *Journal of the American College of Cardiology* **63,** 1345–1354 (2014).

111. Lavie, C. J., Milani, R. V. & Ventura, H. O. Obesity and Cardiovascular Disease. Risk Factor, Paradox, and Impact of Weight Loss. *Journal of the American College of Cardiology* **53,** 1925–1932 (2009).
112. Dehlendorff, C., Andersen, K. K. & Olsen, T. S. Body mass index and death by stroke no obesity paradox. *JAMA Neurol.* **71,** 978–984 (2014).
113. Akin, I. *et al.* No evidence of 'obesity Paradox' after treatment with drug-eluting stents in a routine clinical practice: Results from the prospective Multicenter German DES.DE (German Drug-Eluting Stent) registry. *JACC Cardiovasc. Interv.* **5,** 162–169 (2012).
114. Windberger, U., Bartholovitsch, A., Plasenzetti, R., Korak, K. J. & Heinze, G. Whole blood viscosity, plasma viscosity and erythrocyte aggregation in nine mammalian species: Reference values and comparison of data. *Experimental Physiology* **88,** 431–440 (2003).
115. Papaioannou, T. G. & Stefanadis, C. Vascular wall shear stress: basic principles and methods. *Hell. J. Cardiol.* **46,** 9–15 (2005).
116. Saunders, N. R., Liddelow, S. A. & Dziegielewska, K. M. Barrier mechanisms in the developing brain. *Front. Pharmacol.* **3 MAR,** 1–18 (2012).
117. Yezhuvath, U. S., Lewis-Amezcua, K., Varghese, R., Xiao, G. & Lu, H. On the assessment of cerebrovascular reactivity using hypercapnia BOLD MRI. *NMR Biomed.* **22,** 779–786 (2009).
118. Markus, H. & Cullinane, M. Severely impaired cerebrovascular reactivity predicts stroke and TIA risk in patients with carotid artery stenosis and occlusion. *Brain* **124,** 457–67 (2001).
119. Okazawa, H. *et al.* Effects of acetazolamide on cerebral blood flow, blood

volume, and oxygen metabolism: a positron emission tomography study with healthy volunteers. *J. Cereb. Blood Flow Metab.* **21,** 1472–9 (2001).

120. Buch, S., Ye, Y. & Haacke, E. M. Quantifying the changes in oxygen extraction fraction and cerebral activity caused by caffeine and acetazolamide. *J. Cereb. Blood Flow Metab.* **37,** 825–836 (2017).
121. Lim, G. B. Risk factors: CVD risk and the 'obesity paradox'. *Nat. Rev. Cardiol. 2015 1210* (2015).
122. Boillot, A. *et al.* Obesity and the Microvasculature: A Systematic Review and Meta-Analysis. *PLoS One* **8,** e52708 (2013).
123. Deng, J., Zhang, J., Feng, C., Xiong, L. & Zuo, Z. Critical role of matrix metalloprotease-9 in chronic high fat diet-induced cerebral vascular remodelling and increase of ischaemic brain injury in mice. *Cardiovasc. Res.* **103,** 473–484 (2014).
124. Selim, M., Jones, R., Novak, P., Zhao, P. & Novak, V. The effects of body mass index on cerebral blood flow velocity. *Clin. Auton. Res.* **18,** 331–338 (2008).
125. Uchino, K. *et al.* Increased cerebral oxygen metabolism and ischemic stress in subjects with metabolic syndrome-associated risk factors: preliminary observations. *Transl. Stroke Res.* **1,** 178–83 (2010).
126. Wiewiora, M., Piecuch, J., Glűck, M., Slowinska-Lozynska, L. & Sosada, K. Shear stress and flow dynamics of the femoral vein among obese patients who qualify for bariatric surgery. *Clin. Hemorheol. Microcirc.* **54,** 313–23 (2013).
127. Acharya, N. K. *et al.* Sevoflurane and Isoflurane induce structural changes in brain vascular endothelial cells and increase blood-brain barrier permeability: Possible link to postoperative delirium and cognitive decline. *Brain Res.* **1620,** 29–41 (2015).

128. Neuroscience, A., Hsu, T. M. & Kanoski, S. E. Blood-brain barrier disruption : mechanistic links between Western diet consumption and dementia. *Front. Aging Neurosci* **6,** 1–6 (2014).
129. Rouhl, R. P. W. *et al.* Vascular inflammation in cerebral small vessel disease. *Neurobiol. Aging* **33,** 1800–1806 (2012).
130. Sandoval, K. E. & Witt, K. A. Blood-brain barrier tight junction permeability and ischemic stroke. *Neurobiology of Disease* **32,** 200–219 (2008).
131. Chodobski, A., Zink, B. J. & Szmydynger-Chodobska, J. Blood-Brain Barrier Pathophysiology in Traumatic Brain Injury. *Translational Stroke Research* **2,** 492–516 (2011).
132. Hartz, A. M. S. *et al.* Amyloid- Contributes to Blood-Brain Barrier Leakage in Transgenic Human Amyloid Precursor Protein Mice and in Humans With Cerebral Amyloid Angiopathy. *Stroke* **43,** 514–523 (2012).
133. Saraiva, C. *et al.* Nanoparticle-mediated brain drug delivery : Overcoming blood – brain barrier to treat neurodegenerative diseases. *J. Control. Release* **235,** 34–47 (2016).
134. Wang, C. *et al.* Effects of sevoflurane versus propofol on cerebrovascular reactivity to carbon dioxide during laparoscopic surgery. *Ther. Clin. Risk Manag.* **13,** 1349–1355 (2017).
135. Schieve, J. F. & Wilson, W. P. The influence of age, anesthesia and cerebral arteriosclerosis on cerebral vascular activity to CO2. *Am. J. Med.* **15,** 171–174 (1953).
136. Blair, G. W., Doubal, F. N., Thrippleton, M. J., Marshall, I. & Wardlaw, J. M. Magnetic resonance imaging for assessment of cerebrovascular reactivity in cerebral small vessel disease: A systematic review. *J. Cereb. Blood Flow Metab.* **36,** 833–841 (2016).
137. Ellis, M. J. *et al.* Neuroimaging assessment of cerebrovascular reactivity in

concussion: Current concepts, methodological considerations, and review of the literature. *Front. Neurol.* **7,** (2016).

138. Stapleton, P. A., James, M. E., Goodwill, A. G. & Frisbee, J. C. Obesity and vascular dysfunction. *Pathophysiol. Off. J. Int. Soc. Pathophysiol.* **15,** 79–89 (2008).
139. Doupis, J. *et al.* Effects of Diabetes and Obesity on Vascular Reactivity, Inflammatory Cytokines, and Growth Factors. *Obesity* **19,** 729–735 (2011).
140. Teppema, L. J. *et al.* Effects of Acetazolamide on Ventilatory, Cerebrovascular, and Pulmonary Vascular Responses to Hypoxia. *Am. J. Respir. Crit. Care Med.* **175,** 277–281 (2007).
141. Tuettenberg, J., Heimann, A. & Kempski, O. Nitric oxide modulates cerebral blood flow stimulation by acetazolamide in the rat cortex: a laser Doppler scanning study. *Neurosci. Lett.* **315,** 65–68 (2001).
142. Fukumura, D. *et al.* Predominant role of endothelial nitric oxide synthase in vascular endothelial growth factor-induced angiogenesis and vascular permeability. *Proc Natl Acad Sci U S A* **98,** 2604–2609 (2001).
143. Krupinski, J., Kaluza, J., Kumar, P., Kumar, S. & Wang, J. Role of angiogenesis in patients with cerebral ischemic stroke. *Stroke* **25,** 1794–1798 (1994).
144. Endres, M., Laufs, U., Liao, J. K. & Moskowitz, M. A. Targeting eNOS for stroke protection. *Trends in Neurosciences* **27,** 283–289 (2004).
145. Cimino, M. *et al.* Neuroprotective effect of simvastatin in stroke: A comparison between adult and neonatal rat models of cerebral ischemia. in *NeuroToxicology* **26,** 929–933 (2005).
146. Jickling, G. C. *et al.* Hemorrhagic transformation after ischemic stroke in animals and humans. *J. Cereb. Blood Flow Metab.* **34,** 185–99 (2014).
147. Ergul, A. *et al.* Increased hemorrhagic transformation and altered infarct size

and localization after experimental stroke in a rat model type 2 diabetes. *BMC Neurol.* **7,** 33 (2007).

148. Li, W. *et al.* Adaptive cerebral neovascularization in a model of type 2 diabetes: relevance to focal cerebral ischemia. *Diabetes* **59,** 228–35 (2010).
149. Skolnick, B. E. *et al.* A Clinical Trial of Progesterone for Severe Traumatic Brain Injury. *N. Engl. J. Med.* **371,** 2467–2476 (2014).
150. Corps, K. N., Roth, T. L. & McGavern, D. B. Inflammation and neuroprotection in traumatic brain injury. *JAMA Neurol.* **72,** 355–362 (2015).
151. Kovacs, S. K., Leonessa, F. & Ling, G. S. F. Blast TBI Models, Neuropathology, and Implications for Seizure Risk. *Front. Neurol.* **5,** 47 (2014).
152. Chen, A. J.-W. & D'Esposito, M. Traumatic Brain Injury: From Bench to Bedside to Society. *Neuron* **66,** 470 (2010).
153. Jullienne, A. *et al.* Chronic cerebrovascular dysfunction after traumatic brain injury. *Journal of Neuroscience Research* **94,** 609–622 (2016).
154. Loane, D. J. & Faden, A. I. Neuroprotection for traumatic brain injury: Translational challenges and emerging therapeutic strategies. *Trends in Pharmacological Sciences* **31,** 596–604 (2010).
155. Jaeger, M., Schuhmann, M. U., Soehle, M. & Meixensberger, J. Continuous assessment of cerebrovascular autoregulation after traumatic brain injury using brain tissue oxygen pressure reactivity. *Crit. Care Med.* **34,** 1783–1788 (2006).
156. Diringer, M. N. *et al.* Regional cerebrovascular and metabolic effects of hyperventilation after severe traumatic brain injury. *J. Neurosurg.* **96,** 103–108 (2002).
157. Adelson, P. D. *et al.* Cerebrovascular response in infants and young children following severe traumatic brain injury: a preliminary report. *Pediatr.*

Neurosurg. **26,** 200–7 (1997).

158. Steiner, L. A., Czosnyka, M. & Piechnik, S. K. Continuous monitoring of cerebrovascular pressure reactivity allows determination of optimal cerebral perfusion pressure in patients with traumatic brain injury. *Crit. Care* **30,** 733–738 (2002).
159. Kenney, K. *et al.* Cerebral Vascular Injury in Traumatic Brain Injury. *Exp. Neurol.* **275,** 353–366 (2016).
160. Bitner, B. R. *et al.* Antioxidant carbon particles improve cerebrovascular dysfunction following traumatic brain injury. *ACS Nano* **6,** 8007–8014 (2012).
161. DeWitt, D. S. & Prough, D. S. Traumatic Cerebral Vascular Injury: The Effects of Concussive Brain Injury on the Cerebral Vasculature. *J. Neurotrauma* **20,** 795–825 (2003).
162. Werner, C. & Engelhard, K. Pathophysiology of traumatic brain injury. *Br. J. Anaesth.* **99,** 4–9 (2007).
163. Rostami, E., Engquist, H. & Enblad, P. Imaging of cerebral blood flow in patients with severe traumatic brain injury in the neurointensive care. *Frontiers in Neurology* **5 JUL,** (2014).
164. Udomphorn, Y., Armstead, W. M. & Vavilala, M. S. Cerebral Blood Flow and Autoregulation After Pediatric Traumatic Brain Injury. *Pediatric Neurology* **38,** 225–234 (2008).
165. Botteri, M., Bandera, E., Minelli, C. & Latronico, N. Cerebral blood flow thresholds for cerebral ischemia in traumatic brain injury. A systematic review. *Crit. Care Med.* **36,** 3089–3092 (2008).
166. Wintermark, M. *et al.* Cerebral vascular autoregulation assessed by perfusion-CT in severe head trauma patients. *J. Neuroradiol.* **33,** 27–37 (2006).

167. Schneider, H. J., Kreitschmann-Andermahr, I., Ghigo, E., Stalla, G. K. & Agha, A. Hypothalamopituitary dysfunction following traumatic brain injury and aneurysmal subarachnoid hemorrhage: a systematic review. *JAMA* **298,** 1429–1438 (2007).
168. Kurland, D., Hong, C., Aarabi, B., Gerzanich, V. & Simard, J. M. Hemorrhagic Progression of a Contusion after Traumatic Brain Injury: A Review. *J. Neurotrauma* **29,** 19–31 (2012).
169. Perrein, A. *et al.* Cerebral vasospasm after traumatic brain injury: An update. *Minerva Anestesiologica* **81,** 1219–1228 (2015).
170. Armin, S. S., Colohan, A. R. T. & Zhang, J. H. Vasospasm in traumatic brain injury. *Acta Neurochir. Suppl.* **104,** 421–425 (2008).
171. Reznik, M., Saeed, Y. & Shutter, L. Teaching Neuro Images: Severe vasospasm in traumatic brain injury. *Neurology* **86,** e132–e133 (2016).
172. Kramer, D. R., Winer, J. L., Pease, B. A. M., Amar, A. P. & Mack, W. J. Cerebral Vasospasm in Traumatic Brain Injury. *Neurol. Res. Int.* **2013,** 1–7 (2013).
173. Alluri, H., Wiggins-Dohlvik, K., Davis, M. L., Huang, J. H. & Tharakan, B. Blood–brain barrier dysfunction following traumatic brain injury. *Metabolic Brain Disease* **30,** 1093–1104 (2015).
174. Hay, J. R., Johnson, V. E., Young, A. M. H., Smith, D. H. & Stewart, W. Blood-Brain Barrier Disruption Is an Early Event That May Persist for Many Years After Traumatic Brain Injury in Humans. *J. Neuropathol. Exp. Neurol.* **74,** 1147–57 (2015).
175. Alves, J. L. Blood-brain barrier and traumatic brain injury. *Journal of Neuroscience Research* **92,** 141–147 (2014).
176. Saw, M. M. *et al.* Differential Disruption of Blood–Brain Barrier in Severe Traumatic Brain Injury. *Neurocrit. Care* **20,** 209–216 (2014).

177. Wei, E. P., Hamm, R. J., Baranova, A. I. & Povlishock, J. T. The Long-Term Microvascular and Behavioral Consequences of Experimental Traumatic Brain Injury after Hypothermic Intervention. *J. Neurotrauma* **26,** 527–537 (2009).
178. Xiong, Y., Mahmood, A. & Chopp, M. Animal models of traumatic brain injury. *Nat. Rev. Neurosci.* **14,** 128–142 (2013).
179. O'Connor, W. T., Smyth, A. & Gilchrist, M. D. Animal models of traumatic brain injury: A critical evaluation. *Pharmacology and Therapeutics* **130,** 106–113 (2011).
180. Rosenfeld, J. V. *et al.* Blast-related traumatic brain injury. *The Lancet Neurology* **12,** 882–893 (2013).
181. Wang, Y. *et al.* Tightly Coupled Repetitive Blast-Induced Traumatic Brain Injury: Development and Characterization in Mice. *J. Neurotrauma* **28,** 2171–2183 (2011).
182. Cheng, J. *et al.* Development of a rat model for studying blast-induced traumatic brain injury. *J. Neurol. Sci.* **294,** 23–28 (2010).
183. Risling, M. & Davidsson, J. Experimental animal models for studies on the mechanisms of blast-induced neurotrauma. *Front. Neurol.* **APR,** (2012).
184. Long, J. B. *et al.* Blast Overpressure in Rats: Recreating a Battlefield Injury in the Laboratory. *J. Neurotrauma* **26,** 827–840 (2009).
185. Cao, R. *et al.* Functional and oxygen-metabolic photoacoustic microscopy of the awake mouse brain. *Neuroimage* **150,** 77–87 (2017).
186. Soetikno, B. *et al.* Vessel segmentation analysis of ischemic stroke images acquired with photoacoustic microscopy. *SPIE BiOS* **8223,** 822345 (2012).
187. Holtmaat, A. *et al.* Long-term, high-resolution imaging in the mouse neocortex through a chronic cranial window. *Nat. Protoc.* **4,** 1128–1144 (2009).

188. Goldey, G. J. *et al.* Removable cranial windows for long-term imaging in awake mice. *Nat. Protoc.* **9,** 2515–2538 (2014).
189. Mishra, V. *et al.* Primary blast causes mild, moderate, severe and lethal TBI with increasing blast overpressures: Experimental rat injury model. *Sci. Rep.* **6,** (2016).
190. Hester, R. L., Eraslan, A. & Saito, Y. Differences in EDNO contribution to arteriolar diameters at rest and during functional dilation in striated muscle. *Am. J. Physiol. Heart Circ. Physiol.* **265,** H146–H151 (1993).
191. Vorstrup, S., Henriksen, L. & Paulson, O. B. Effect of acetazolamide on cerebral blood flow and cerebral metabolic rate for oxygen. *J. Clin. Invest.* **74,** 1634–9 (1984).
192. Oertel, M. *et al.* Posttraumatic vasospasm: the epidemiology, severity, and time course of an underestimated phenomenon: a prospective study performed in 299 patients. *J. Neurosurg.* **103,** 812–824 (2005).
193. Vespa, P. *et al.* Metabolic Crisis without Brain Ischemia is Common after Traumatic Brain Injury: A Combined Microdialysis and Positron Emission Tomography Study. *J. Cereb. Blood Flow Metab.* **25,** 763–774 (2005).
194. Logsdon, A. F. *et al.* Role of microvascular disruption in brain damage from traumatic brain injury. *Compr. Physiol.* **5,** 1147–1160 (2015).
195. Bailey, D. M. *et al.* Impaired cerebral haemodynamic function associated with chronic traumatic brain injury in professional boxers. *Clin. Sci.* **124,** 177–189 (2013).
196. Obenaus, A. *et al.* Traumatic brain injury results in acute rarefication of the vascular network. *Sci. Rep.* **7,** (2017).
197. Chan, S. tak *et al.* Transcranial Doppler study of cerebrovascular reactivity: Are migraineurs more sensitive to breath-hold challenge? *Brain Res.* **1291,** 53–59 (2009).

198. Tully, H. Go with the flow: Cerebrovascular reactivity as a therapeutic target for TBI symptoms. *Sci. Transl. Med.* **10,** eaat1643 (2018).
199. Donkin, J. J. & Vink, R. Mechanisms of cerebral edema in traumatic brain injury: Therapeutic developments. *Current Opinion in Neurology* **23,** 293–299 (2010).
200. Winkler, E. A., Minter, D., Yue, J. K. & Manley, G. T. Cerebral Edema in Traumatic Brain Injury: Pathophysiology and Prospective Therapeutic Targets. *Neurosurgery Clinics of North America* **27,** 473–488 (2016).
201. Saunders, N. R., Dziegielewska, K. M., Møllgård, K. & Habgood, M. D. Markers for blood-brain barrier integrity: how appropriate is Evans blue in the twenty-first century and what are the alternatives? *Front. Neurosci.* **9,** 385 (2015).
202. Xu, Z., Zhu, Q. & Wang, L. V. In vivo photoacoustic tomography of mouse cerebral edema induced by cold injury. *J. Biomed. Opt.* **16,** 66020 (2011).
203. Ventura, S. J., Martin, J. a, Curtin, S. C., Mathews, T. J. & Park, M. M. *Births: Final data for 1998. National Vital Statistics Reports* **48,** (2000).
204. Members, W. G. *et al.* Heart Disease and Stroke Statistics—2010 Update. *Circulation* **121,** e46–e215 (2010).
205. Sacco, R. L., Wolf, P. A. & Gorelick, P. B. Risk factors and their management for stroke prevention: outlook for 1999 and beyond. *Neurology* **53,** S15-24 (1999).
206. Adams, H. P. *et al.* Classification of subtype of acute ischemic stroke. Definitions for use in a multicenter clinical trial. TOAST. Trial of Org 10172 in Acute Stroke Treatment. *Stroke* **24,** 35–41 (1993).
207. J.L., S. *et al.* The golden hour and acute brain ischemia: Presenting features and lytic therapy in over 30,000 patients arriving within 60 minutes of onset at GWTG-S hospitals. *Stroke* **40,** e113 (2009).

208. Lipton, P. Ischemic cell death in brain neurons. *Physiol. Rev.* **79,** 1431–1568 (1999).
209. Donnan, G. A. & Davis, S. M. Neuroimaging, the ischaemic penumbra, and selection of patients for acute stroke therapy. *Lancet Neurology* **1,** 417–425 (2002).
210. Heiss, W. D., Kracht, L. W., Thiel, A., Grond, M. & Pawlik, G. Penumbral probability thresholds of cortical flumazenil binding and blood flow predicting tissue outcome in patients with cerebral ischaemia. *Brain* **124,** 20–29 (2001).
211. Sobesky, J. *et al.* Does the Mismatch Match the Penumbra? *Stroke* **36,** 980–985 (2005).
212. Jordan, J. D. & Powers, W. J. Cerebral autoregulation and acute ischemic stroke. *Am. J. Hypertens.* **25,** 946–950 (2012).
213. Bandera, E. *et al.* Cerebral blood flow threshold of ischemic penumbra and infarct core in acute ischemic stroke: A systematic review. *Stroke* **37,** 1334–1339 (2006).
214. Giubilei, F. *et al.* Predictive value of brain perfusion single-photon emission computed tomography in acute ischemic stroke. *Stroke* **21,** 895–900 (1990).
215. Nour, M., Scalzo, F. & Liebeskind, D. S. Ischemia-Reperfusion Injury in Stroke. *Interv. Neurol.* **1,** 185–199 (2012).
216. Denner, L. Stroke and ischemia-reperfusion injury. *IDrugs Investig. drugs J.* **4,** 20–22 (2001).
217. Cipolla, M. J., McCall, A. L., Lessov, N. & Porter, J. M. Reperfusion decreases myogenic reactivity and alters middle cerebral artery function after focal cerebral ischemia in rats. *Stroke* **28,** 176–180 (1997).
218. An, H. *et al.* Imaging Oxygen Metabolism In Acute Stroke Using MRI. *Curr. Radiol. Rep.* **2,** 39 (2014).

219. Lenzi, G. L., Frackowiak, R. S. & Jones, T. Cerebral oxygen metabolism and blood flow in human cerebral ischemic infarction. *J Cereb Blood Flow Metab* **2,** 321–335 (1982).
220. Durukan, A. & Tatlisumak, T. Acute ischemic stroke: Overview of major experimental rodent models, pathophysiology, and therapy of focal cerebral ischemia. *Pharmacol. Biochem. Behav.* **87,** 179–197 (2007).
221. Bogousslavsky, J., Melle, G. Van & Regli, F. The lausanne stroke registry: Analysis of 1,000 consecutive patients with first stroke. *Stroke* **19,** 1083–1092 (1988).
222. Fluri, F., Schuhmann, M. K. & Kleinschnitz, C. Animal models of ischemic stroke and their application in clinical research. *Drug Des. Devel. Ther.* **9,** 3445–3454 (2015).
223. Sutherland, B. A. *et al.* The transient intraluminal filament middle cerebral artery occlusion model as a model of endovascular thrombectomy in stroke. *J. Cereb. Blood Flow Metab.* **36,** 363–369 (2016).
224. Liu, S., Zhen, G., Meloni, B. P., Campbell, K. & Winn, H. R. Rodent stroke model guidelines for preclinical stroke trials (1st edition). *J. Exp. Stroke Transl. Med.* **2,** 2–27 (2009).
225. Li, L. & Zuo, Z. Isoflurane preconditioning improves short-term and long-term neurological outcome after focal brain ischemia in adult rats. *Neuroscience* **164,** 497–506 (2009).
226. Evans, M. R. B., White, P., Cowley, P. & Werring, D. J. Revolution in acute ischaemic stroke care: a practical guide to mechanical thrombectomy. *Pract. Neurol.* **17,** 252–265 (2017).
227. Singhal, A. B., Lo, E. H., Dalkara, T. & Moskowitz, M. A. in *Acute Ischemic Stroke* 1–26 (2006). doi:10.1007/3-540-30810-5_1
228. Savitz, S. I. & Fisher, M. Future of neuroprotection for acute stroke: In the

aftermath of the SAINT trials. *Annals of Neurology* **61,** 396–402 (2007).

229. Berlis, A. *et al.* Mechanical thrombolysis in acute ischemic stroke with endovascular photoacoustic recanalization. *Stroke* **35,** 1112–1116 (2004).
230. Zhang, L., Zhang, Z. G. & Chopp, M. The neurovascular unit and combination treatment strategies for stroke. *Trends in Pharmacological Sciences* **33,** 415–422 (2012).
231. Kim, G. S. *et al.* Critical role of sphingosine-1-phosphate receptor-2 in the disruption of cerebrovascular integrity in experimental stroke. *Nat. Commun.* **6,** 7893 (2015).
232. Blaho, V. A. & Hla, T. An update on the biology of sphingosine 1-phosphate receptors. *J. Lipid Res.* **55,** 1596–1608 (2014).
233. Sun, K. *et al.* Sphingosine-1-phosphate promotes erythrocyte glycolysis and oxygen release for adaptation to high-altitude hypoxia. *Nat. Commun.* **7,** 12086 (2016).
234. Spiegel, S. & Milstien, S. Sphingosine-1-phosphate: An enigmatic signalling lipid. *Nature Reviews Molecular Cell Biology* **4,** 397–407 (2003).
235. Kharel, Y. *et al.* Sphingosine Kinase 2 Inhibition and Blood Sphingosine 1-Phosphate Levels. *J. Pharmacol. Exp. Ther.* **355,** 23–31 (2015).
236. Shaner, R. L. *et al.* Quantitative analysis of sphingolipids for lipidomics using triple quadrupole and quadrupole linear ion trap mass spectrometers. *J. Lipid Res.* **50,** 1692–1707 (2009).
237. Kharel, Y. *et al.* Sphingosine kinase type 1 inhibition reveals rapid turnover of circulating sphingosine 1-phosphate. *Biochem. J.* **440,** 345–353 (2011).
238. Urtz, N. *et al.* Sphingosine 1-phosphate produced by sphingosine kinase 2 intrinsically controls platelet aggregation in vitro and in vivo. *Circ. Res.* **117,** 376–387 (2015).
239. Brait, V. H., Tarrasón, G., Gavaldà, A., Godessart, N. & Planas, A. M.

Selective Sphingosine 1-Phosphate Receptor 1 Agonist Is Protective Against Ischemia/Reperfusion in Mice. *Stroke* **47,** 3053–3056 (2016).

240. Kimura, A. *et al.* Antagonism of sphingosine 1-phosphate receptor-2 enhances migration of neural progenitor cells toward an area of brain infarction. *Stroke* **39,** 3411–3417 (2008).
241. Iwasawa, E. *et al.* Sphingosine-1-Phosphate Receptor 1 Activation Enhances Leptomeningeal Collateral Development and Improves Outcome after Stroke in Mice. *J. Stroke Cerebrovasc. Dis.* (2018). doi:10.1016/j.jstrokecerebrovasdis.2017.11.040
242. Hasegawa, Y., Suzuki, H., Sozen, T., Rolland, W. & Zhang, J. H. Activation of sphingosine 1-phosphate receptor-1 by FTY720 is neuroprotective after ischemic stroke in rats. *Stroke* **41,** 368–374 (2010).
243. Ader, I., Malavaud, B. & Cuvillier, O. When the sphingosine kinase 1/sphingosine 1-phosphate pathway meets hypoxia signaling: New targets for cancer therapy. *Cancer Research* **69,** 3723–3726 (2009).
244. Bouquerel, P. *et al.* Essential role for SphK1/S1P signaling to regulate hypoxia-inducible factor 2α expression and activity in cancer. *Oncogenesis* **5,** e209 (2016).
245. Rapizzi, E. *et al.* Sphingosine 1-phosphate increases glucose uptake through trans-activation of insulin receptor. *Cell. Mol. Life Sci.* **66,** 3207–18 (2009).